Abstract

MERTYUREK, UGUR. **Super-Nodal Methods for Space-Time Kinetics**. (Under the direction of Paul J. Turinsky)

The purpose of this research has been to develop an advanced Super-Nodal method to reduce the run time of 3-D core neutronics models, such as in the NESTLE reactor core simulator and FORMOSA nuclear fuel management optimization codes. Computational performance of the neutronics model is increased by reducing the number of spatial nodes used in the core modeling. However, as the number of spatial nodes decreases, the error in the solution increases. The Super-Nodal method reduces the error associated with the use of coarse nodes in the analyses by providing a new set of cross sections and ADFs (Assembly Discontinuity Factors) for the new nodalization. These so called homogenization parameters are obtained by employing consistent collapsing technique.

During this research a new type of singularity, namely “fundamental mode singularity”, is addressed in the ANM (Analytical Nodal Method) solution. The “Coordinate Shifting” approach is developed as a method to address this singularity. Also, the “Buckling Shifting” approach is developed as an alternative and more accurate method to address the zero buckling singularity, which is a more common and well known singularity problem in the ANM solution. In the course of addressing the treatment of these singularities, an effort was made to provide better and more robust

results from the Super-Nodal method by developing several new methods for determining the transverse leakage and collapsed diffusion coefficient, which generally are the two main approximations in the ANM methodology. Unfortunately, the proposed new transverse leakage and diffusion coefficient approximations failed to provide a consistent improvement to the current methodology. However, improvement in the Super-Nodal solution is achieved by updating the homogenization parameters at several time points during a transient. The update is achieved by employing a refinement technique similar to pin-power reconstruction. A simple error analysis based on the relative residual in the 3-D few group diffusion equation at the fine mesh level is also introduced in this work.

The proposed Super-Nodal method was tested for PWR cores with large heterogeneities and under severe reactor accident conditions. Two nodalizations, SN1 and SN2, have been used with three types of collapsing schemes, namely SN1, SN2, and SN1-r. The core is axially collapsed from 18 nodes to 12 and 8 nodes in the SN1 and SN2 nodalizations, respectively. While the SN1 and SN2 schemes refer to SN1 and SN2 nodalizations, SN1-r refers to SN1 nodalization with multiple refining steps. The first test case is the steady state analysis of a core. The general core geometry is modified to introduce a strong heterogeneity by introducing partial length BP rods in the four central fuel assemblies. Even though the Super-Nodal method agrees well with the fine *i.e.* reference, solution for the axial and radial power distributions, it fails to represent the intra-nodal flux shape for the BP loaded assemblies. For the second test case the core is depleted and a control rod bank is inserted and withdrawn in 40 seconds. A computer CPU time speedup of 1.53 and 1.64 are achieved for the SN1 and SN2 schemes, respectively. Both schemes represent the core power level with a small error; however, both schemes fail to accurately represent the peak node power during the transient. The SN1-r scheme with two additional refining steps removes this discrepancy with a decreased speedup of 1.24.

Test Case 3 is a rod ejection accident. Similar to Test Case 2, all three schemes predict accurately the core power level; however, only the SN1-r scheme shows good accuracies for the peak node power. The SN1, SN2 and SN1-r schemes give speedups of 1.53, 2.08 and 1.26, respectively.

Test Case 4 is a large steam line break accident. The SN2 and SN1 schemes fail to converge beyond the point that the prompt criticality is reached. The SN1-r scheme agrees well with the reference solution's axial and radial power distributions. It also provides an accurate prediction of peak node power except at the time of prompt criticality where the peak node power error reaches 10% of full rated power. The speedup is also small for this case, 1.15, due to the need for frequent refine-collapse steps in order to achieve adequate accuracy.

Super-Nodal Methods for Space-Time Kinetics

by

Ugur Mertyurek

A dissertation submitted to the Graduate Faculty of
North Carolina State University
in partial fulfillment of the
requirements for the Degree of
Doctor of Philosophy

Nuclear Engineering

Raleigh, North Carolina

2002

APPROVED BY:

Paul J. Turinsky, Chair of Advisory Committee

Kuruvilla Verghese

Robert E. Funderlic

Dmitriy Y. Anistratov

Robert E. White

For my wife

Biography

Ugur Mertyurek was born in Gaziantep, Turkey on April 20, 1970 and graduated from Gaziantep High School in June 1987. He received his B.S. degree in Nuclear Engineering in 1992 from Hacettepe University in Ankara, Turkey. Immediately after graduation, he worked as a teaching assistant in the Nuclear Engineering Department at Hacettepe University for one year. Later, he transferred to the University of Tennessee at Knoxville, where he received his Master of Science degree in Nuclear Engineering in December 1995. During his master studies he held a research assistantship funded by the Tennessee Valley Authority with the Nuclear Engineering Department.

In January 1996 he moved to Raleigh, North Carolina for his PhD degree in Nuclear Engineering at North Carolina State University. During his PhD studies, he simultaneously earned a Master of Computer Science in August 2001, and earned his PhD in Nuclear Engineering in May 2002.

Acknowledgement

I would like thank three men that I have seen as role models in preparing me for today and my academic accomplishments.

My father, Metin Mertyurek, who has taught me to never give up. He also has taught me to smile and take pleasure from life even during the hardest times. Although he tried really hard to earn his PhD degree, he could not due to political reasons in our country. Therefore, I earned one for the both of us.

Dr. Osman K. Kadiroglu, who motivated me to finish my undergraduate degree and to come to the United States. He treated his students like their friends and made us feel unique and enjoy being nuclear engineers.

My advisor, Dr. Paul Turinsky, who showed me the path to be an excellent engineer and excellent scientist. I am honored to be one of his students. Unfortunately, as a role model, he sets the flag so high, it would be a while until I get there. I would like to thank him for his patience and support he provided me whenever I knocked at his door almost everyday with a new problem for the past six years.

I would also like to thank my friends for supporting me and helping me with their wisdom, Dr. Atul Karve, Prakash Narayanan, Yannis Mavropoulos, Erdal Aycicek and Dr. Isa Sarac.

I am grateful to both my parents, Metin and Necla Mertyurek, and my wife's parents, Hasan Kemalettin and Sare Mutlu, for helping me with their prayers.

I dedicate this thesis to my wife, Suzan. For being there for me, for her endless patience, support, encouragement and putting up with me during all these stressful years. I am not sure if I could have finished this thesis without her help.

"The purpose of learning is to make knowledge a guide in life and illuminate the road to human betterment. For this reason, any knowledge not appropriated for the self is a burden on the back of the learner, and the science which does not direct man toward sublime goals is a deception."

Table of Contents

List of Figures

List of Tables

1. Introduction

1.1 Overview and Motivation

The utilization of three-dimensional core simulators in transient analysis began to appear in applications such as accident analysis and predictive expert system aids over the past few years. In addition, three-dimensional core simulators have recently begun to be utilized in steady-state analysis in support of nuclear fuel management optimization (NFMO).

For most applications such as nuclear safety analysis, a complete system model representing core physics and thermal-hydraulics is required. The general strategy is to integrate a three-dimensional core neutronics simulator with a thermal-hydraulics transient code like RELAP5, TRAC, or RETRAN. The most relevant example, in regard to this proposal, is the integration of the RELAP5 thermal-hydraulics code with the NESTLE [1] reactor core code, which solves the few group neutron diffusion equation via the analytical nodal method (ANM). Despite recent developments in computer hardware and numerical analysis, this is a challenging problem, because such a 3-D core neutronics model creates a large overhead on a thermal-hydraulics system model that already requires large computational resources. Computational overhead of a 3-D core model is even more noticeable when a complex thermal hydraulics model along with a 3-D core model is used in a NFMO code such as FORMOSA-B [2]. The need for an increase in computational efficiency is clear, especially when a simulator faster than real-time is needed for applications like training and predictive expert systems.

This thesis addresses the issue of computational burden from a neutronics viewpoint. One way of increasing computational performance in the neutronics model is to decrease the number of spatial nodes. This approach is referred to as Super-Nodal methods in neutronics. It is possible to collapse from a finer mesh to a coarser mesh in a consistent manner by preserving neutron interaction rates and surface currents on a spatial node-wise basis. By doing this, improved computation time is obtained at the expense of decreased accuracy, the loss of accuracy increasing as the current core state deviates more from the reference core state used to complete consistent collapse.

If error bounds could be obtained as a function of time, this information could then be used to offer the choice of using a finer or a coarser spatial mesh size at each time step, so as to preserve a specified fidelity.

1.2 Literature Review

1.2.1 Nodal Methods

Employing the finite difference method for accurate solutions of core neutronic problems like transients and burnup calculations is impractical because of its high cost. The computer time can be reduced by using coarser spatial mesh sizes, however the finite difference method becomes inaccurate.

Nodal methods have been popular since the early seventies, due to their effectiveness in increasing the speed of the computations, and their accuracy compared to costly fine mesh finite difference solutions [3]-[20]. The nodal methods subdivide the reactor core into large regions called *nodes* and represent the flux distribution inside nodes using a more sophisticated formulation than finite difference methods. The main idea in nodal methods is similar to the finite difference methods. The few-group diffusion equation is volume integrated over a node and the surface currents are related to the node average fluxes by means of coupling coefficients. While the coupling coefficients are defined in terms of diffusion coefficients and mesh spacing in the finite difference methods, the nodal methods use different, more complicated approaches [21]. Because of computational speed limitations in early years, the motivation was to develop computationally more efficient nodal methods at the cost of accuracy. FLARE [21]. and its successors used parameter adjustment techniques to improve prediction agreement with plant data. Over the last 15 years a second class of nodal methods, modern nodal methods, have been developed to replace empirical parameters approach [11].

Probably the most common modern nodal methods are transverse integrated nodal methods. In this class of nodal methods the three-dimensional few-group neutron diffusion equation is replaced by three one dimensional diffusion equations. These one-dimensional equations are obtained by integrating the 3-D neutron diffusion equation over the two directions transverse to the direction of interest. The resultant leakages out of the transverse faces are unknown and must be approximated.

The transverse integrated nodal methods are divided into two general classes: polynomial and analytical methods.

1.2.1.1 Nodal Expansion Methods

Among the various polynomial methods, the Nodal Expansion Methods (NEM) developed by Finnemann and Bennewitz [3]-[5] plays an important role in nodal diffusion calculations. NEM, one of the earliest polynomial methods, originated from the Nodal Synthesis Method. In these methods, the transverse integrated fluxes are approximated by polynomials of up to fourth order. Higher order expansions are also possible [5]. Three of the five coefficients of these polynomials are calculated by demanding neutron balance for each node, and continuity of the surface average fluxes and currents between two adjacent nodes. The remaining two coefficients are determined by demanding preservation of higher moments of the flux using a weighted residual procedure on the transverse integrated diffusion equation. The calculation of the associated transverse leakage moments requires approximation of the transverse leakage shape. In the initial NEM by Finnemann [3], it was assumed that the transverse leakage and the one-dimensional flux have the same shape ("Buckling approximation"). The Buckling approximation leads to large errors in realistic heterogeneous core configurations. An improved procedure by Finnemann [5] was introduced in which the transverse leakage is approximated by a quadratic polynomial. The expansion coefficients are calculated by assuming that the quadratic polynomial extends over the two neighboring nodes and satisfies the average leakages in the central and two neighboring nodes. The quadratic leakage fit does not rely on the diffusion equation itself and can only be justified if the transverse leakages vary smoothly across the three nodes. This is usually not the case near strong absorbers or at boundaries.

1.2.1.2 Analytical Nodal Methods

The other class of nodal methods, Analytical Nodal Methods (ANM), was developed at MIT by Henry and his co-workers [7]-[10]. ANM solves the transverse integrated diffusion equation analytically, most times applied to two energy groups. ANM determines the flux distribution by imposing continuity of surface average currents and surface average fluxes between adjacent nodes as boundary conditions. As in NEM, ANM also relies on the assumed shape of the transverse leakages. Finneman and his colleagues [3] used a Buckling approximation to eliminate the leakage term and reduced the transverse integrated diffusion equation into a seven-point difference equation for the fluxes alone. Although this approach simplifies the calculations, as in NEM, it leads to large errors [9]. In order to improve accuracy, Finneman and his colleagues [5] implemented a quadratic leakage representation. Since the quadratic leakage approach couples neighboring node leakages, a solution scheme similar to NEM is used instead of Finneman's seven-point difference approach. Greenman and Smith [12] performed a numerical study of the errors associated with the quadratic transverse leakage approximation. The transverse leakage approximation is a weak point of nodal methods. There have been numerous researches to improve this approximation. Abderrafi and

Ougouag [13] improved the transverse leakage approximation by moment weighting the diffusion equation by the Legendre Polynomials before transverse integrating the diffusion equation. This approach allowed them to expand transverse leakages in a series of Legendre Polynomials. Chao [14] used a sine function to represent transverse leakages. One of the most notable approaches is Finnemann and Wagner's [4] quadratic expansion in which they included the cross product terms and represented the flux in a non-separable polynomial form in 2-D. They calculate leakages from the reconstructed flux, this flux selected so as to preserve the average flux in the central and four neighboring nodes, and imposing continuity of surface average flux and current. Chao [14] improved Finnemann and Wagner's method by representing the flux using a quartic non-separable expansion in 2-D. Later, Noh and Cho [16] developed an analytical solution using 2-D non-separable functions following the same idea but only completing transverse integration in one direction. Unfortunately, although these methods introduced more accuracy, they also added additional complexity and computational burden.

In order to use ANM for the solution of multigroup diffusion equations, decoupling of the multigroup equations is necessary. The complexity of this procedure makes ANM more computationally expensive than NEM. There are also stability issues associated with ANM in some cases. These instabilities originate from the nature of the trigonometric functions in the solution of the flux. One of these instabilities occurs when the k_∞ value of the node approaches close to the k_{eff} value. Two possible treatments for this instability are outlined by Joo [17] and Smith [10]. Most nodal method neutronics codes employ NEM because of its computational efficiency and stability compared to ANM. On the other hand, ANM produces more accurate results than NEM, particularly when the nodal meshing is large [6], [7].

1.2.1.3 Spatial Homogenization Methods

The diffusion equation assumes that the pin-by-pin lattice cross sections have been spatially homogenized to obtain 'equivalent' diffusion theory parameters which are spatially constant (or smoothly varying) over the entire cross sectional area of a fuel assembly. These node-averaged cross sections are important for the nodal analysis of reactor core problems. Since all properties of the original intra-nodal heterogeneous solution cannot be represented with homogenized parameters, the most commonly employed procedure for determining homogenized parameters focuses on preservation of averaged group reaction rates and the surface averaged group currents, which assures preservation of the reactor eigenvalue [18], [19]. Ideal homogenized parameters can be defined as

$$\hat{\Sigma}^{l}_{\alpha g} = \frac{\int_{Vi} \Sigma_{\alpha g}(\boldsymbol{r})\boldsymbol{\phi}_{g}(\boldsymbol{r})\boldsymbol{dr}}{\int_{Vi} \boldsymbol{\phi}_{g}(\boldsymbol{r})\boldsymbol{dr}} \tag{1-1}$$

where $\Sigma_{\alpha g}(r)$, $\phi_g(r)$, $\hat{\Sigma}^{l}_{\alpha g}$ and $\hat{\phi}_g(r)$ represent heterogeneous and homogenous, respectively, cross sections and fluxes, respectively, for group *g*, and

$$\hat{D}^{l,k}_{g} = \frac{-\int_{S_i^k} \vec{J}_g(r)\cdot\hat{n}_s dS}{\int_{S_i^k} \vec{\nabla}\phi_g(r)\cdot\hat{n}_s dS} \tag{1-2}$$

where $\hat{\boldsymbol{D}}^{\boldsymbol{l,k}}_{\boldsymbol{g}}$ is the homogenized diffusion coefficient on surface *k* of node *l* .

The heterogeneous flux $\phi_g(r)$ is typically approximated by solving a 2-D lattice physics problem imposing $\vec{\boldsymbol{J}}\cdot\hat{\boldsymbol{n}}_{\boldsymbol{s}} = 0$ (zero net current) boundary conditions for an assembly or color-set. Obviously, this method preserves the node-averaged reaction rates and surface currents only if the reactor consists of an infinite set of the same color-set. For a realistic core model with multiple color-sets, the homogenous cross sections are only approximate.

Equation (1-2) shows that the diffusion coefficient is surface dependent, hence direction dependent. Therefore, it is impossible to define spatially constant values of the diffusion coefficient such that reaction rates and leakages are satisfied at the same time.

Different methods have been developed to obtain the homogenized diffusion coefficient [23]. One method treats the diffusion coefficient similar to the cross-sections and uses flux-volume weighting.

$$\hat{\boldsymbol{D}}_g^{\boldsymbol{I}} = \frac{\int_{Vi} \boldsymbol{D}_g(\boldsymbol{r})\boldsymbol{\phi}_g(\boldsymbol{r})\boldsymbol{dr}}{\int_{Vi} \boldsymbol{\phi}_g(\boldsymbol{r})\boldsymbol{dr}} \tag{1-3}$$

Another simplistic approach defines the diffusion coefficient as,

$$\hat{\boldsymbol{D}}_g^{\boldsymbol{I}} = 1/3\hat{\Sigma}_{trg}^{\boldsymbol{I}}$$

where

$$\hat{\Sigma}_{trg}^{\boldsymbol{I}} = \frac{\int_{Vi} \Sigma_{trg}^{\boldsymbol{I}}(\boldsymbol{r})\boldsymbol{\phi}_g(\boldsymbol{r})\boldsymbol{dr}}{\int_{Vi} \boldsymbol{\phi}_g(\boldsymbol{r})\boldsymbol{dr}} \tag{1-4}$$

Koebke [18] and Smith [19] showed that the persistence of large errors in the solution of the homogenized diffusion equation, even using exact flux weighted cross sections, indicates that the inaccurate approximation of the leakage term is the major contributor to the error.

To sort out how both reaction rates and surface leakages can both be preserved, Koebke made the following observation: Since the homogenous flux distribution does not correspond to the true heterogeneous flux distribution, continuity of the flux at node interfaces for the homogenous flux is not required. This being the case, by appropriately selecting the degree of discontinuity of the flux at the node interfaces, the currents at the node interfaces can be made equal to the heterogeneous currents. He introduced the heterogeneity factor *"f"* such that equality of the heterogeneous surface flux at the interface of two adjacent nodes is guaranteed by the following continuity condition,

$$\hat{\phi}_l^+ f_l^+ = \hat{\phi}_{l+1}^- f_{l+1}^- \tag{1-5}$$

where $\hat{\phi}_l^+$ and $\hat{\phi}_{l+1}^-$ represent transverse integrated homogenous surface fluxes in the direction of the solution for right and left surfaces of nodes *l* and *l+1*, respectively. The heterogeneity factor *f* is then defined as,

$$f_l^+ = \frac{\phi_l^+}{\hat{\phi}_l^+} \quad f_{l+1}^- = \frac{\phi_{l+1}^-}{\hat{\phi}_{l+1}^-} \tag{1-6}$$

These equivalence factors provide additional degrees of freedom for us to preserve reaction rates and surface currents simultaneously. Koebke calculated heterogeneity factors by iterating on values of diffusion coefficients such that $f_l^+ = f_{l+1}^-$ is satisfied. This homogenization method is known as 'Equivalence Theory' (E.T.). Smith developed a simpler variation of the Equivalence Theory. He realized that for any value of the diffusion coefficient, heterogeneity factors that preserve the surface average currents can be calculated. Unless diffusion coefficients are calculated iteratively, heterogeneity factors on either side of an interface will be different. Therefore, Smith referred to these parameters as "discontinuity factors" and calculated the homogenous diffusion coefficient by using flux-volume weighting. This method is called Generalized Equivalence Theory (G.E.T.).

1.2.1.4 Super-Nodal Methods

Super-Nodal method introduced by Gamino [21] took nodal methods one step further. The concept behind the Super-Nodal method is to use large mesh sizes ("super nodes") for the nodal solution. Larger mesh sizes allow the use of fewer nodes, resulting in computational savings in computer time and memory. The Equivalence Theory forms the basis of Super-Nodal method. As the first step, a finer mesh, core-wide reference solution is obtained. This solution is used to homogenize super-nodes by calculating homogenization constants. Coarse Mesh Discontinuity Factors (CMDF) are calculated using Generalized Equivalence Theory. These constants are then used in Super-Nodal calculations for subsequent reactor analysis calculations. Gamino showed that for depletion calculations, the Super-Nodal solution can be improved by updating homogenization constants at some burnup steps. The Super-Nodal flux solution is subsequently dehomogenized to obtain approximate fine-mesh fluxes. While Gamino's Super-Nodal scheme is applicable to fuel depletion analysis, further work needs to be accomplished on the updating of homogenization constants during transients for a complete reactor analysis using Super-Nodal methods. As the frequency of the updates increases, errors in the power distribution decrease at the expense of increasing computational cost. Unfortunately, Gamino's work lacks an error bound estimate on the Super-Nodal method, which one would like to calculate in order to achieve specified fidelity with a minimum number of updates and/or spatial nodes.

1.2.1.5 Error Analysis

Due to wide spread applications and simplicity, there have been many years of effort devoted to calculating error bounds and generating adaptive methods in finite element methods (FEM) [22], [23]. Because of this tremendous work, researchers have tried to relate nodal methods to FEM. Fedon-Magnud [24] worked on 2-D NEM and noted that NEM is like FEM based upon piecewise (dis)continous functions used to approximate the flux shape. Fedon-Magnud and his co-authors also proved that any simple polynomial nodal method can be represented as a FEM of nonconforming type. Later, Hennart [25] related ANM to FEM and showed ANM is also a FEM. Penland [26] concentrated on the errors associated with utilizing NEM for the solution of the neutron diffusion equation. He calculated upper bounds for the global error estimate using the mesh doubling technique. Although Smith and Greenman [12] did numerical studies on the error associated with the quadratic leakage fit, there are not many analytical studies on the error presented by the transverse leakage approximations and homogenization.

1.2.1.6 Flux Reconstruction

Modern nodal methods provide accurate results for node average quantities even for highly heterogeneous fuel assemblies [27]. Unfortunately, not only are spatial details lost due to homogenization but also, nodal solutions are decoupled in each direction making it not possible to get pin-wise flux directly from the transverse integrated nodal solution. Point wise flux and power information is vital for reactor safety analysis *e.g.* peak pin-power. Therefore, several methods have been developed to construct finer heterogeneous local flux information within a coarser node. The general idea involving the flux reconstruction is to express heterogeneous pin by pin flux as a product of a two or three dimensional homogenized intra-nodal flux distribution in the polynomial form and local form factors [28]-[30] The coefficients of the multidimensional intra-nodal flux distribution are calculated by forcing the reconstructed solution to preserve the nodal solution quantities such as volume and surface average fluxes, and surface average currents. However, these constraints are inadequate to obtain the intra-nodal flux distribution with adequate accuracy. Corner-point fluxes are introduced as additional constraints; however, they cannot be directly determined using the transverse integrated equations approach and are approximately evaluated in a variety of ways. Many pin-power reconstruction methods differentiate based on the order of the polynomial that is used for reconstruction. There are also more complicated nodal methods which solve the two or three dimensional diffusion equation instead of the transverse integrated one dimensional equation, hence it is possible to get the intra-nodal flux shape directly from the nodal solution [31],[16].

The form factors account for the heterogeneities in the fuel assembly, such as water holes and burnable absorber pins. The form factors are calculated as part of assembly homogenization calculations and they are fuel-color, assembly dependent [28].

The Super-Nodal method employs a similar approach as the pin-power reconstruction method to obtain the fine-mesh node average flux distribution from the coarse mesh flux distribution, enabling calculation of the peak power and its location.

1.3 Scope of Research

The objective of this research is to decrease the computational burden of 3-D neutronics core simulators by implementing the Super-Nodal method into the existing nodal solution strategy. The Super-Nodal algorithm adapts itself well into the nodal algorithms used in the NESTLE [1] and FORMOSA [2] codes. Like most nodal codes, NESTLE and FORMOSA utilize an outer-inner iterative strategy. The analytical nodal method (ANM) is selected for the Super-Nodal scheme since it gives more accurate results compared to NEM at large spatial mesh sizes. A Super-Nodal method is integrated into the NESTLE V6.1 code. NESTLE has been selected as the test bed code since it is based upon ANM; whereas, the FORMOSA series of codes utilizes NEM. The nonlinear iterative approach used to implement nodal methods envelops the outer-inner iteration loop. Coarse mesh and fine mesh iterations are integrated outside the nonlinear iterations without changing the code structure.

In order to represent a reactor core accurately at the coarse mesh level, homogenization parameters are calculated employing the consistent collapsing (CC) technique. Refining (prolongation) and collapsing (restriction) algorithms are developed to reduce homogenization errors during transients. Thermal-Hydraulics and Xe-Sm feedbacks are also treated in CC to enable a realistic reactor core analysis.

It is well known that the ANM solution is near-singular for the nodes that have close to zero leakage. A second type of singularity was discovered during this research at the coarse mesh level for certain core configurations. Addressing these instabilities and investigating limitations of ANM in Super-Nodal methods are essential if one wants to employ a Super-Nodal method in a complete core analysis code. Therefore, two different methods are developed to address these two types of singularities.

The only assumption made in ANM is the transverse leakage shape within the node. If one can provide a better representation of transverse leakage, ANM errors are expected to decrease. In an effort to obtain an ANM solution for the nodes close to singularity, several transverse leakage approximation methods are developed.

In order to improve the Super-Nodal solution, three different approaches are tested to calculate the coarse mesh homogenized diffusion coefficient, which is the weak point of the G.E.T.

Finally, a simple global error estimate technique is developed for switching between fine and coarse mesh layouts during transient calculations.

This chapter has provided a brief explanation of the motivation for this research, as well as background information. Chapter 2 explains the details of the Super-Nodal methodology and gives the theoretical foundations for the methods used in Super-Nodal implementation. Chapter 3 discusses different transverse leakage and diffusion coefficient calculation approaches. Chapter 4 reviews the benchmark problems used and the performance of the Super-Nodal method for different coarse mesh geometries, in addition to comparing collapsing schemes. Finally, in Chapter 5 a summary of the thesis and recommendations on future work are given.

2. Methodology

2.1 Analytical Nodal Method

The Super-Nodal method is employed using the analytical nodal method due to its accuracy for large mesh sizes. Therefore, it is important to understand the ANM methodology to develop the Super-Nodal method. In this section ANM equations, as they are incorporated in NESTLE 6.1, are reviewed. The solution algorithm which employs the so called "two-node problem" is also analyzed. Starting with the three dimensional two group diffusion equation in Cartesian geometry

$$-\vec{\nabla}\cdot \boldsymbol{D}_g\vec{\nabla}\ \boldsymbol{\phi}_g(\boldsymbol{r})+\Sigma_{tg}\boldsymbol{\phi}_g(\boldsymbol{r})=\frac{\chi_g(\boldsymbol{r})}{\boldsymbol{k}}\sum_{g'=1}^{G}\nu\Sigma_{fg'}(\boldsymbol{r})\boldsymbol{\phi}_{g'}(\boldsymbol{r})+\sum_{g'=1}^{G}\Sigma_{sgg'}(\boldsymbol{r})\boldsymbol{\phi}_{g'}(\boldsymbol{r}) \tag{2-1}$$

where *r=(x,y,z)* and integrating over two of three directions, three one dimensional transverse integrated equations are obtained for each direction of Cartesian geometry. For simplicity, only the z-direction relevant equations are presented, recognizing that the other directions have similar equations. Then the *z* direction, transverse integrated diffusion equation for node $l \in (\Delta x,\Delta y,\Delta z)^l$ can be written assuming that the properties are constant within spatial node *l* as,

$$-\frac{d}{dz}D_g^l\frac{d}{dz}\phi_{gz}^l(z)+\Sigma_{tg}^l\phi_{gz}^l(z)-\frac{\chi_g^l}{k}\sum_{g'=1}^{G}\nu_{g'}\Sigma_{fg'}^l\phi_{g'z}^l(z)-\sum_{g'=1}^{G}\Sigma_{sgg'}^l\phi_{g'z}^l(z)=-L^l(z) \tag{2-2}$$

where $\phi_{gz}^l(z)$ is the z direction transverse integrated flux, defined as

$$\phi_{gz}^{l}(z) = \frac{1}{\Delta x \Delta y}\int_{-\Delta x/2}^{\Delta x/2} dx \int_{-\Delta y/2}^{\Delta y/2} dy\, \phi_g(r) \tag{2-3}$$

and $L^l(z)$ is the z direction transverse leakage,

$$L^l(z) = \frac{1}{\Delta x \Delta y}\int_{-\Delta x/2}^{\Delta x/2} dx\left(-D_g^l \frac{\partial}{\partial y}\phi_g^l(r)\right)\Big|_{y=-\Delta y/2}^{y=\Delta y/2} + \frac{1}{\Delta x \Delta y}\int_{-\Delta y/2}^{\Delta y/2} dy\left(-D_g^l \frac{\partial}{\partial x}\phi_g^l(r)\right)\Big|_{x=-\Delta x/2}^{x=\Delta x/2} \tag{2-4}$$

Note that the spatial coordinates are shifted so that the coordinate origin is at node *l*'s center. Solution of Equation (2-2) is separated into homogenous and particular solutions. The homogenous equations are given by,

$$\begin{bmatrix} -D_1 \frac{d^2}{dz^2} + (\Sigma_{r1} - \frac{1}{k}\nu\Sigma_{f1}) & -\frac{1}{k}\nu\Sigma_{f2} \\ -\Sigma_{r1} & -D_2 \frac{d^2}{dz^2} + \Sigma_{r2} \end{bmatrix} \begin{bmatrix} \phi_1^H \\ \phi_2^H \end{bmatrix} = \begin{bmatrix} 0 \\ 0 \end{bmatrix} \tag{2-5}$$

If the homogenous solution is in the form of

$$\bar{\phi}_g^H(z) = \tilde{\phi}_g^H e^{iBz} \tag{2-6}$$

then Equation (2-4) becomes,

$$\begin{bmatrix} -D_1 B^2 + (\Sigma_{r1} - \frac{1}{k}\nu\Sigma_{f1}) & -\frac{1}{k}\nu\Sigma_{f2} \\ -\Sigma_{r1} & -D_2 B^2 + \Sigma_{r2} \end{bmatrix} \begin{bmatrix} \tilde{\phi}_1^H \\ \tilde{\phi}_2^H \end{bmatrix} = \begin{bmatrix} 0 \\ 0 \end{bmatrix} \tag{2-7}$$

For a non-trivial solution the determinant of the coefficient matrix must be zero which leads to

$$(B^2)^2 + \left(\frac{\Sigma_{r2}}{D_2} + \frac{\Sigma_{r1}}{D_1} - \frac{1}{k}\frac{\nu\Sigma_{f1}}{D_1}\right)B^2 + \left(1 - \frac{k_\infty}{k}\right)\frac{\Sigma_{r1}}{D_1}\frac{\Sigma_{r2}}{D_2} = 0 \tag{2-8}$$

where

$$k_\infty = \frac{\nu\Sigma_{f1}}{\Sigma_{r1}} + \frac{\Sigma_{12}}{\Sigma_{r1}}\frac{\nu\Sigma_{f2}}{\Sigma_{r2}} \tag{2-9}$$

The roots of Equation (2-8) are given as

$$\begin{aligned} \kappa^2 &\equiv -b + \sqrt{b^2 - c^2} \\ \mu^2 &\equiv -b - \sqrt{b^2 - c^2} \end{aligned} \tag{2-10}$$

where

$$b \equiv \frac{1}{2}\left(\frac{\Sigma_{r1}}{D_1} + \frac{\Sigma_{r2}}{D_2} - \frac{1}{k}\frac{\nu\Sigma_{f1}}{D_1}\right) \tag{2-11}$$

and

$$c \equiv \left(1 - \frac{k_\infty}{k}\right)\frac{\Sigma_{r1}}{D_1}\frac{\Sigma_{r2}}{D_2} \tag{2-12}$$

Note that $\mu^2<0$ always so μ is always complex; however, the sign of κ^2 can be positive or negative depending on the value of k_∞,

$$\kappa = \begin{cases} |\kappa| & k_\infty > k \\ i|\kappa| & k_\infty \le k \end{cases} \tag{2-13}$$

Thus the homogenous solution is a linear combination of the trial solution, Equation (2-6) for different values of ***B,*** which can be represented by,

$$\phi_g^H(z) = a_{g1}sn(\kappa z) + a_{g2}cn(\kappa z) + a_{g3}sn(\mu z) + a_{g4}cn(\mu z) \tag{2-14}$$

where

$$\boldsymbol{sn}(\kappa z) = \begin{cases} \sin(\kappa z) & \text{if } |\kappa| > \boldsymbol{k}_\infty \\ \sinh(\kappa z) & \boldsymbol{otherwise} \end{cases} \quad , \quad cn(\kappa z) = \begin{cases} \cos(\kappa z) & \text{if } |\kappa| > k_\infty \\ \cosh(\kappa z) & otherwise \end{cases}$$
$$\boldsymbol{sn}(\mu z) = \sinh(\mu z) \quad , \quad \boldsymbol{cn}(\mu z) = \cosh(\mu z) \quad . \tag{2-15}$$

Inserting Equation (2-14) into Equation (2-5) we get

$$\begin{bmatrix} \pm \boldsymbol{D}_1\boldsymbol{\kappa}^2 + \Sigma_{r1} - \frac{1}{\boldsymbol{k}}\nu\Sigma_{r1} & -\frac{1}{\boldsymbol{k}}\nu\Sigma_{f1} \\ -\Sigma_{12} & \pm \boldsymbol{D}_2\boldsymbol{\kappa}^2 + \Sigma_{r2} \end{bmatrix} \begin{bmatrix} \boldsymbol{a}_{11}\boldsymbol{sn}(\kappa z) + \boldsymbol{a}_{12}\boldsymbol{cn}(\kappa z) \\ \boldsymbol{a}_{21}\boldsymbol{sn}(\kappa z) + \boldsymbol{a}_{22}\boldsymbol{cn}(\kappa z) \end{bmatrix} +$$
$$\begin{bmatrix} \pm \boldsymbol{D}_1\mu^2 + \Sigma_{r1} - \frac{1}{\boldsymbol{k}}\nu\Sigma_{r1} & -\frac{1}{\boldsymbol{k}}\nu\Sigma_{f1} \\ -\Sigma_{12} & -\boldsymbol{D}_2\mu^2 + \Sigma_{r2} \end{bmatrix} \begin{bmatrix} \boldsymbol{a}_{13}\boldsymbol{sn}(\mu z) + \boldsymbol{a}_{14}\boldsymbol{cn}(\mu z) \\ \boldsymbol{a}_{23}\boldsymbol{sn}(\mu z) + \boldsymbol{a}_{24}\boldsymbol{cn}(\mu z) \end{bmatrix} = \begin{bmatrix} 0 \\ 0 \end{bmatrix} \tag{2-16}$$

Recognizing that this equation must hold for all values of z this implies that equality must hold for each trigonometric or hyperbolic trigonometric function separately. By setting each of the four terms to zero, fast to thermal flux ratios of like expansion coefficients are determined, where

$$r \equiv \frac{a_{11}}{a_{21}} = \frac{a_{12}}{a_{22}} = \frac{\pm D_2\kappa^2 + \Sigma_{r2}}{\Sigma_{12}} \tag{2-17}$$

and

$$s \equiv \frac{a_{13}}{a_{23}} = \frac{a_{14}}{a_{24}} = \frac{-D_2\mu^2 + \Sigma_{r2}}{\Sigma_{12}} \tag{2-18}$$

These ratios allow us to represent fast flux coefficients in terms of the thermal flux coefficients. They will be used extensively in the rest of the derivation for simplicity. In the next step the particular solution is derived. The particular solution of Equation (2-2) comes from the form of the transverse leakage function on the right hand side. As briefly discussed in Chapter 1, a quadratic polynomial is used to approximate the intra-nodal transverse leakage shape as follows,

$$L_g(z) = \overline{L}_g + b_{g1} f_1(z) + b_{g2} f_2(z) \tag{2-19}$$

where

$$\begin{aligned} f_1(z) &= \frac{z}{\Delta z} \\ f_2(z) &= 3\left(\frac{z}{\Delta z}\right)^2 - \frac{1}{4} \end{aligned} \tag{2-20}$$

These basis functions are selected to satisfy,

$$\int_{-\Delta z/2}^{\Delta z/2} \boldsymbol{f_p}(z)\boldsymbol{dz} = 0 \;\; p{=}1{,}2 \quad \boldsymbol{f}_1\left(\pm\frac{1}{2}\right) = \pm\frac{1}{2}, \;\; \boldsymbol{f}_2\left(\pm\frac{1}{2}\right) = \frac{1}{2} \tag{2-21}$$

Since the non-homogenous term is a quadratic function, the particular solution has to be a quadratic function. Finally, using the same basis functions, the particular solution can be represented as,

$$\boldsymbol{\phi_g^p}(z) = \boldsymbol{c}_{g0} + \boldsymbol{c}_{g1} \boldsymbol{f}_1(z) + \boldsymbol{c}_{g2} \boldsymbol{f}_2(z) \tag{2-22}$$

Using Equations (2-17) and (2-18) the form of the flux distribution is given as

$$\begin{bmatrix} \boldsymbol{\phi}_1(z) \\ \boldsymbol{\phi}_2(z) \end{bmatrix} = \begin{bmatrix} \boldsymbol{r} & \boldsymbol{s} \\ 1 & 1 \end{bmatrix} \begin{bmatrix} \boldsymbol{a}_{21}\boldsymbol{sn}(\kappa z) + \boldsymbol{a}_{22}\boldsymbol{cn}(\kappa z) \\ \boldsymbol{a}_{23}\boldsymbol{sn}(\mu z) + \boldsymbol{a}_{24}\boldsymbol{cn}(\mu z) \end{bmatrix} + \begin{bmatrix} \boldsymbol{c}_{10} + \boldsymbol{c}_{11}\boldsymbol{f}_1(z) + \boldsymbol{c}_{12}\boldsymbol{f}_2(z) \\ \boldsymbol{c}_{20} + \boldsymbol{c}_{21}\boldsymbol{f}_1(z) + \boldsymbol{c}_{22}\boldsymbol{f}_2(z) \end{bmatrix} \tag{2-23}$$

The coefficients of the particular solution, *i.e.* c_{gm} *m=0,1,2,* in Equation (2-23) are calculated by inserting Equation (2-22) into Equation (2-2) and forcing the same order basis functions to satisfy the balance equations. Two sets of equations are obtained as,

$$\begin{bmatrix} \Sigma_{r1} - \frac{1}{k}\nu\Sigma_{f1} & -\frac{1}{k}\nu\Sigma_{f2} \\ -\Sigma_{r1} & \Sigma_{r2} \end{bmatrix} \begin{bmatrix} c_{1m} \\ c_{2m} \end{bmatrix} = \begin{bmatrix} -b_{1m} \\ -b_{2m} \end{bmatrix} \quad m=1,2 \tag{2-24}$$

and

$$\begin{bmatrix} \Sigma_{r1} - \frac{1}{k}\nu\Sigma_{f1} & -\frac{1}{k}\nu\Sigma_{f2} \\ -\Sigma_{r1} & \Sigma_{r2} \end{bmatrix} \begin{bmatrix} c_{10} \\ c_{20} \end{bmatrix} = \begin{bmatrix} -\overline{L}_1 \\ -\overline{L}_2 \end{bmatrix} + \frac{6}{h_x^2} \begin{bmatrix} D_1 c_{12} \\ D_2 c_{22} \end{bmatrix} \tag{2-25}$$

The remaining coefficients in Equation (2-23) belong to the homogeneous solution and they are obtained from the “two-node problem” explained in the next section.

2.1.1 Two-Node Problem

NESTLE 6.1 employs the non-linear iterative strategy to reduce computer run time and memory requirements [32]. The main idea is to solve the diffusion equation using the Finite Difference Method (FDM), and during the outer iterations update the FDM diffusion coupling coefficients after each ΔN number of outer iterations so as to preserve the ANM estimated net surface currents. This iterative approach is convergent and forces the FDM solution to yield a better estimate of the surface currents consistent with values calculated by ANM. ANM calculates the net surface currents performing the so called “two-node problem” calculation for every interface for all nodes and in all directions.

The two-node problem is simply a spatially decoupled nodal calculation spanning two adjoining nodes. Each two-node problem produces two-group surface currents between the two nodes. In this section, the solution of the two-node problem is derived using the ANM solution described in Section 2.1. For a two-node problem in *z* direction between nodes *l* and *l+1*, the coordinate system is shown as

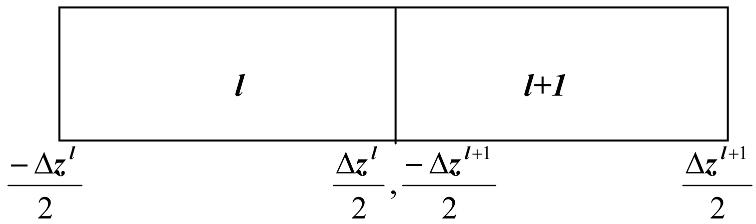

Figure 2.1 Two-Node Problem

There are 8 unknowns in this two-node problem which corresponds to the 4 coefficients of the homogenous flux in Equation (2-23) per node. The node average flux, criticality constant and transverse leakage function are known from the previous FDM iteration along with the cross sections. In order to have a complete solution, 8 equations are required and they are obtained demanding the intra-nodal flux shape in both nodes to satisfy the following constraints,

- Node average flux.

$$\bar{\phi}_g^{q} = \frac{1}{\Delta z^{q}} \int_{-\Delta z^{q}/2}^{\Delta z^{q}/2} \phi_g^{q}(z)\,dz \quad q \in \{l, l+1\} \tag{2-26}$$

- Surface averaged heterogeneous flux continuity at the adjoining interface between the two nodes

$$f_g^{l+}\phi_g^{l+} = f_g^{l+1-}\phi_g^{l+1-} \tag{2-27}$$

where $\phi_g^{l+} = \phi_g^{l}\left(\frac{\Delta z^{l}}{2}\right)$ and $\phi_g^{l+1-} = \phi_g^{l+1}\left(-\frac{\Delta z^{l}}{2}\right)$ are homogenous surface fluxes for node *l* and *l+1,* respectively. The f_g^{l+} and f_g^{l+1-} represent discontinuity factors as they are defined in Equation (1-6) for right and left surfaces of node *l* and *l+1,* respectively.

- Surface averaged net current continuity at the adjoining interface between the two nodes.

$$
-D_g^l \left. \frac{d^2\phi_g^l(z)}{dz^2} \right|_{\frac{\Delta z^l}{2}} = -D_g^{l+1} \left. \frac{d^2\phi_g^{l+1}(z)}{dx^2} \right|_{-\frac{\Delta z^{l+1}}{2}} \tag{2-28}
$$

Note that none of the constraints couples the two-node to any other node than each other. This feature allows us to solve a two-node problem for each surface independently, reducing storage requirements and the CPU time.

The even numbered coefficients of Equation (2-23) are calculated by inserting Equation.(2-23) into Equation (2-26) and solving the following 2x2 matrix

$$
\begin{bmatrix} r\dfrac{sn(\kappa_{1/2})}{\kappa_{1/2}} & s\dfrac{sn(\mu_{1/2})}{\mu_{1/2}} \\ \dfrac{sn(\kappa_{1/2})}{\kappa_{1/2}} & \dfrac{sn(\mu_{1/2})}{\mu_{1/2}} \end{bmatrix} \begin{bmatrix} a_{22} \\ a_{24} \end{bmatrix} = \begin{bmatrix} \bar{\phi}_1 - c_{10} \\ \bar{\phi}_2 - c_{20} \end{bmatrix} \tag{2-29}
$$

where $\kappa_{1/2} \equiv \kappa \dfrac{\Delta z}{2}$ and $\mu_{1/2} \equiv \mu \dfrac{\Delta z}{2}$. The solution of the remaining odd numbered coefficients in each node is obtained when Equation.(2-23) is inserted in Equation (2-27) and Equation (2-28) as follow,

$$
\begin{bmatrix}
f_1^l r^l sn(\kappa_{1/2}^l) & f_1^l s^l sn(\mu_{1/2}^l) & f_1^{l+!} r^{l+1} sn(\kappa_{1/2}^{l+1}) & f_1^{l+1} s^{l+1} sn(\mu_{1/2}^{l+1}) \\
f_2^l sn(\kappa_{1/2}^l) & f_2^l sn(\mu_{1/2}^l) & f_2^l sn(\mu_{1/2}^l) & f_2^{l+1} sn(\mu_{1/2}^{l+1}) \\
-D_1^l r^l \kappa^l cn(\kappa_{1/2}^l) & -D_1^l s^l \mu^l cn(\kappa_{1/2}^l) & D_1^{l+1} r^{l+1} \kappa^{l+1} cn(\kappa_{1/2}^{l+1}) & D_1^{l+1} s^{l+1} \mu^{l+1} cn(\mu_{1/2}^{l+1}) \\
-D_2^l \kappa^l cn(\kappa_{1/2}^l) & -D_2^l \mu^l cn(\mu_{1/2}^l) & D_2^{l+1} \kappa^{l+1} cn(\kappa_{1/2}^{l+1}) & D_2^{l+1} \mu^{l+1} cn(\mu_{1/2}^{l+1})
\end{bmatrix}
\begin{bmatrix} a_{21}^l \\ a_{21}^l \\ a_{21}^l \\ a_{21}^l \end{bmatrix} =
$$

$$
\begin{bmatrix}
-f_1^l r^l cn(\kappa_{1/2}^l) & f_1^l s^l cn(\mu_{1/2}^l) & f_1^{l+!} r^{l+1} cn(\kappa_{1/2}^{l+1}) & f_1^{l+1} s^{l+1} cn(\mu_{1/2}^{l+1}) \\
-f_2^l cn(\kappa_{1/2}^l) & f_2^l cn(\mu_{1/2}^l) & f_2^l cn(\mu_{1/2}^l) & f_2^{l+1} cn(\mu_{1/2}^{l+1}) \\
\mp D_1^l r^l \kappa^l cn(\kappa_{1/2}^l) & D_1^l s^l \mu^l sn(\kappa_{1/2}^l) & \mp D_1^{l+1} r^{l+1} \kappa^{l+1} sn(\kappa_{1/2}^{l+1}) & D_1^{l+1} s^{l+1} \mu^{l+1} sn(\mu_{1/2}^{l+1}) \\
\mp D_2^l \kappa^l cn(\kappa_{1/2}^l) & D_2^l \mu^l sn(\mu_{1/2}^l) & \mp D_2^{l+1} \kappa^{l+1} sn(\kappa_{1/2}^{l+1}) & D_2^{l+1} \mu^{l+1} sn(\mu_{1/2}^{l+1})
\end{bmatrix}
\begin{bmatrix} a_{21}^l \\ a_{24}^l \\ a_{21}^{l+1} \\ a_{24}^{l+1} \end{bmatrix}
+ \begin{bmatrix}
f_1^{l+1}\phi_1^{Pl+1-} - f_1^l \phi_1^{Pl-} \\
f_2^{l+1}\phi_2^{Pl+1-} - f_2^l \phi_2^{Pl-} \\
J_1^{Pl+1-} - J_1^{Pl+} \\
J_2^{Pl+1-} - J_2^{Pl+}
\end{bmatrix} \tag{2-30}
$$

where $\boldsymbol{\phi}_g^{Pl+} = \boldsymbol{\phi}_g^{Pl}\left(\frac{\Delta \boldsymbol{z}^{l}}{2}\right)$ and $\boldsymbol{\phi}_g^{Pl+1-} = \boldsymbol{\phi}_g^{Pl+1}\left(-\frac{\Delta \boldsymbol{z}^{l+1}}{2}\right)$.

Surface averaged currents are calculated from the solutions of the two-node problems. These ANM evaluated surface currents are used to correct the FDM coupling coefficients by adding a correction term to the FDM surface current expression as following,

$$J_{gz}^{l+} = -\frac{C_{gz}^{l+}}{\frac{\Delta z^{l} + \Delta z^{l+1}}{2}}\left[\overline{\phi}_g^{\,l+1} - \overline{\phi}_g^{\,l}\right] - \frac{\widetilde{D}_{gz}^{l+}}{\frac{\Delta z^{l} + \Delta z^{l+1}}{2}}\left[\overline{\phi}_g^{\,l+1} + \overline{\phi}_g^{\,l}\right] \tag{2-31}$$

The first term on the RHS is the normal FDM approximation for the surface current using a box scheme, where $\boldsymbol{C}_{gz}^{l+}$ is the original FDM coupling coefficient defined as,

$$C_{gz}^{l+} = \frac{D_g^{l} D_g^{l+1}(\Delta z^{l} + \Delta z^{l+1})}{D_g^{l}\Delta z^{l} + D_g^{l+!}\Delta z^{l+1}} \tag{2-32}$$

After each ANM calculation, $\widetilde{\boldsymbol{D}}$ values are calculated to accurately express the surface currents in terms of node average fluxes in the FDM solution.

2.2 Super-Nodal Method

2.2.1 Super-Nodal Algorithm

The essence of the Super-Nodal algorithm is to have two distinct grid layouts, fine and coarse grids, and to provide the necessary homogenization parameters for the coarse grid from the fine grid reference solution. This strategy is analogous to what assembly calculations mean for the fine grid FDM and ANM solution. Here, instead of using zero current assembly based homogenization, a more detailed reactor wise solution is provided for the homogenization. The algorithm has five main steps, which will be explained in more detail in the following sections. The first step is to obtain a fine mesh reference solution at $t=0$ s before the transient calculation start. The second step is the homogenization or the collapsing step. In this step the reference solution is used to calculate the coarse mesh, discontinuity factors and coarse mesh cross sections, Xe-Sm and delay neutron precursor number densities, and thermal-hydraulic properties. The transient reactor analysis calculations are performed for each time step at the coarse mesh level in the third step. The fourth step is the refining or dehomogenization step. If the error in the coarse mesh solution increases due to deviations from the reference solution *e.g*. large control rod movement, then a fine grid level solution is completed using the coarse mesh solution as the initial iterative estimate for the fine mesh solution. The fifth and last step involves re-updating coarse mesh homogenization parameters using the fine mesh reference solution obtained in step 4. The transient reactor analysis calculation then continues at the coarse mesh level for the next time-step. The fifth step is similar to the second step. The last two steps are performed as often as needed to reduce the coarse mesh errors. A summary of the Super-Nodal algorithm is shown in Figure 2.2.

2.2.2 Spatial Homogenization

Calculation of the homogenization parameters is an important step for the implementation of a nodal method. If one wants to represent the fine mesh heterogeneous volume averaged nodal solution at the coarse mesh level, integral quantities such as node-averaged reaction rates, criticality constant, and surface average currents should be preserved at the coarse mesh level. G.E.T. accomplishes this and is employed as the basis for the Super-Nodal method. For a complete reactor analysis at the coarse mesh level, thermal-hydraulics (T-H), precursor number densities, and transient fission products must be also treated.

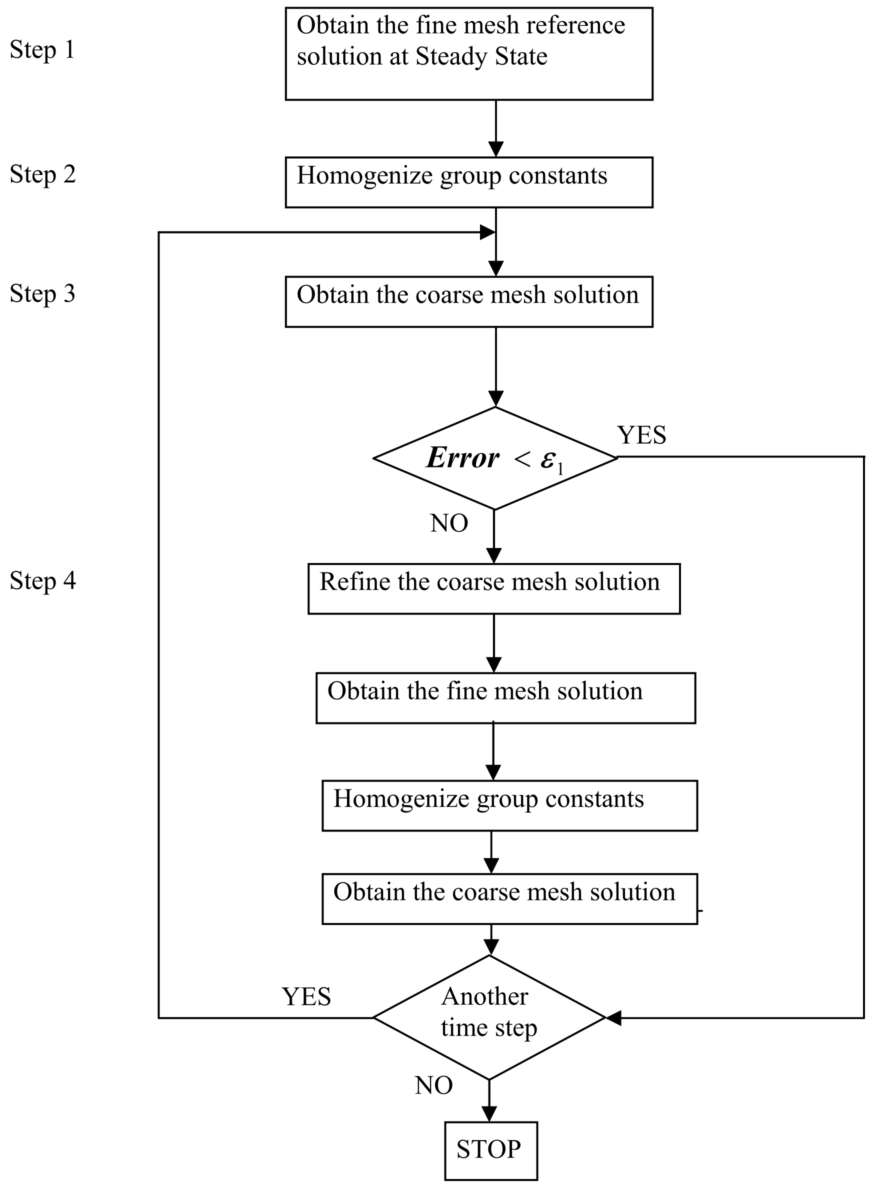

Figure 2.2 Basic Super-Nodal Algorithm

2.2.2.1 Neutron Cross Section Homogenization

Generalized Equivalence Theory (G.E.T.) preserves the total reaction rates inside a coarse node for each type of reaction in the diffusion equation by employing flux-volume weighted cross sections. As an example, the homogenized absorption cross section is determined from,

$$\hat{\Sigma}_{\alpha g}^{N} = \frac{\sum_{i} \Sigma_{\alpha g}^{i} \phi_{g}^{i} \Delta V^{i}}{\hat{\phi}_{g}^{N} \Delta \hat{V}^{N}} \quad g = 1,2\,; i \in N \tag{2-33}$$

where $\Sigma_{\alpha g}^{i}$ and ΔV^{i} are the finer mesh absorption cross section and volume of node i which is associated with the super-node N, and "^" denotes the homogenized values.

To treat thermal-hydraulic feedback effects on the cross sections, the consistent collapse of Taylor series expansion coefficients for the cross-sections in terms of thermal-hydraulic parameters can be determined by utilizing the T-H conditions as predicted by the coarse mesh T-H model. Taylor series expansion of the cross sections for node l in terms of coolant density, coolant temperature, effective fuel temperature and soluble poison density is formulated in NESTLE 6.1 as

$$\Sigma_{\alpha g}^{l} = a_{1\alpha g}^{l} + \sum_{j=2}^{3} a_{j\alpha g}^{l} \left(\Delta\rho_{C}^{l}\right)^{j-1} + a_{4\alpha g}^{l} \Delta T_{C}^{l} + a_{5\alpha g}^{l} \Delta\sqrt{T_{F_{eff}}^{l}} + \sum_{j=6}^{8} a_{j\alpha g}^{l} \left(\Delta N_{sp}^{l}\right)^{j-5} \tag{2-34}$$

where

$\Sigma_{\alpha g}^{l}$ = macroscopic cross section for reaction type α, and group g

$a_{j\alpha g}^{l}$ = j-th expansion coefficient for reaction type α, and group g

$\Delta\rho_{C}^{l}$ = change in the coolant density from reference solution.

ΔT_{C}^{l} = change in coolant temperature from reference solution

$\Delta\sqrt{T^l_{F_{eff}}}$ = change in square root of effective fuel temperature from reference solution

ΔN^l_{sp} = change in soluble poison number density from reference solution

As an example, the coarse mesh coefficients of change in coolant density are calculated as shown in Equation (2-35). The rest of the cross section expansion coefficients are calculated in a similar manner by using related thermal-hydraulic properties for weighting.

$$\hat{a}^N_{j\alpha g} = \frac{\sum_i a^i_{j\alpha g}\left(\Delta\rho^i_C\right)^{j-1}\phi^i_g\Delta V^i}{\left(\Delta\hat{\rho}^N_C\right)^{j-1}\hat{\phi}^N_g\Delta\hat{V}^N} \quad g = 1,2\,;\, i \in N \tag{2-35}$$

2.2.2.2 Xe-Sm Feedback

The absorption cross-section includes a correction term for the transient fission products. The correction comes from contributions of Xe^{135} and Sm^{149} to neutron absorption. The total macroscopic absorption cross-section is calculated from,

$$\widetilde{\Sigma}^l_{ag} = \Sigma^l_{ag} + \Delta\Sigma^l_{Xe_{ag}} + \Delta\Sigma^l_{Sm_{ag}} \tag{2-36}$$

where

$$\begin{aligned} \Delta\Sigma^l_{Xe_{ag}} &= \sigma^l_{Xe_{ag}} N^l_{Xe} \\ \Delta\Sigma^l_{Sm_{ag}} &= \sigma^l_{Sm_{ag}} N^l_{Sm} \end{aligned} \tag{2-37}$$

with N^l_{Xe} and N^l_{Sm} denoting the Xe^{135} and Sm^{149} number densities for node *l*. The Xe^{135} and Sm^{149} microscopic cross sections, $\sigma^l_{Xe_{ag}}$ and $\sigma^l_{Sm_{ag}}$ are represented and evaluated in exactly the same manner as the macroscopic cross-sections. The number densities are determined by solving the I^{135} - Xe^{135} and Pm^{149}- Sm^{149} chain depletion equations. The time dependent Xe^{135} number density is given by

$$\frac{d}{dt} N_{Xe}^{l}(t) = \lambda_I N_I^{l}(t) + \gamma_{Xe}^{l} \sum_{g=1}^{2} \Sigma_{fg}^{l}(t)\phi_g^{l}(t) - \lambda_{Xe} N_{Xe}^{l}(t) \\ - \sum_{g=1}^{2} \sigma_{Xe_{ag}}^{l}(t)\phi_g^{l}(t) N_{Xe}^{l}(t) \tag{2-38}$$

where

$N_i^l(t)$ = nuclei number density of isotope *i*

$\sigma_{i_{ag}}^{l}(t)$ = microscopic absorption cross section of isotope *i*

$\Sigma_{fg}(t)$ = macroscopic fission cross section

γ_i^l = effective yield of isotope *i*

λ_i = decay constant of isotope *i*

The depletion equations for I^{135}, $Pm^{149}$and Sm^{149} are expressed in a similar manner.

At the coarse mesh level, the number densities of fission products are preserved. The coarse mesh number densities are calculated using volume weighting.

$$\hat{N}_{Xe}^{N} = \frac{\sum_i N_{Xe}^{i} \Delta V^{i}}{\Delta \hat{V}^{N}} \tag{2-39}$$

The effective yields are collapsed with flux-volume and fission cross-section weighting to preserve the number density balance in Equation (2-38) as follows

$$\hat{\gamma}_{Xe}^{N} = \frac{\sum_i \gamma_{Xe}^{N} \Sigma_{fg}^{i} \phi_g^{i} \Delta V^{i}}{\hat{\Sigma}_{fg}^{N} \hat{\phi}_g^{N} \Delta \hat{V}^{N}} \tag{2-40}$$

The I^{135}, $Pm^{149}$and Sm^{149} number densities and effective yields are collapsed using the same approach.

2.2.2.3 Thermal-Hydraulic Feedback

NESTLE uses a thermal-hydraulic (T-H) model which models single and two phase coolant flow up a closed coolant channel. A Homogenous Equilibrium Mixture (HEM) model is employed, limiting model applicability to low quality fluids where slip does not occur. The system of equations, which describe the average conditions within the flow channel, are obtained from the mass continuity and energy conservation equations given by Equations (2-41) and Equation (2-42) assuming pressure to be constant.

$$A_C^l \frac{\partial}{\partial t} \rho_C^l = -\frac{\partial}{\partial z}\left(G_C^l A_C^l\right) \tag{2-41}$$

$$A_C^l \frac{\partial}{\partial t} \rho_C^l u_C^l = -\frac{\partial}{\partial z}\left(G_C^l A_C^l u_C^l\right) - P \frac{\partial}{\partial z}\left(\frac{G_C^l A_C^l}{\rho_C^l}\right) + q_S^{\prime\prime l} S_F^l + \dot{q}_C^l A_C^l \tag{2-42}$$

where

ρ_C^l = coolant density

G_C^l = coolant mass flux

U_C^l = coolant internal energy

$\dot{q}_C^l$ = volumetric power density from hear deposited directly in the coolant

$q_S^{\prime\prime l}$ = fuel rod surface heat flux into the coolant

A_C^l = total cross-sectional area for coolant flow within the node

S_F^l = total fuel rod surface area per unit axial length within the node

P = coolant pressure

The surface fuel temperature, which is required to be calculated in order to correct cross-sections for Doppler broadening, is expressed as a function of average fuel temperature. The average fuel temperature is calculated using a lumped parameter model as indicated by Equation (2-43)

$$\rho_F c_{PF}^l \frac{\partial T_F^l}{\partial t} V_F^l = Q_F^l + h_{eff}^l V_F^l (T_C^l - T_F^l) \tag{2-43}$$

where

T_C^l = average coolant temperature

T_F^l =average fuel temperature

V_F^l =fuel volume

$\dot{Q}_F^l$ =power from heat deposited directly in the fuel

Equations (2-41) through (2-43) are coupled and non-linear in nature since ρ_C^l and T_C^l are functions of U_C^l. Hence T-H equations are solved iteratively in NESTLE's nested iteration scheme [40]. For transient problems a semi-implicit time treatment is employed.

Two different approaches are developed to obtain coarse mesh T-H properties. In the first approach, collapsed fine mesh reference T-H properties are used as initial estimates and Equations (2-41) through (2-43) are iterated until converged coarse mesh T-H properties are obtained for *t=0* time step. At each time step thereafter, coarse mesh T-H calculations are performed in the nested iteration scheme. The second approach is to use the fine mesh grid to solve Equations (2-41) through (2-43). This is done by continuing to perform the T-H calculations at the fine mesh level for each time step and collapsing the fine mesh T-H parameters at the end of each T-H update to calculate coarse mesh T-H feedback properties.

In both approaches the collapsing of fine mesh T-H properties is performed as follows:

a) Fuel and water fractions are collapsed by preserving total water and fuel volumes in the coarse node, respectively.

$$\hat{W}_C^N = \frac{\sum_i W_C^i V^i}{\hat{V}^N} \qquad \hat{W}_F^N = \frac{\sum_i W_F^i V^i}{\hat{V}^N} \tag{2-44}$$

b) Internal energy is collapsed preserving the node energy flux.

$$\hat{U}_C^N = \frac{\sum_i U_C^i G^i A_C^i}{\hat{G}^N \hat{A}_C^N} \tag{2-45}$$

c) Coolant density is collapsed by preserving the total coolant mass in the node.

$$\hat{\rho}_C^N = \frac{\sum_i \rho_C^i A_C^i \Delta z^i}{\hat{A}_C^N \Delta \hat{z}^N} \tag{2-46}$$

d) Fuel temperature is collapsed by preserving the fuel internal energy

$$\hat{T}_F^N = \frac{\sum_i T_F^i \rho_F^i V_F^i c_{PF}^i}{\hat{\rho}_F^N \hat{V}_F^N \hat{c}_{PF}^N} \tag{2-47}$$

The second approach requires fine mesh power densities to be known in order to calculate fine mesh T-H properties. Therefore, a dehomogenization step is performed before each T-H update and the fine mesh power densities are calculated from coarse mesh power densities. The dehomogenization step is explained in detail in the next section.

2.2.3 Spatial Dehomogenization

During the coarse mesh calculation an estimate of the fine mesh flux is required for several reasons such as peak power calculation, updating of cross-sections, error analysis and T-H update. There are several polynomial based fine mesh or pin-power reconstruction methods in the literature mentioned in Chapter 1. The most popular ones construct the pin-wise flux estimate as a product of a polynomial interpolation function and assembly form factor (FF), which is defined as

$$\boldsymbol{FF_g^i} = \frac{\Phi_g^i}{\hat{\Phi}_g^N} \ldots i \in N \tag{2-48}$$

where Φ_g^i is the average flux in pin-wise region i of assembly N and $\hat{\Phi}_g^N$ is the assembly average flux. The form factors come from assembly calculations while the coefficients of the interpolation polynomial are calculated from nodal properties. Since only axial collapsing is examined in this thesis a simple reconstruction algorithm is used. The fine mesh node average flux for group g in node i is calculated employing form factor FF_g^i and the available axial intra-nodal flux shape as following,

$$\phi_g^i = FF_g^i \int_{z_{i-1}}^{z_i} \hat{\phi}_g^N(z)dz \ldots i \in N \tag{2-49}$$

where z_i, z_{i-1} are fine mesh node boundaries and $\hat{\phi}_g^N(z)$ is the transverse integrated coarse mesh flux shape in the z direction. The form factors $\{FF_g^i\}$ are calculated during collapsing at $t=0$ and can be updated if any refine-collapse step is performed.

The reconstructed fine mesh flux estimate does not preserve the coarse mesh node average flux if the form factors are not exact for that iteration. Therefore, fine mesh node average fluxes calculated in Equation (2-49) are rebalanced for consistency as,

$$\tilde{\phi}_g^i = \frac{FF_g^i \int_{z_{i-1}}^{z_i} \hat{\phi}_g^N(z)dz}{R_g^N} \ldots i \in N \tag{2-50}$$

where

$$R_g^N = \frac{\sum_i \phi_g^i \Delta z^i}{\hat{\phi}_g^N \Delta z^N} \ldots i \in N \tag{2-51}$$

2.2.4 One-Node Problem and Discontinuity Factors

The other term in the volume averaged diffusion equation that must be preserved for consistent collapsing is the leakage term. However, it is not trivial to calculate a diffusion coefficient[50] (discussed in Chapter 3) which preserves surface average fine mesh currents for the coarsened node. Simply, the nodal solution does not have enough degrees of freedom to preserve the reaction rates and surface averaged currents at the same time for a coarse node. In CC, CMDFs are utilized in a similar manner to Assembly Discontinuity Factors (ADF) in the assembly homogenization calculations. While ADFs correct for purely homogenization, CMDFs in addition to homogenization errors correct for errors that originate from the coarse mesh transverse leakage and thermal-hydraulic calculations.

The CMDFs are determined by solving the transverse integrated diffusion equation, one coarse node at a time ("one-node problem"). This is done by utilizing the homogenized cross-sections and imposing the finer mesh determined, coarse mesh surface average currents as boundary condition. The coarse mesh surface fluxes calculated from the one-node problem and finer mesh surface fluxes, both for the homogenous system, are inserted into the following equation to calculate the Super-Nodal CMDFs,

$$\hat{\boldsymbol{f}}_{gu}^{N\pm} = \frac{\sum_{i \in S^N} \boldsymbol{f}_{gu}^{i\pm} \boldsymbol{\phi}_{gu}^{i\pm} \boldsymbol{A}_u^{i\pm}}{\hat{\boldsymbol{\phi}}_{gu}^{N\pm} \hat{\boldsymbol{A}}_u^{N\pm}} \quad u = x, y, z\,;\, g = 1,2\,;\, i \in S^N \tag{2-52}$$

where $\boldsymbol{f}_{gu}^{i\pm}$, ϕ_{gu}^{i}, A_u^i are finer mesh ADF, surface flux and surface area, respectively, in the u direction for node i associated with the related surface of coarse node N. The ADFs appearing in the numerator originate from the original homogenization of the lattice.

The solution of the "one-node" problem is similar to the solution of the "two-node" problem presented in Section 2.1. For the coarse mesh transverse integrated flux shape for the z direction given below,

$$\phi_{gz}^{l}(z) = a_{g1}^{l} sn(\kappa^{l} z) + a_{g2}^{l} cn(\kappa^{l} z) + a_{g3}^{l} sn(\mu^{l} z) + a_{g4}^{l} cn(\mu^{l} z) + \sum_{i=0}^{2} c_{gi}^{l} f_i(z) \tag{2-53}$$

first the particular solution coefficients, $\boldsymbol{c}_{gi}^{l}$ are calculated inserting transverse leakage coefficients in Equation (2-24) and (2-25). The even coefficients of the homogenous solution $\boldsymbol{a}_{g2}^{l}$ and $\boldsymbol{a}_{g4}^{l}$ are calculated from the coarse mesh node average flux $\hat{\boldsymbol{\phi}}_{g}^{N}$ and ratios of fast to thermal group expansion coefficients as indicated by Equation (2-29). The remaining odd coefficients of the intra-nodal flux are obtained by first demanding the left (-) surface average current for each group to preserve the fine mesh prediction of this current, expressed as

$$\hat{\boldsymbol{J}}_{g}^{N-} = \frac{\sum_{i \in S^N} \boldsymbol{J}_{g}^{i-} \boldsymbol{A}^{i-}}{\hat{\boldsymbol{A}}^{N-}} \quad u = x, y, z\,;\, g = 1,2\,;\, \boldsymbol{i} \in \boldsymbol{S}^{N-} \tag{2-54}$$

Using Fick's Law for the surface current,

$$\hat{J}_g^{N-} = -\hat{D}_g^N \frac{d}{dz}\phi_g^N(z)\bigg|_{-\Delta z/2} \quad g = 1,2\,, \tag{2-55}$$

substituting Equation (2-53) into this equation, and using the known ratios of the fast and thermal group expansion coefficients, we obtain the equation for the odd coefficients,

$$\begin{bmatrix} -\hat{D}_1 r\kappa\cos(\kappa\frac{\Delta z}{2}) & -\hat{D}_1 s\mu\cosh(\mu\frac{\Delta z}{2}) \\ -\hat{D}_2\kappa\cos(\kappa\frac{\Delta z}{2}) & -\hat{D}_2\mu\cosh(\mu\frac{\Delta z}{2}) \end{bmatrix} \begin{bmatrix} a_{21} \\ a_{23} \end{bmatrix} = \begin{bmatrix} \hat{J}_1^- \\ \hat{J}_2^- \end{bmatrix} + \begin{bmatrix} C_1 \\ C_2 \end{bmatrix} \tag{2-56}$$

where

$$\begin{bmatrix} C_1 \\ C_2 \end{bmatrix} = \begin{bmatrix} -D_1\left(\frac{3c_{12}}{\Delta z} + a_{22} r\kappa\cos(\kappa\frac{\Delta z}{2}) - a_{24} s\mu\cosh(\mu\frac{\Delta z}{2})\right) \\ -D_2\left(\frac{3c_{12}}{\Delta z} + a_{22}\kappa\cos(\kappa\frac{\Delta z}{2}) - a_{24}\mu\cosh(\mu\frac{\Delta z}{2})\right) \end{bmatrix} \tag{2-57}$$

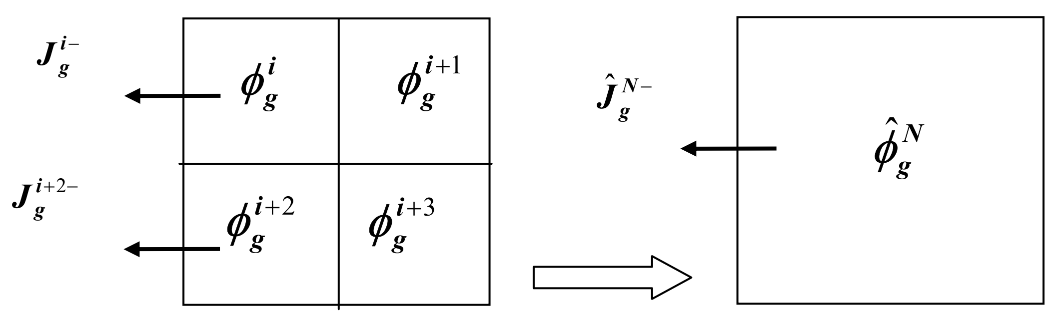

Figure 2.3 "One-Node " Problem Boundary Conditions

2.2.5 Singularity Treatment

In this section, numerical singularities associated with the ANM method are described and two different remedies for two types of singularities are introduced. In general singularities in ANM originate from the form of the transverse integrated diffusion equation in Equation (2-2). Recall in the transverse integrated diffusion equation that the transverse leakage term is moved to the right hand side, and the homogenous and the particular equations are solved separately. Then, the homogenous equation represents a node with zero leakage in the transverse directions. Therefore, a non-critical node can be critical in the absence of transverse leakages and the homogenous equation can have an infinite number of solutions.

2.2.5.1 Zero buckling Singularity

This type of singularity is seen in the nodes with very low leakage. For very low leakage nodes k_∞ of the node approaches k_{eff} of the core. As seen in Equations (2-12) and (2-10) as k_∞ gets closer to k_{eff} one of the roots of the buckling term κ approaches zero. The singularity occurs in the coefficient matrix of the even coefficients of the flux distribution given in Equation (2-29).

$$\begin{bmatrix} r\dfrac{sn(\kappa_{1/2})}{\kappa_{1/2}} & s\dfrac{sn(\mu_{1/2})}{\mu_{1/2}} \\ \dfrac{sn(\kappa_{1/2})}{\kappa_{1/2}} & \dfrac{sn(\mu_{1/2})}{\mu_{1/2}} \end{bmatrix} \begin{bmatrix} a_{22} \\ a_{24} \end{bmatrix} = \begin{bmatrix} \bar{\phi}_1 - c_{10} \\ \bar{\phi}_2 - c_{20} \end{bmatrix} \tag{2-29}$$

As the κ value approaches zero, the sine component goes to zero while the hyperbolic component goes to infinity. Smith [10] developed a fix for this problem by using truncated Taylor series expansion of the analytical solution for the nodes in the neighborhood of zero leakage. Joo and his colleagues [17] showed that there is a special solution for the transverse integrated diffusion equation when κ is exactly zero and used that solution as a fix to the zero buckling singularity. Joo also suggested switching to the Nodal Expansion Method (NEM) for the critical nodes and using ANM for non-critical nodes. He showed that both methods give similar results. Unfortunately, the first approach is only exact when κ is equal to zero, and the second approach is inconvenient regarding code complexity. The current ANM in NESTLE employs a simpler solution to this problem. The buckling term κ is shifted away from the critical region by perturbing the fission cross section in the critical nodes. The volume average neutron balance is preserved by adding a source term on the right hand side in the amount of the perturbed fission reaction rate. This method is fast and helpful if a node is not critical but becomes critical during outer iterations. Although this method helps the overall convergence of the code, the flux distribution in the critical node is not converged (Figure 2.4)

The effect of singularity is more drastic for the coarse mesh solution as seen in Figure 2.5. Since the Coarse Mesh Discontinuity Factors (CMDF) are calculated from a non-converged fine mesh flux distribution, the errors in the coarse mesh solution increases. Figure 2.5 also shows that these nodes would have large CMDF values which would cause robustness problems.

Therefore, the current solutions for the "zero buckling" singularity problem are not adequate for the consistent collapsing method.

A "buckling shifting" approach is employed to solve the zero buckling criticality problem. A Fourier analysis which is given in Appendix A revealed that under certain conditions the transverse leakage is a function of the transverse integrated flux for the 1-G transverse integrated diffusion equation. Following this analysis, the transverse leakage shape is approximated by adding a flux shape component to the normal quadratic expansion,

$$L^l(z) = D^l\left(B_{xy}^l\right)^2 \phi^l(z) + \Delta L^l(z) \tag{2-58}$$

where, ΔL^l is the residual quadratic polynomial and defined as,

$$\Delta L^l(z) = p_1^l f_1(z) + p_2^l f_2(z) \tag{2-59}$$

and satisfies

$$\int_{-\Delta z/2}^{\Delta z/2} \Delta \boldsymbol{L}^{\boldsymbol{l}}(\boldsymbol{z})\boldsymbol{dz} = 0 \tag{2-60}$$

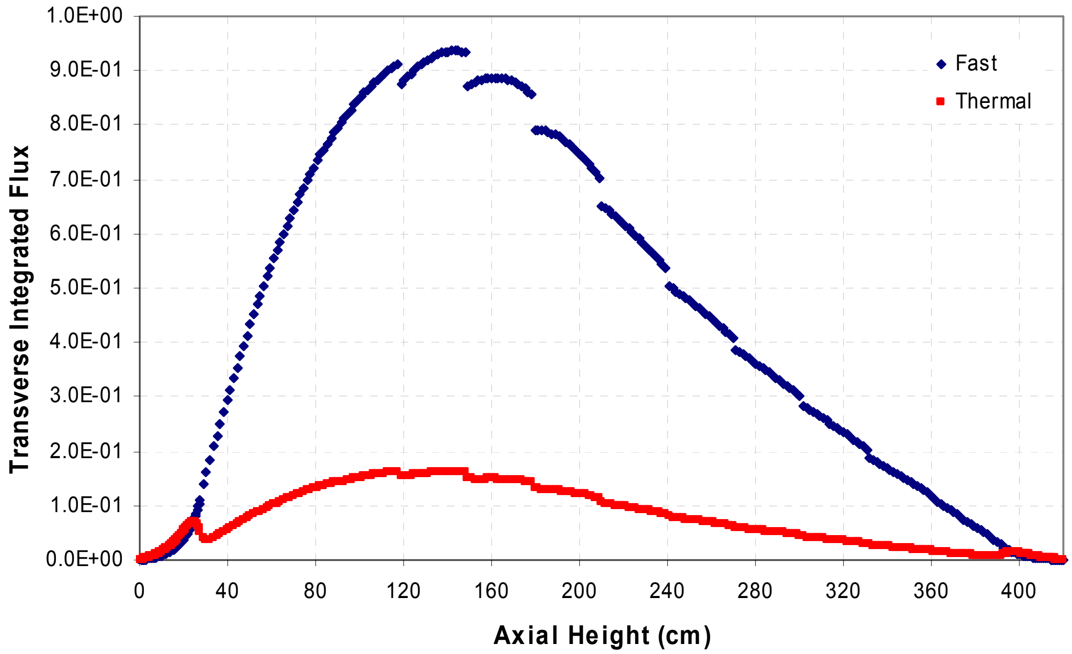

Figure 2.4 **Fine Mesh Solutions for a Critical Node with the Perturbation Fix-up**

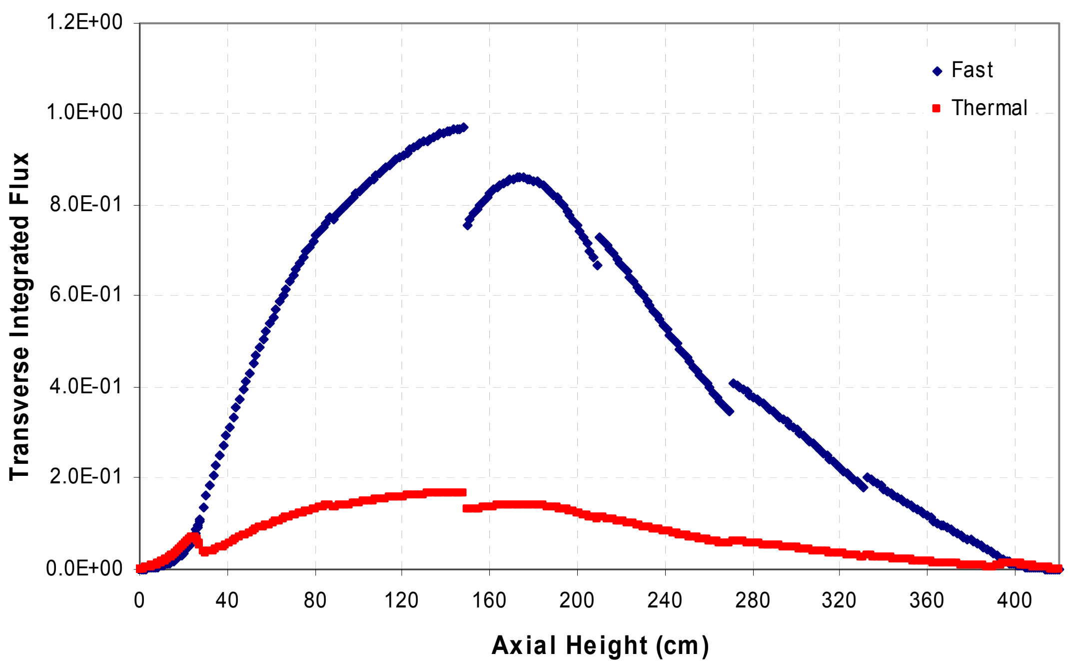

Figure 2.5 **Coarse Mesh Solutions for a Critical Node with the Perturbation Fix-up**

This formulation of the transverse leakage is useful since it helps to change the buckling term in the critical nodes by moving the flux component of the transverse leakage to the left hand side. Unfortunately, the Fourier analysis also shows that transverse leakage is dependent upon Fourier components of both energy groups for the 2-G transverse integrated diffusion equation. In order to define the transverse leakage in the form of Equation (2-58), one needs to decouple the 2-G equations into two 1-G equations. The system of equations for 2-G for node l can be written in matrix form as,

$$-\overline{\overline{\boldsymbol{D}^l}}\nabla^2\overrightarrow{\phi^l}(z)+\overline{\overline{\boldsymbol{A}^l}}\overrightarrow{\phi^l}(z)-\frac{1}{\boldsymbol{k}}\overline{\overline{\boldsymbol{M}^l}}\overrightarrow{\phi^l}(z)=-\overrightarrow{\boldsymbol{L}^l}(z) \tag{2-61}$$

where:

$$\overline{\overline{\boldsymbol{D}^l}}=\begin{bmatrix}\boldsymbol{D}_1^l & 0\\ 0 & \boldsymbol{D}_2^l\end{bmatrix},\ \overline{\overline{\boldsymbol{A}^l}}=\begin{bmatrix}\Sigma_{r1}^l & 0\\ -\Sigma_{s12}^l & \Sigma_{r2}^l\end{bmatrix},\ \overline{\overline{\boldsymbol{M}^l}}=\begin{bmatrix}\nu\Sigma_{f1}^l & \nu\Sigma_{f2}^l\\ 0 & 0\end{bmatrix},\ \overrightarrow{\phi^l}(z)=\begin{bmatrix}\phi_1^l(z)\\ \phi_2^l(z)\end{bmatrix},$$

$$\overrightarrow{\boldsymbol{L}^l}(z)=\begin{bmatrix}\boldsymbol{L}_1^l(z)\\ \boldsymbol{L}_2^l(z)\end{bmatrix}$$

Operating upon Equation (2-61) by $\left(\overline{\overline{D^l}}\right)^{-1}$ produces:

$$-\nabla\overrightarrow{\phi^l}(z)+\overline{\overline{\boldsymbol{B}^l}}\overrightarrow{\phi^l}(z)=-\left(\overline{\overline{\boldsymbol{D}^l}}\right)^{-1}\overrightarrow{\boldsymbol{L}^l}(z) \tag{2-62}$$

where

$$\overline{\overline{B^l}}\overset{\Delta}{=}\left(\overline{\overline{D^l}}\right)^{-1}\left[\overline{\overline{A^l}}-\frac{1}{k}\overline{\overline{M^l}}\right] \tag{2-63}$$

Now consider the solution of the following eigenvalue problem,

$$\overline{\overline{\boldsymbol{B}^l}}\,\overrightarrow{\Psi_j^l}=\lambda_j^l\overrightarrow{\Psi_j^l}\quad \textit{for } j=1,2 \tag{2-64}$$

and define the matrix $\overline{\overline{\boldsymbol{R}^l}}$ as $\overline{\overline{\boldsymbol{R}^l}}=\begin{bmatrix}\overrightarrow{\Psi_1^l} & \overrightarrow{\Psi_2^l}\end{bmatrix}$. We can then express the flux in terms of a new function, $\overrightarrow{\Phi^l}(z)$ as follows:

$$\overrightarrow{\boldsymbol{\phi}^{\boldsymbol{l}}}(\boldsymbol{z}) = \overline{\overline{\boldsymbol{R}^{\boldsymbol{l}}}}\,\overrightarrow{\Phi^{\boldsymbol{l}}}(\boldsymbol{z}) \tag{2-65}$$

Substituting Equation (2-65) into Equation (2-62) and multiplying through by $\left(\overline{\overline{\boldsymbol{R}^{\boldsymbol{l}}}}\right)^{-1}$ produces:

$$-\nabla^2\overrightarrow{\Phi^{\boldsymbol{l}}}(\boldsymbol{z}) + \overline{\overline{\lambda^{\boldsymbol{l}}}}\,\overrightarrow{\Phi^{\boldsymbol{l}}}(\boldsymbol{z}) = -\overrightarrow{\Gamma^{\boldsymbol{l}}}(\boldsymbol{z}) \tag{2-66}$$

where

$$\overrightarrow{\Gamma^{\boldsymbol{l}}}(\boldsymbol{z}) \stackrel{\Delta}{=} \left(\overline{\overline{\boldsymbol{R}^{\boldsymbol{l}}}}\right)^{-1}\left[\left(\overline{\overline{\boldsymbol{D}^{\boldsymbol{l}}}}\right)^{-1}\overrightarrow{\boldsymbol{L}^{\boldsymbol{l}}}(\boldsymbol{z})\right] \tag{2-67}$$

and $\overline{\overline{\lambda^l}}$ denotes the diagonal matrix whose diagonal elements are the eigenvalues of Equation (2-64). Equation (2-66) can be expressed as two 1-G equations, since the energy coupling has been removed:

$$-\nabla^2\Phi_j^l(z) + \lambda_j^l\Phi_j^l(z) = -\Gamma_j^l(z) \qquad j = 1,2 \tag{2-68}$$

where

$$\lambda_j^l = \begin{cases} \boldsymbol{\kappa} \text{ for } \boldsymbol{j} = 1 \\ \boldsymbol{\mu} \text{ for } \boldsymbol{j} = 2 \end{cases} \tag{2-69}$$

Equation (2-68) has the same form as the 1-G diffusion equation. However, the previous manner of treating the transverse leakage requires that the modified transverse leakage $\Gamma_j^l(z)$ be energy group decoupled with regard to the buckling component appearing in Equation (2-58). To determine whether this is true, we substitute Equation (2-58) (now with energy group dependence) into Equation (2-67) to obtain,

$$\overrightarrow{\Gamma^l}(z) = \left(\overline{\overline{R^l}}\right)^{-1}\left(\overline{\overline{D^l}}\right)^{-1}\left[\overline{\overline{D^l}}\,\overline{\overline{B^{l2}}}\,\overrightarrow{\phi^l}(z) + \overrightarrow{\Delta L^l}(z)\right] \tag{2-70}$$

Now $\overline{\overline{D^l}}$ and $\overline{\overline{\boldsymbol{B}^{l^2}}}$ are diagonal matrices, so the order of matrix multiplication does not matter, which allows Equation (2-70) to be written,

$$\overrightarrow{\Gamma^l}(z) = \overline{\overline{B^{l^2}}}\left(\overline{\overline{R^l}}\right)^{-1}\overrightarrow{\phi^l}(z) + \left(\overline{\overline{D^l}}\right)^{-1}\left(\overline{\overline{R^l}}\right)^{-1}\overrightarrow{\Delta L^l}(z) \tag{2-71}$$

Using Equation (2-65) in Equation (2-71) produces:

$$\overrightarrow{\Gamma^l}(z) = \overline{\overline{B^{l^2}}}\,\overline{\Phi^l}(z) + \overrightarrow{\Delta\Gamma^l}(z) \tag{2-72}$$

where the modified residual quadratic polynomial is defined as

$$\overrightarrow{\Delta\Gamma^{\boldsymbol{l}}}(\boldsymbol{z}) = \left(\overline{\overline{\boldsymbol{D^l}}}\right)^{-1}\left(\overline{\overline{\boldsymbol{R^l}}}\right)^{-1}\overrightarrow{\Delta \boldsymbol{L^l}}(\boldsymbol{z}) \tag{2-73}$$

Unfortunately, if the magnitude of elements of $\overline{\overline{\boldsymbol{B}^{l^2}}}$ ($\boldsymbol{B}_j^{l^2}$) are large, this algorithm can produce distorted intra nodal flux shapes. There are two reasons for this behavior in the flux shape: First, a large value of $\boldsymbol{B}_j^{l^2}$ means larger contribution of the flux to the transverse leakages and a quadratic correction function $\overrightarrow{\Delta\Gamma^{\boldsymbol{l}}}(\boldsymbol{z})$ cannot represent the higher order terms in the Fourier expansion accurately. Second, if the hyperbolic component of the intra-nodal flux dominates the flux shape a quadratic function again fails to represent the residuals. Therefore a “modified buckling shifting” is employed to prevent the singularity. First two additional variables are introduced to Equation (2-72).

$$\Gamma_j^{\boldsymbol{l}}(\boldsymbol{z}) = \widetilde{\Gamma}_j^{\boldsymbol{l}} + \boldsymbol{\theta}_j^{\boldsymbol{l}}\boldsymbol{B}_j^{\boldsymbol{l}^2}\Phi_j^{\boldsymbol{l}}(\boldsymbol{z}) + \Delta\Gamma_j^{\boldsymbol{l}}(\boldsymbol{z}) \text{ for } j=1,2 \tag{2-74}$$

where $\Delta\Gamma_j^{\boldsymbol{l}}(\boldsymbol{z})$ can be explicitly written as

$$\Delta\Gamma_j^l(z) = b_{j1}^l f_1(z) + b_{j2}^l f_2(z) \tag{2-75}$$

and f_1 and f_2 denote the normal NEM polynomial functions. The singularity of the solution matrix can be avoided by selecting a θ_1^l value in Equation (2-74) such that for the new buckling term,

$$\tilde{\kappa}^l = \sqrt{\left(\kappa^l\right)^2 - \theta_1\left(B_1^l\right)^2} \tag{2-76}$$

Note that $\theta_2^l = 0$ since the singularity originates from the κ^l and there is no need to shift the second root μ which introduces the hyperbolic components to the transverse leakage. The coefficients of $\Delta\Gamma_j^l(z)$ can be calculated by inserting Equation (2-72) into Equation (2-67) where $\overrightarrow{L^l}(z)$ is calculated from the quadratic transverse leakage approximation. $\tilde{\Gamma}_j^l$ is obtained by preserving node average transverse leakages as follows,

$$\tilde{\Gamma}_1^l = \frac{e^l}{D_1^l}\overline{L}_1^l - \frac{s^l e^l}{D_2^l}\overline{L}_2^l - \theta_1^l B_1^{l^2}\left(e^l\hat{\phi}_1^l - s^l e\hat{\phi}_2^l\right) \tag{2-77}$$

and

$$\tilde{\Gamma}_2^l = -\frac{e^l}{D_1^l}\overline{L}_1^l + \frac{r^l e^l}{D_2^l}\overline{L}_2^l \tag{2-78}$$

where $e^l = 1/\left(r^l - s^l\right)$. The remaining coefficients b_{j1}^l and b_{j2}^l can be calculated by demanding $\Gamma_j^l(z)$ to preserve $\overrightarrow{L^l}(z)$ at the node boundaries. However, these constraints require that the modified surface flux $\Phi_1^l(\pm\Delta z/2)$ to be known in Equation (2-74). Since the surface fluxes are not known prior to the ANM solution either FDM estimates or the previous iteration values of the surface fluxes can be used. On the other hand, if the derivatives of the transverse leakages at the node boundaries are used as constraints, the required derivative of the modified flux can be calculated from ANM corrected FDM surface currents. The latter is used since it provides more accurate constraints. Evaluating the derivative of Equation (2-67) at the node boundaries the remaining coefficients are calculates from,

$$\begin{bmatrix} \frac{1}{\Delta z^l} & -\frac{3}{\Delta z^l} \\ \frac{1}{\Delta z^l} & \frac{3}{\Delta z^l} \end{bmatrix} \begin{bmatrix} b_{11}^l \\ b_{21}^l \end{bmatrix} = \begin{bmatrix} \frac{e^l}{D_1^l}\frac{dL_1^l}{dz}\Big|_{-\Delta z^l/2} - \frac{s^l e^l}{D_2^l}\frac{dL_2^l}{dz}\Big|_{-\Delta z^l/2} - \theta_1^l B_1^{l^2}\left(\frac{e^l}{D_1^l}J_1^l\Big|_{-\Delta z/2} - \frac{s^l e^l}{D_2^l}J_2^l\Big|_{-\Delta z^l/2}\right) \\ \frac{e^l}{D_1^l}\frac{dL_1^l}{dz}\Big|_{+\Delta z^l/2} - \frac{s^l e^l}{D_2^l}\frac{dL_2^l}{dz}\Big|_{+\Delta z^l/2} - \theta_1^l B_1^{l^2}\left(\frac{e^l}{D_1^l}J_1^l\Big|_{+\Delta z/2} - \frac{s^l e^l}{D_2^l}J_2^l\Big|_{+\Delta z^l/2}\right) \end{bmatrix} \quad (2\text{-}79)$$

and

$$\begin{bmatrix} \frac{1}{\Delta z^l} & -\frac{3}{\Delta z^l} \\ \frac{1}{\Delta z^l} & \frac{3}{\Delta z^l} \end{bmatrix} \begin{bmatrix} b_{12}^l \\ b_{22}^l \end{bmatrix} = \begin{bmatrix} -\frac{e^l}{D_1^l}\frac{dL_1^l}{dz}\Big|_{-\Delta z^l/2} + \frac{r^l e^l}{D_2^l}\frac{dL_2^l}{dz}\Big|_{-\Delta z^l/2} \\ -\frac{e^l}{D_1^l}\frac{dL_1^l}{dz}\Big|_{+\Delta z^l/2} + \frac{r^l e^l}{D_2^l}\frac{dL_2^l}{dz}\Big|_{+\Delta z^l/2} \end{bmatrix} \quad (2\text{-}80)$$

2.2.5.2 Fundamental Mode Singularity

This second type of singularity is similar to the “zero buckling” singularity; however, it originates not only from neutronics properties but also from the grid layout that is used to solve the nodal balance equation. Since this type of singularity is related to the node size like the $\tilde{\boldsymbol{D}}$ factors (Equation 2.31), it can be mistaken easily with the adverse effect of large $\tilde{\boldsymbol{D}}$ values on the convergence for the solution for large node sizes [38].

As shown in Figure 2.6, the solution of the “one-node problem” can produce an unphysical flux behavior. A large error in the flux shape is expected in the coarse nodes whose associated fine nodes exhibit strong within node spatial flux dependence, such as fuel nodes adjacent to reflectors or control rods. However, the fine mesh flux shape in Figure 2.7 is smooth and should be easily represented by the coarse mesh flux. The bizarre behavior of the flux at some coarse nodes can be understood when the ANM solution of the coarse mesh flux is investigated.

The ANM solution of the transverse integrated diffusion equation using the quadratic transverse leakage approximation for node l in the z direction is given in Equation (2-53)

$$\phi_{gz}^{l}(z) = a_{g1}^{l} sn(\kappa^{l} z) + a_{g2}^{l} cn(\kappa^{l} z) + a_{g3}^{l} sn(\mu^{l} z) + a_{g4}^{l} cn(\mu^{l} z) + \sum_{i=0}^{2} c_{gi}^{l} f_{i}(z) \qquad (2\text{-}53)$$

where κ and μ are eigenvalues (roots of the buckling term) of the coefficient matrix of the two-group diffusion equations. From the "one-node" problem explained in Section 2.2.4, we recall that the even coefficients of Equation (2-53) are calculated from the node average fluxes and the odd coefficients of the flux distribution are obtained using

$$\begin{bmatrix} -\hat{\boldsymbol{D}}_1 \boldsymbol{r}\boldsymbol{\kappa} \cos(\boldsymbol{\kappa}\frac{\Delta z}{2}) & -\hat{\boldsymbol{D}}_1 \boldsymbol{s}\boldsymbol{\mu} \cosh(\boldsymbol{\mu}\frac{\Delta z}{2}) \\ -\hat{\boldsymbol{D}}_2 \boldsymbol{\kappa} \cos(\boldsymbol{\kappa}\frac{\Delta z}{2}) & -\hat{\boldsymbol{D}}_2 \boldsymbol{\mu} \cosh(\boldsymbol{\mu}\frac{\Delta z}{2}) \end{bmatrix} \begin{bmatrix} \boldsymbol{a}_{21} \\ \boldsymbol{a}_{23} \end{bmatrix} = \begin{bmatrix} \hat{\boldsymbol{J}}_1^- \\ \hat{\boldsymbol{J}}_2^- \end{bmatrix} + \begin{bmatrix} \boldsymbol{C}_1 \\ \boldsymbol{C}_2 \end{bmatrix} \qquad \textbf{(2-81)}$$

where $\hat{\boldsymbol{J}}_1^-, \hat{\boldsymbol{J}}_2^-$ represent surface averaged currents and C_1 ,C_2 are functions of transverse leakage coefficients. When the mesh size is increased during the collapse, the cosine argument can take on values close to $\frac{\pi}{2}$ for some nodes. The condition number of the coefficient matrix increases as the cosine terms in Equation (2-81) go to zero. The larger condition number of the coefficient matrix amplifies the errors in the coarse mesh flux solution due to the errors in the transverse leakage coefficients.

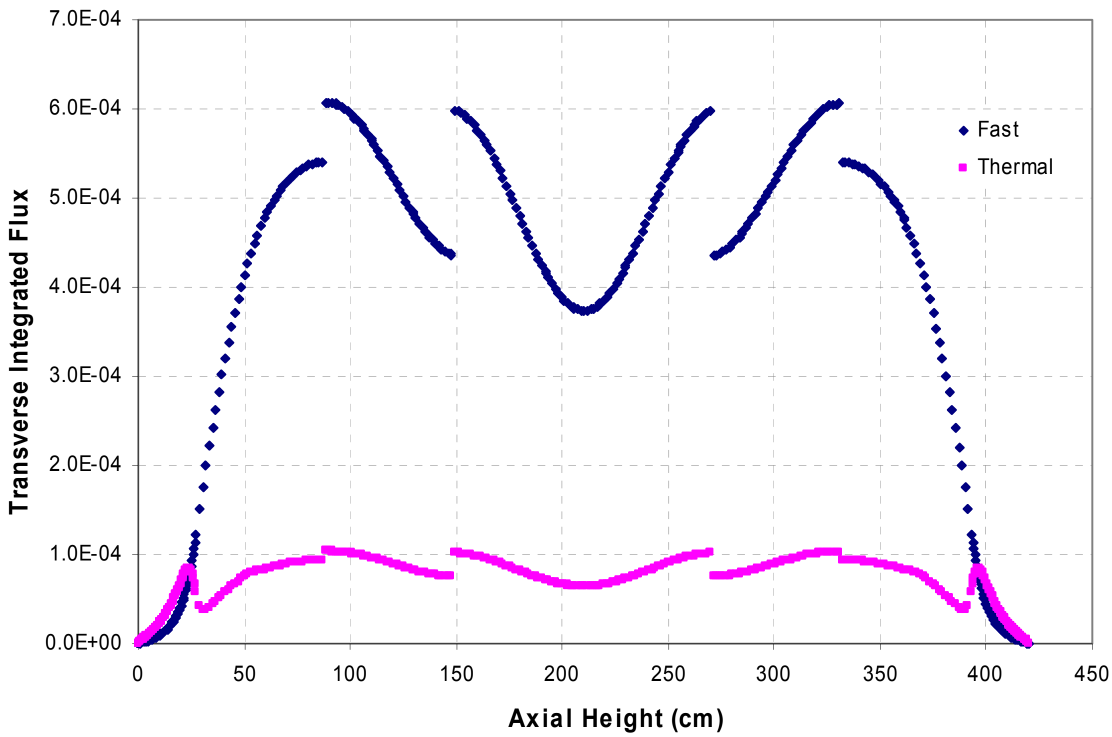

Figure 2.6 Coarse Mesh ANM Solution for Axially Heterogeneous Core

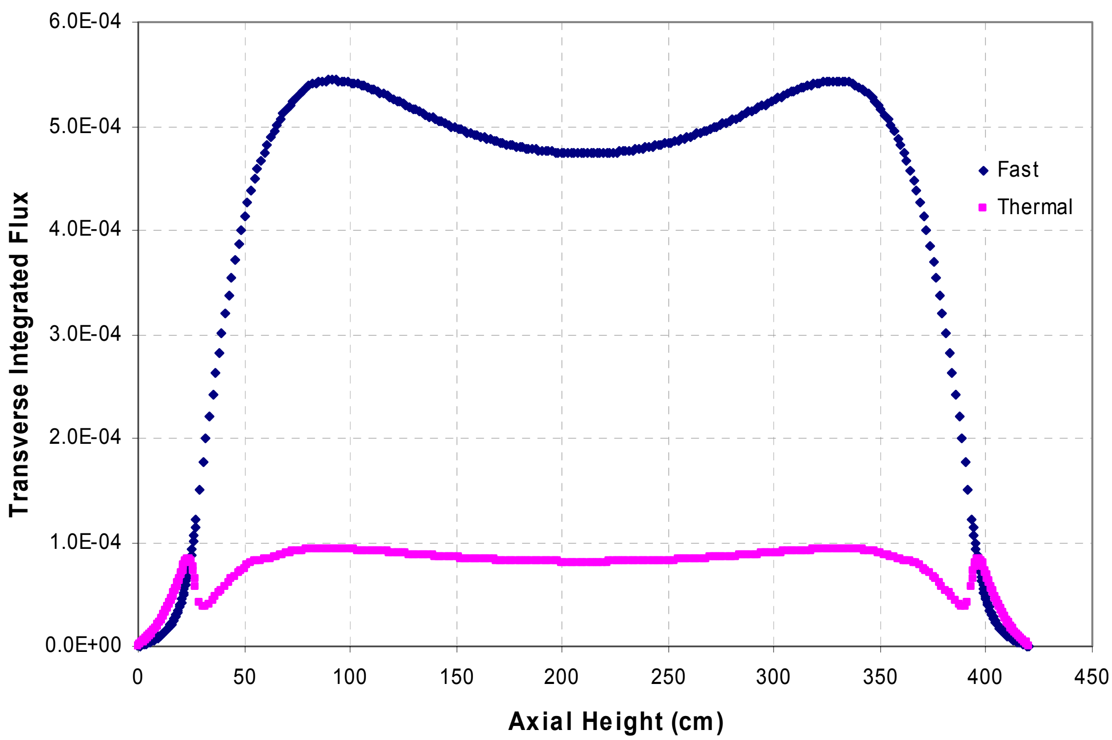

Figure 2.7 Fine Mesh Current ANM Solution for Axially Heterogonous Core

The ANM solution in these nodes can be improved by minimizing the transverse leakage errors or decreasing the buckling term. Various transverse leakage approximations are tested in Section 3.2 to improve the coarse mesh intra-nodal flux shape. Although some improvement is observed with the single precision accuracy, these approximations failed to resolve the problem. A practical approach is developed to prevent the singularity in the coefficient matrix.

In this new approach, the coordinate system of each node is shifted by an ε value as shown in Figure 2.8. Recall the coordinate system for each node in the current ANM is defined as $\left[-\frac{\Delta x}{2},\frac{\Delta x}{2}\right],\left[-\frac{\Delta y}{2},\frac{\Delta y}{2}\right],\left[-\frac{\Delta z}{2},\frac{\Delta z}{2}\right]$ to simplify the implementation. The selection of the coordinate system for ANM is not expected to affect the solution. However, shifting the coordinate system by a small negative ε value as shown in Figure 2.8 can reduce the condition number of the coefficient matrix by reducing the magnitude of the hyperbolic components and increasing the magnitude of the cosine terms.

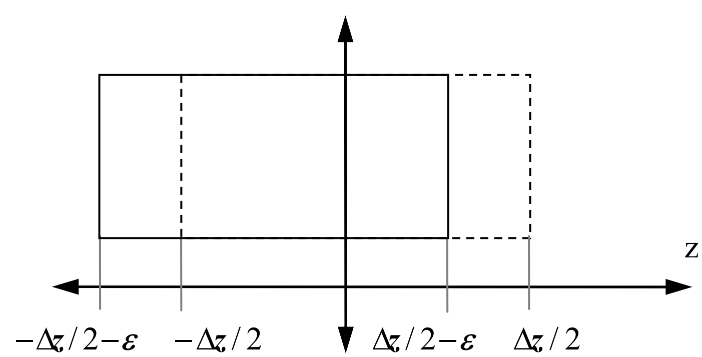

Figure 2.8 Coordinate Transformation for the One-Node Problem

The new coefficient matrix for the new shifted coordinate system becomes,

$$
\begin{bmatrix}
-D_1^l r^l \kappa^l \cos\left(\kappa^l \frac{\Delta z^l}{2} - \kappa^l \varepsilon\right) & -D_1^l s^l \mu^l \cosh\left(\mu^l \frac{\Delta z^l}{2} - \mu^l \varepsilon\right) \\
-D_2^l \kappa^l \cos\left(\kappa^l \frac{\Delta z^l}{2} - \kappa^l \varepsilon\right) & -D_2^l \mu^l \cosh\left(\mu^l \frac{\Delta z^l}{2} - \mu^l \varepsilon\right)
\end{bmatrix} =
$$

$$
\begin{bmatrix}
-D_1^l r^l \kappa^l \left(\cos\left(\kappa^l \frac{\Delta z^l}{2}\right)\cos(\kappa^l \varepsilon) + \sin\left(\kappa^l \frac{\Delta z^l}{2}\right)\sin(\kappa^l \varepsilon)\right) & -D_1^l s^l \mu^l \left(\cosh\left(\mu^l \frac{\Delta z^l}{2}\right)\cosh(\mu^l \varepsilon) - \sinh\left(\mu^l \frac{\Delta z^l}{2}\right)\sinh(\mu^l \varepsilon)\right) \\
-D_2^l \kappa^l \left(\cos\left(\kappa^l \frac{\Delta z^l}{2}\right)\cos(\kappa^l \varepsilon) + \sin\left(\kappa^l \frac{\Delta z^l}{2}\right)\sin(\kappa^l \varepsilon)\right) & -D_2^l \mu^l \left(\cosh\left(\mu^l \frac{\Delta z^l}{2}\right)\cosh(\mu^l \varepsilon) - \sinh\left(\mu^l \frac{\Delta z^l}{2}\right)\sinh(\mu^l \varepsilon)\right)
\end{bmatrix} \tag{2-82}
$$

Since $\sin\left(\kappa^l \frac{\Delta z^l}{2}\right)\sin(\kappa^l \varepsilon) \neq 0$ and $\cosh\left(\mu^l \frac{\Delta z^l}{2}\right)\cosh(\mu^l \varepsilon) \approx \sinh\left(\mu^l \frac{\Delta z^l}{2}\right)\sinh(\mu^l \varepsilon)$ for large values of Δz^l, the two factors causing the high condition number of the coefficient matrix, small cosine values and large hyperbolic values, are eliminated.

2.3 Error Analysis

The strength of the Super-Nodal method comes from its capability of representing the fine mesh reference solution with better accuracy than the original nodal method using the same mesh size. The Super-Nodal method achieves this accuracy with DFs and the homogenized cross section sets. As the consistent collapsing of cross sections assures preservation of the fine mesh reaction rates, DFs correct for all homogenization errors. In the absence of any singularities mentioned in the previous section, the coarse mesh solution reproduces the fine mesh solution for the state that collapsing is performed at. However, as the reactor deviates from the state that the collapsing is performed at, DFs cannot correct for the coarse mesh solution errors at the new state and the coarse mesh solution deviates from the fine mesh solution. The main contributors of the coarse mesh solution error are the following,

A) Quadratic Transverse Leakage Approximation

Due to the polynomial form of the transverse leakage, the error in the transverse leakage shape is expected to increase as the mesh size increases. However, the largest contributor to the transverse leakage error comes from the non-physical constraints on the transverse leakage shape which becomes more prominent at the coarse mesh nodalizations.

B) Thermal-Hydraulic (T-H) Feedback

The thermal-hydraulic feedback calculations are performed using the FDM approach; therefore, it is no surprise that reactor T-H parameters, such as coolant density, fuel temperature and coolant temperature, would have increasing errors with the increasing mesh sizes. Moreover, during transient calculations, errors from the previous time step (depending on the time step size) can contribute to cause larger errors in the thermal-hydraulic feedback parameters. Although errors in the coarse mesh T-H parameters can be minimized by performing the T-H calculations at the fine mesh level employing flux form factors, as the form factors deviate from their correct values the errors in the T-H feedback parameters also increase.

C) Control Rod Movement

Calculation of homogenized cross sections and CMDFs depend on the fine mesh solution. If the spatial distribution of the flux changes, the homogenized cross sections and CMDF value will change. Hence for nodes which control rod assemblies pass through during the transient, they present a real challenge to the Super-Nodal method. The problem is how to calculate the rodded cross sections for a node if that node was not rodded when the collapsing is performed. The same discussion is valid for the calculation of the unrodded cross sections if a node is rodded during collapsing and becomes unrodded afterward. One approach is to use the same flux volume weighting for both rodded and unrodded cross section generation regardless of if the node is rodded or unrodded during collapsing. The rodded and unrodded CMDFs then can be calculated by setting them equal to each other. The second approach is to perform two collapsing calculations, one for the node rodded and the other for the node unrodded, and calculate cross sections and DFs for these two cases. Although the latter is more consistent with the assembly calculations, it does not preserve the reaction rates even if the node is totally rodded or unrodded. This follows since the axial flux distribution within a node can be a strong function of the axial insertion position of the control rod, not just whether the node is rodded or unrodded. The problem with control rods becomes even more complicated if the node is partially rodded. The conventional treatment is volume weighting of the rodded and unrodded cross sections to calculate the cross sections. However, this approach creates the so called "rod cusping" effect due to under and over weighting of the unrodded and rodded cross sections, respectively. The effect of rod cusping is more pronounced as the node size increases. This problem is treated in NESTLE 6.1 by splitting a partially rodded node into a rodded and unrodded node and solving a four-node problem based on nodal constraints [37]. Although this approach can help during the transient for the coarse mesh nodalization, it does not provide a solution to calculation of the homogenization parameters if a node is partially rodded during collapsing.

D) Error in the Fine Mesh Solution

NESTLE employs a non-linear iterative nodal update technique to calculate correction factors ($\tilde{\boldsymbol{D}}$) to the diffusion coupling coefficients. Due to the nonlinear nature of this technique, it is possible to have non converged solutions for some nodes in the core if the stopping criteria are not set tight enough, or if the ANM solution has singularities as mentioned in the previous section. In any case, if the reference solution is not converged, the CMDFs and homogenized cross sections would have errors in them. Particularly, the errors in the DFs lead to instabilities later in the coarse mesh solution. The effect of such errors in the reference solution as seen in Figure 2.4 are amplified in the coarse mesh solution as seen in Figure 2.5.

A detailed error analysis is not carried out in this research. A simple approach based on the relative residual is proposed as a starting point for future work. The relative residual approach is now described.

Recall the FDM equation for the diffusion equation in the matrix form,

$$\overline{\overline{A}}\vec{\phi} = \frac{1}{k}\overline{\overline{F}}\vec{\phi} \tag{2-53}$$

Since flux vector $\vec{\phi}$ is calculated iteratively, the residual vector $\vec{r}$ which is defined as,

$$\vec{r} = \overline{\overline{A}}\vec{\phi} - \frac{1}{k}\overline{\overline{F}}\vec{\phi} \tag{2-53}$$

is not a zero vector if the solution is not converged. Therefore, a scaled norm of the residual vector can provide information about the error in the solution. The same idea can be used to measure the coarse mesh solution error. If the coarse mesh solution is mapped back to the fine mesh level using flux form factors and if the fine mesh $\overline{\overline{A}}$ and $\overline{\overline{F}}$ matrices can be calculated, the fission source scaled L_2 norm of the residual $\frac{\left\|\vec{r}\right\|}{\left\|\overline{\overline{F}}\vec{\phi}\right\|}$ can be evaluated and give us an idea about how much the coarse mesh solution violates the neutron balance equation at the fine mesh level; hence, provide an estimate of the error in the coarse mesh solution. However, this formulation requires fine mesh cross-sections and fine mesh $\widetilde{D}$ values to be known to construct the $\overline{\overline{A}}$ and $\overline{\overline{F}}$ matrices. The fine mesh cross-sections can be calculated employing fine mesh T-H calculation at the coarse mesh level; however, calculation of fine mesh $\widetilde{D}$ values is not trivial. The most recent fine mesh $\widetilde{D}$ values can be used for the error estimate, remembering that the relative residual would also be including a contribution from this assumption that may increase or decrease the magnitude of the L_2 norm. This approach has been tested for different transients and results are presented in Chapter 4.

3. Alternative Approaches

3.1 Diffusion Coefficient Calculation

As discussed in Chapter 2 in detail, in order to represent a reactor core accurately at the coarse mesh level, homogenization parameters must be calculated employing the consistent collapsing (CC) technique. Preserving surface average currents during homogenization is one of the key points of the CC technique. The surface average currents and hence the leakages can be preserved if the diffusion coefficient is defined as

$$\hat{D}_{gu}^{N\pm} = \frac{\sum_{i \in S^{N\pm}} J_{gu}^{i\pm} A_u^i}{-\nabla \hat{\phi}_{gu}^{N\pm} \sum_{i \in S^{N\pm}} A_u^i} \tag{3-1}$$

where

u = x,y,z

i = fine-node surface index

N = coarse-node index

$S^{N\pm}$ = set of fine-node surfaces i making up coarse-node surface (+=left; -=right of coarse-node N)

$J_{gu}^{i\pm}$ = fine-node surface average current normal to surface i

A_u^i = fine-node surface area

$\hat{\phi}_g^{N\pm}$ = coarse-node surface average flux

$D_{gu}^{N\pm}$ = coarse-node diffusion coefficient.

The reason surface dependent diffusion coefficients are required versus using a node average dependant quantities which would preserve total node leakages, is because of the continuity of current condition on each surface. The G.E.T. avoids this problem by using some simple expression to determine the homogenized diffusion coefficient, such as via flux-volume weighting,

$$\hat{D}_g^N = \frac{\sum_i D_g^i \phi_g^i V^i}{\hat{\phi}_g^N \Delta \hat{V}^N} \quad g = 1,2 \;\; i \in N \tag{3-2}$$

Although Equation (3-2) is inaccurate, CMDFs correct for the errors in the resulting coarse-node surface average currents. As noted earlier, the ratio of the resulting CMDFs across a surface can be large, causing robustness problems. Also, the homogenous flux is used to project an estimate of the fine flux, which is used in several capacities as noted earlier. If the homogenous flux has a very unphysical shape, it is likely to deviate substantially as core conditions change from those at time of CC, invalidating the form factors used in the projection of the fine flux. Three alternative calculational methods for determining diffusion coefficient are developed. The common idea in these three methods is to adjust the diffusion coefficient in each direction such that the change in the CMDF value across a surface in each direction is reduced.

3.1.1 Approach 1

Approach 1 is to determine direction dependent diffusion coefficients so as to satisfy surface flux continuity across node interfaces. The effects of varying the values of fast and thermal group diffusion coefficients on node surface flux are shown in Figure 3.1. The sharp deep values of the surface fluxes are an indication of the singularity points discussed in the previous sections.

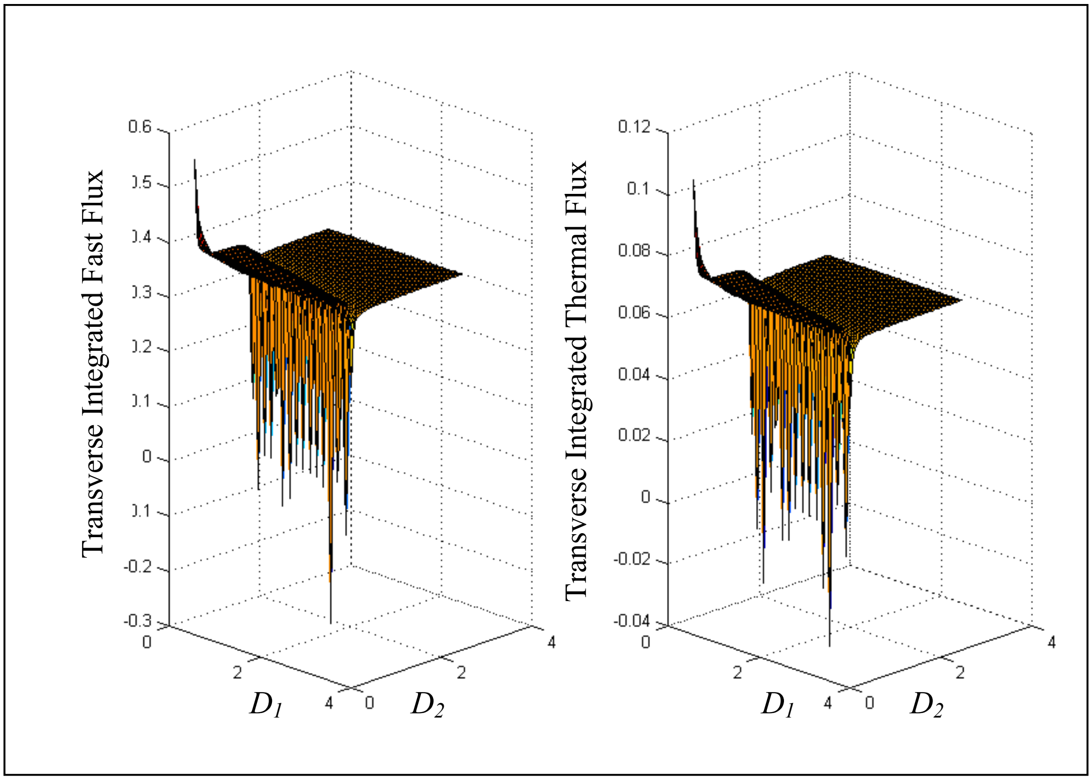

Figure 3.1 Change in Fast and Thermal Transverse Integrated Fluxes with Diffusion Coefficients

Determining the fast and thermal, direction dependent diffusion coefficients requires two additional equations to obtain a complete system of equations. These two additional equations are obtained by requiring the coarse-node surface average homogenous flux for each energy group on the left side to be equal to a specific value. Then the right side surface average flux can be calculated for the coarse-node, and serves as the left side boundary condition for the next node as shown in Figure 3.2. For the left most node, the surface average flux of the coarse node is determined from the fine-node solution. The Newton-Raphson method is employed to determine the coarse-mesh diffusion coefficients due to the non-linearity of the problem.

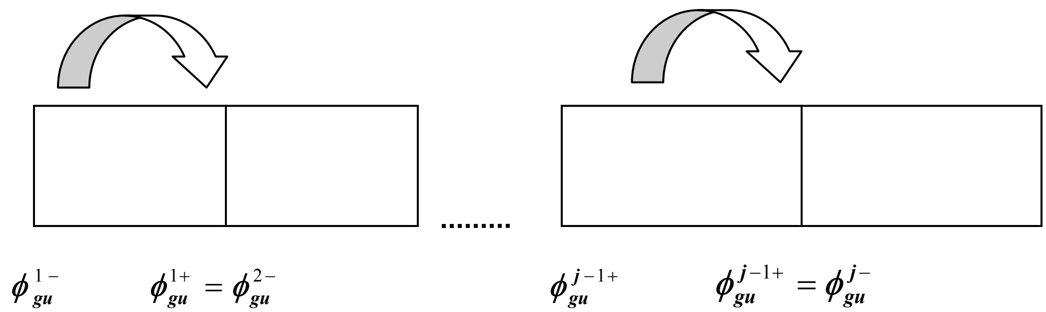

Figure 3.2 Calculation of D_g Using Approach 1

A fresh fuel loaded core is modeled to test this new approach and the core is axially collapsed from 18 nodes (30.48 cm fuel nodes) to 12 nodes (60.96 cm fuel nodes) by collapsing all nodes except the ones about the upper and lower fuel-reflector interfaces. Approach 1 proved to be promising when the axial flux shape with the direction dependent diffusion coefficients are compared to the axial flux shape obtained from the flux-volume weighted diffusion coefficients (see Figure 3.3 and Figure 3.4). The two large jumps which are located between node 5-6 and 7-8 interfaces are nearly eliminated as seen in Figure 3.4. As a measure of jumps in the flux shape, ratios of CMDF across these two surfaces are compared in Table 3-1. Why the ratios differs from *1.0,* hence small flux interface jumps still exist, is just an indication of degree of convergence of the Newton-Raphson method. The two different diffusion coefficients which are calculated by flux-volume weighting and using Approach 1 are also compared in Table 3-2 for each axial coarse node. The oscillatory behavior of the thermal diffusion coefficient is troubling since the total fueled region is homogenous.

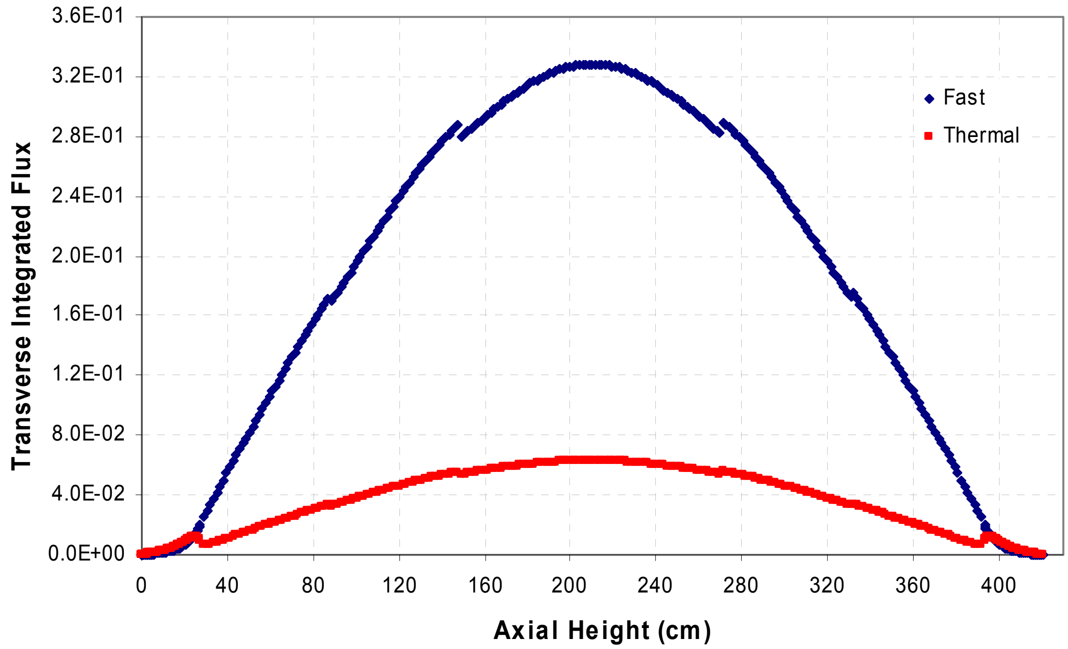

Figure 3.3 **Coarse Mesh Flux Shape Calculated Using Volume Averaged D_g**

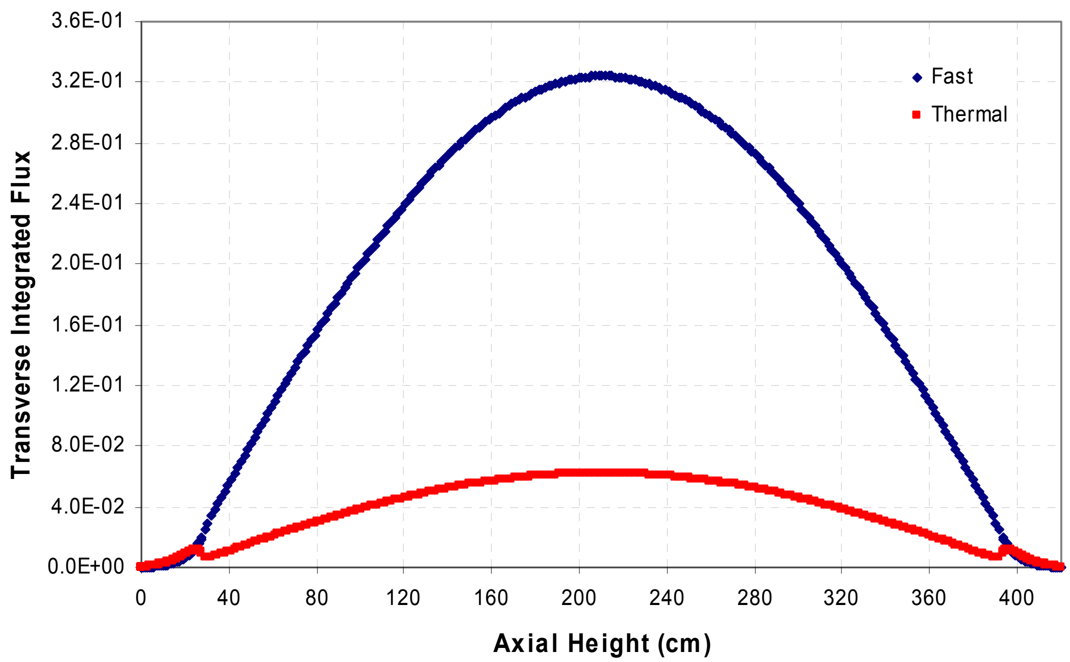

Figure 3.4 **Coarse Mesh Flux Shape Calculated Using Approach 1**

Table 3-1 Comparison of ADF Ratios for Approach 1

	Flux Volume Averaged		Approach 1	
Node Interface	Fast	Thermal	Fast	Thermal
5-6	0.97352	0.97448	1.00648	1.00727
7-8	1.02687	1.02589	0.993522	0.994371

Table 3-2 Comparison of Diffusion Coefficients Calculated From Flux-Volume Averaging and From Approach 1

	Flux Volume Averaged		Approach 1	
Axial Node Number	D_1	D_2	D_1	D_2
1	1.775354	0.2817671	1.788398	0.2594372
2	1.775354	0.2817671	1.764482	0.3052364
3	1.446565	0.3908812	1.456182	0.3399230
4	1.446565	0.3908812	1.440050	0.4513714
5	1.446565	0.3908812	1.483852	0.3426386
6	1.446565	0.3908812	1.483253	0.4644495
7	1.446565	0.3908812	1.476254	0.4856077
8	1.446565	0.3908812	1.487616	0.3292696
9	1.446565	0.3908812	1.435447	0.4689353
10	1.446565	0.3908812	1.459977	0.3271905
11	1.775354	0.2817672	1.751586	0.3145596
12	1.775354	0.2817671	1.811760	0.2519424

Unfortunately, after further research we determined that this approach can fail when the thermal-hydraulic feedback is treated or applied to sub-critical nodes. This occurs since a diffusion coefficient with a reasonable value cannot satisfy the targeted surface average flux value. Figure 3.5 shows the change in the thermal surface average flux value with D_2. Note that the targeted surface flux value is 2.081×10^{-3} and the maximum obtainable value by adjusting D_2 is 2.06×10^{-3} for this case (seen in Figure 3.6 which is a blowup of a portion of Figure 3.5).

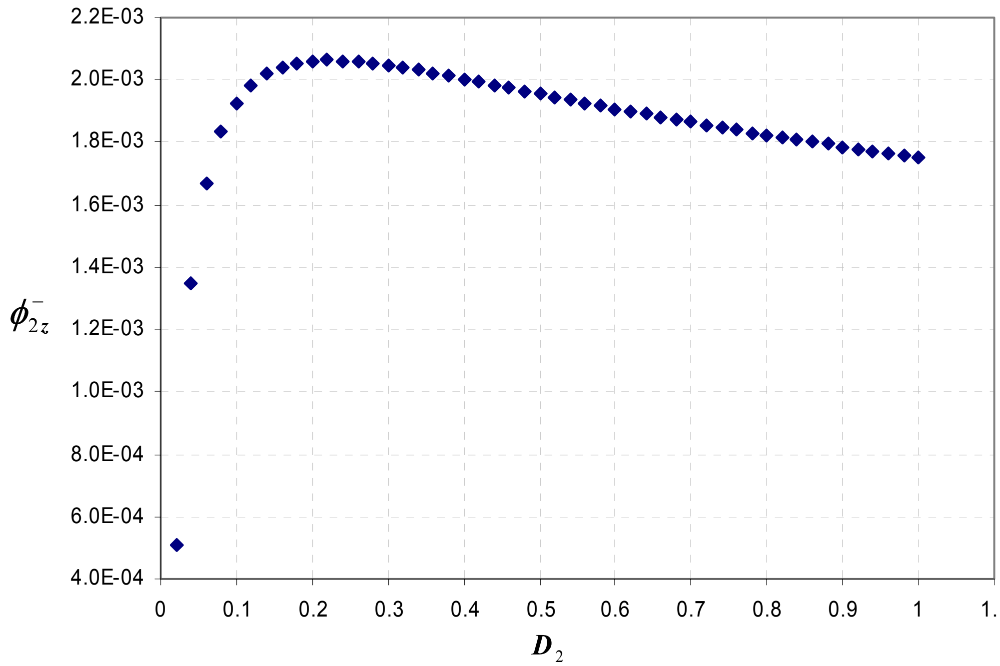

Figure 3.5 Change in Left Surface Thermal Flux with D_2

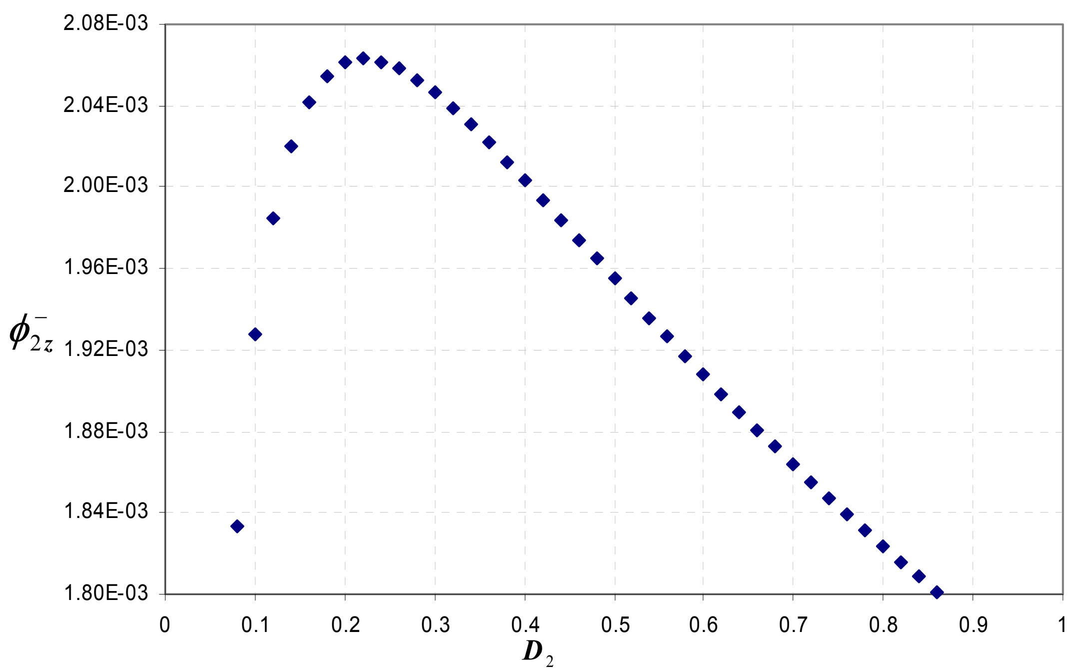

Figure 3.6 Change in Left Surface Thermal Flux with D_2 (peak region)

3.1.2 Approach 2

After determining that the diffusion coefficient is not sufficient to change the surface flux to the targeted value, the second approach was developed to introduce more degrees of freedom by using transverse leakage expansion coefficients. The selection is based on the fact that the transverse leakage expansion coefficients using NEM expansion functions are calculated based on an approximation, so as long as the node average transverse leakage is preserved the neutron balance is preserved, and there still is freedom in selecting the expansion coefficients. By treating the two expansion coefficients and the node average diffusion coefficient for each group as unknowns, this implies for two groups that the total number of unknowns increases to six. Four constraints are obtained by requiring the homogenous surface average fluxes to be equal to the heterogeneous surface average fluxes on both sides of a node. For the remaining two constraints, continuity of the derivative of the transverse leakage on the left surface of a node is demanded. Starting from the left most node, and knowing the derivative of the transverse leakage on the left surface from the fine mesh solution, the transverse leakage expansion coefficients are determined, allowing the derivative on the right surface to be calculated. The calculation is marched through the last node as in Approach 1. The constraints and equations are shown in Table 3-3.

Table 3-3 Unknowns and Constraints for Approach 2

Unknowns	Constraints
$D_g^l, b_{g1}^l, b_{g2}^l$	$\hat{\phi}_{gu}^{l+} = \phi_{gu}^{1+}$, $\hat{\phi}_{gu}^{l-} = \phi_{gu}^{1-}$, $\left.\frac{dL_{gu}^{l}}{du}\right\vert_{+} = \left.\frac{dL_{gu}^{l+1}}{du}\right\vert_{-}$

As a test case the fine mesh nodalization is used. This new approach is expected to return the original diffusion coefficients and the transverse leakage coefficients. Nevertheless, Approach 2 failed to converge due to error propagation. As the calculation marches through the nodes, the derivative of the transverse leakage deviates from the reference solution.

3.1.3 Approach 3

Since the first two approaches failed to provide a continuous coarse mesh flux across node boundaries, the third approach chooses to preserve node-wise integral versus point-wise properties. When the fine and coarse mesh fluxes are compared, the coarse mesh flux can appear tilted on one side relative to the fine mesh flux. Preserving the node average flux, equivalent to the zeroth moment of the flux, and surface average currents apparently cannot adequately constrain the coarse mesh flux shape. Another constraint on the overall flux shape can be added by conserving the first moment of the fine mesh flux. This constraint is used to determine the node-average diffusion coefficient, taking the place of preserving the left surface flux that was used in Approach 1.

In this new approach, the coordinate system of the coarse mesh flux is changed from $\left[\frac{-\Delta z}{2},\frac{\Delta z}{2}\right]$ to $[0,\Delta z]$ in order to prevent errors canceling out due to symmetry in the coordinate system. The modified coarse mesh coordinate system is used to calculate the first moment of the fine mesh inside the coarse mesh node boundaries. The coordinate transformation for the coarse and the fine meshes are shown in Figure 3.7,

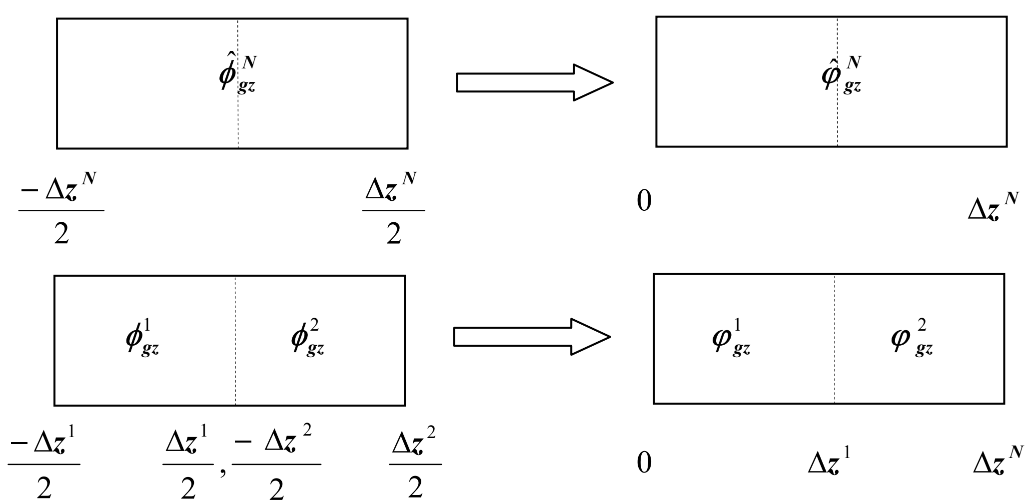

Figure 3.7 Coordinate Transformation for Approach Three

where, $\hat{\varphi}_g^N(z)$ and $\varphi_g^j(z)$ are the coarse and fine mesh flux shapes in the new coordinate system, respectively. The constraint on the first moment is given by,

$$\int_0^{\Delta z^N} z\hat{\varphi}_g^N(z)dz = \sum_j \int_{\Delta z^{j-1}}^{\Delta z^j} z\varphi_g^j(z)dz \tag{3-3}$$

The error in the coarse mesh flux is defined as

$$e = \sum_j \int_{\Delta z^{j-1}}^{\Delta z^j} z\varphi_g^j(z)dz - \int_0^{\Delta z^N} z\hat{\varphi}_g^N(z)dz \tag{3-4}$$

and minimized using the Newton-Raphson algorithm.

This new approach is tested using the same test core as used for Approach 1. Approach 3 produces almost identical result as Approach 1. Since Approach 1 failed when thermal-hydraulic feedback was treated, Approach 3 is tested with thermal-hydraulic feedback. Figure 3.8 and Figure 3.9 show the transverse integrated flux shapes employing the coarse mesh diffusion coefficients calculated from flux volume averaging and from the new approach, respectively. The new approach reduces the ratios of CMDFs for the node surface between nodes 5 and 6, as shown in Table 3-4.

Table 3-4 Comparison of ADF Ratios for the Surface Between Nodes 5 and 6

Flux Volume Averaged		**Approach 3**	
Fast	Thermal	Fast	Thermal
0.97643	0.95339	0.99044	0.98608

Although the new algorithm improves the coarse mesh flux shape, it never converges for certain nodes. In this example node 6, which is located between 149.32 cm and 210.28 cm in axial height, never converged and all of the improvement in the CMDF ratios comes from the converged solution of node 5 as indicated in Table 3-5.

Table 3-5 The First Moment Errors and Diffusion Coefficients for Node 5

	Flux Volume Averaged		**Approach 3**	
	Fast	**Thermal**	**Fast**	**Thermal**
Error (e)	-9.05712	-3.47182	2.4414e-3	7.9345e-4
Diffusion Coefficient	1.41540	0.38599	1.5598	0.5024

When the change in first moment error versus change in the two group diffusion coefficients are examined in Figure 3.10 to Figure 3.12 for node 5 and node 6, it is seen that the first moment error in node 6 is very insensitive for reasonable values of the diffusion coefficients. The neutronics properties of node 5 and node 6 are very close due to the fact that both nodes span the same fresh fuel region. The main difference in these two nodes is that node 6 is a low leakage node. Since the diffusion coefficient appears in the leakage term of the diffusion equation, the solution of the diffusion equation becomes less sensitive to the change in diffusion coefficient as the leakage decreases in the node.

All three approaches proved that diffusion coefficients can help to reduce CMDF ratios; however, the calculation of a new diffusion coefficient is time consuming and does not always guarantee better results. Therefore, none of these approaches was pursued further.

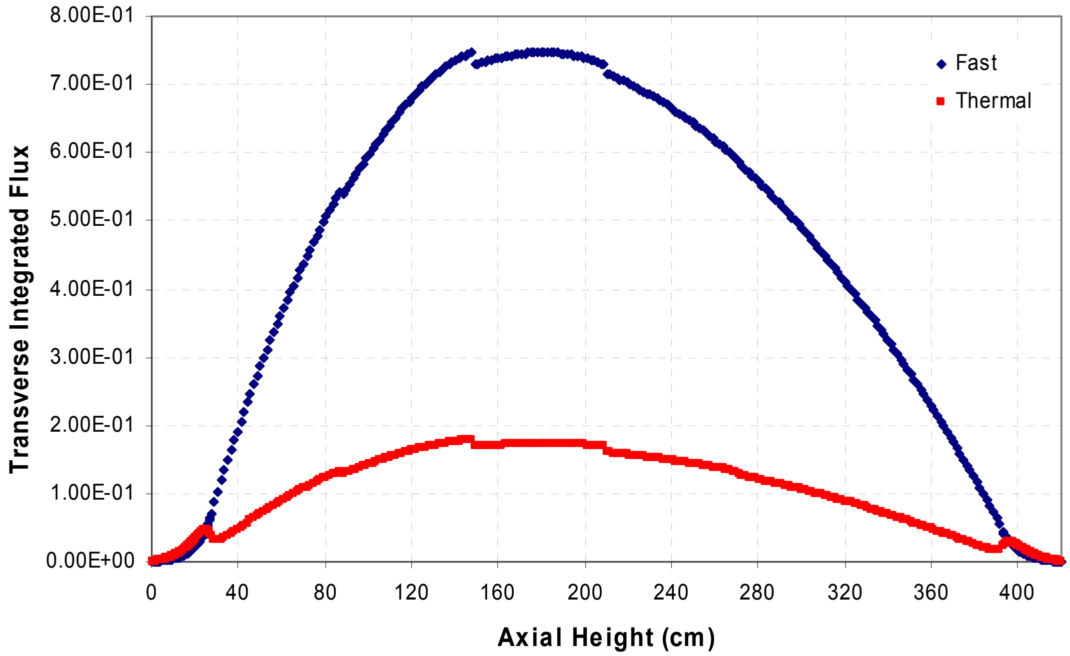

Figure 3.8 Coarse Mesh Flux Shape Calculated Using Volume Averaged D_g

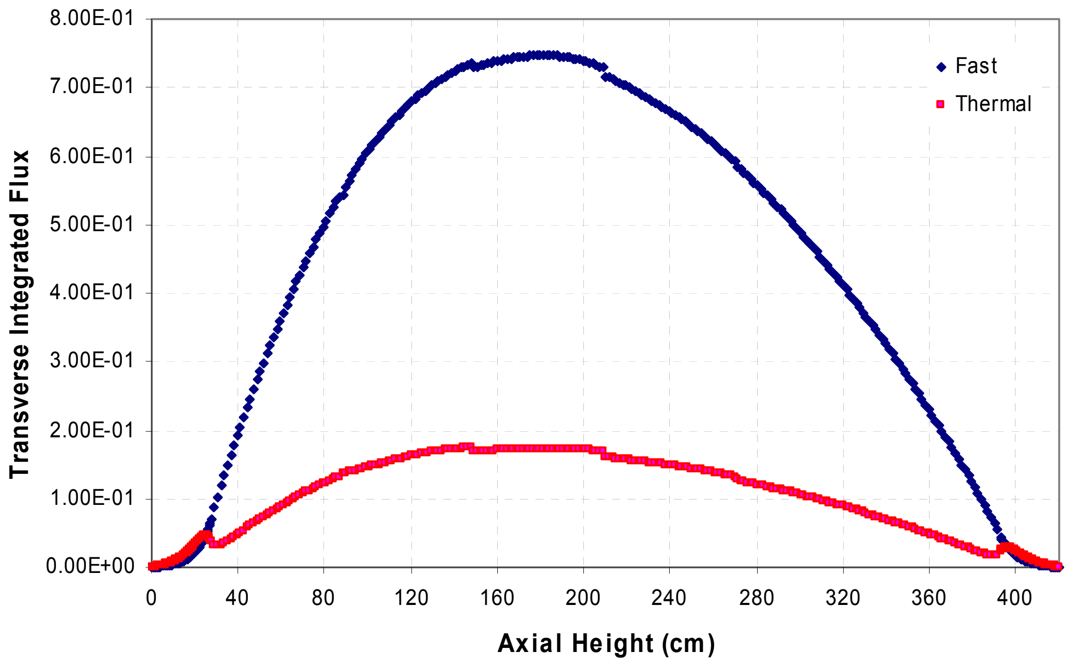

Figure 3.9 Coarse Mesh Flux Shape Calculated Using Approach 3

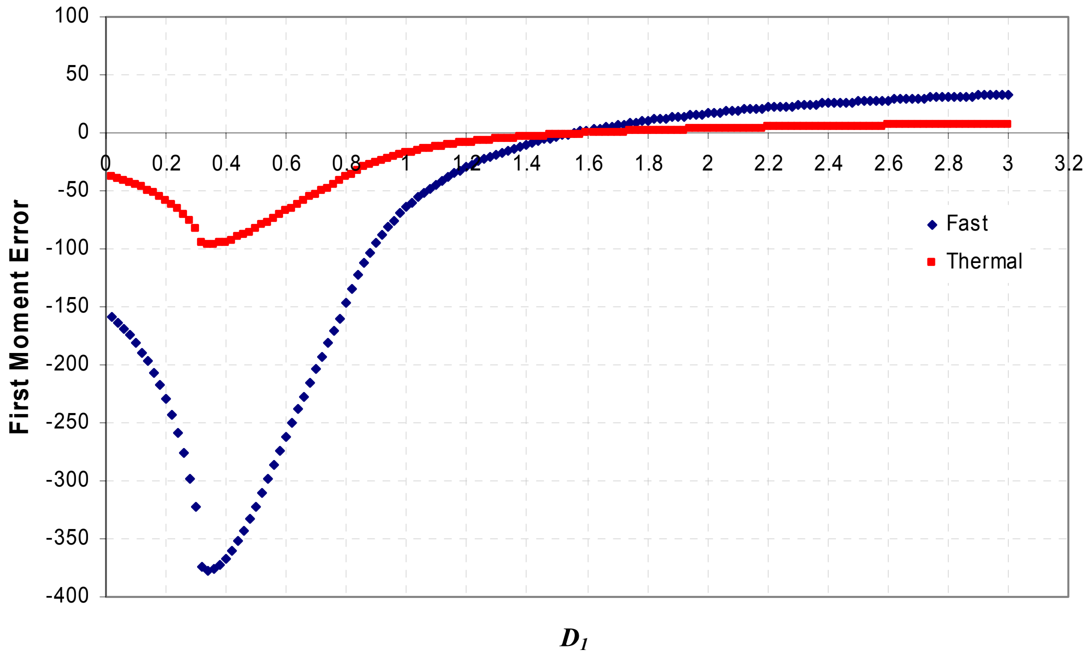

Figure 3.10 **Change In The First Moment Error with D_1 for Node 5**

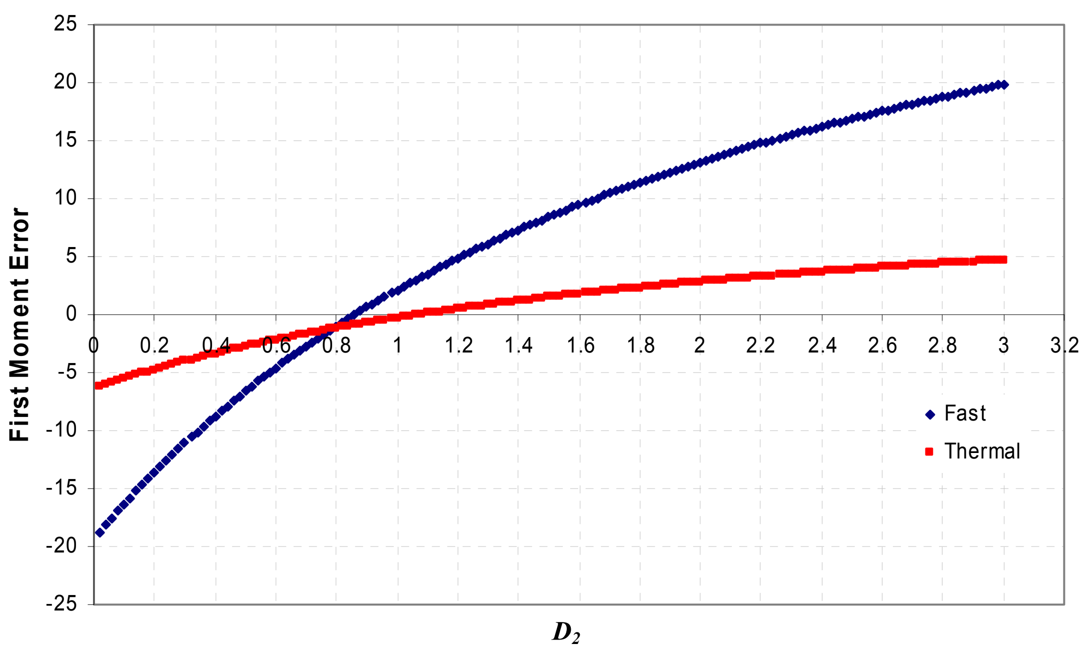

Figure 3.11 **Change In The First Moment Error with D_2 for Node 5**

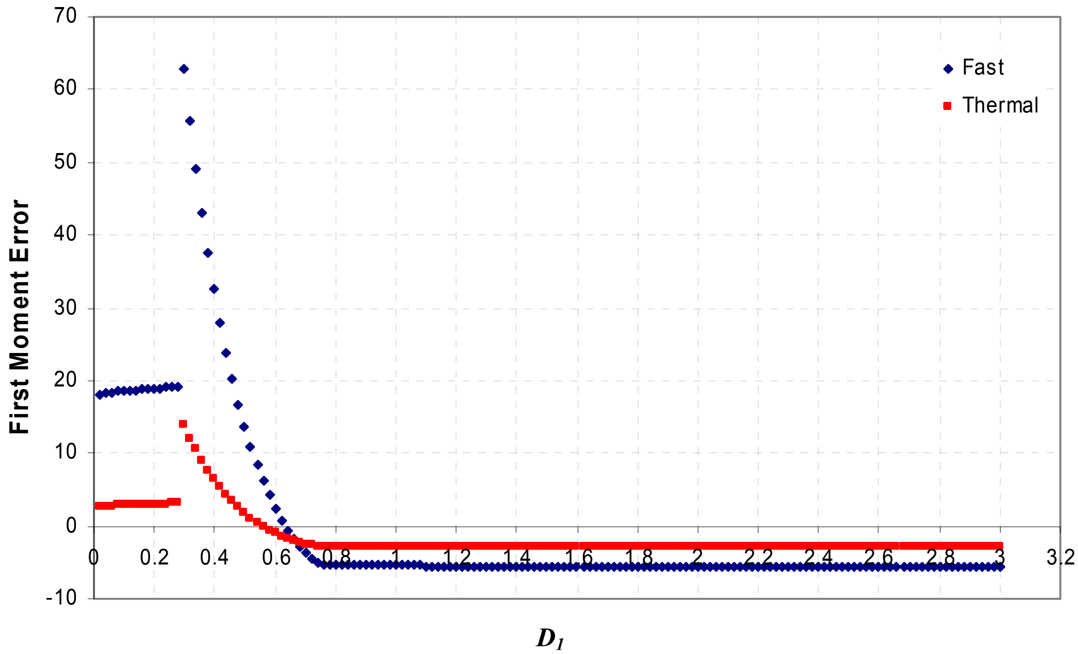

Figure 3.12 Change In The First Moment Error with D_1 For Node 6

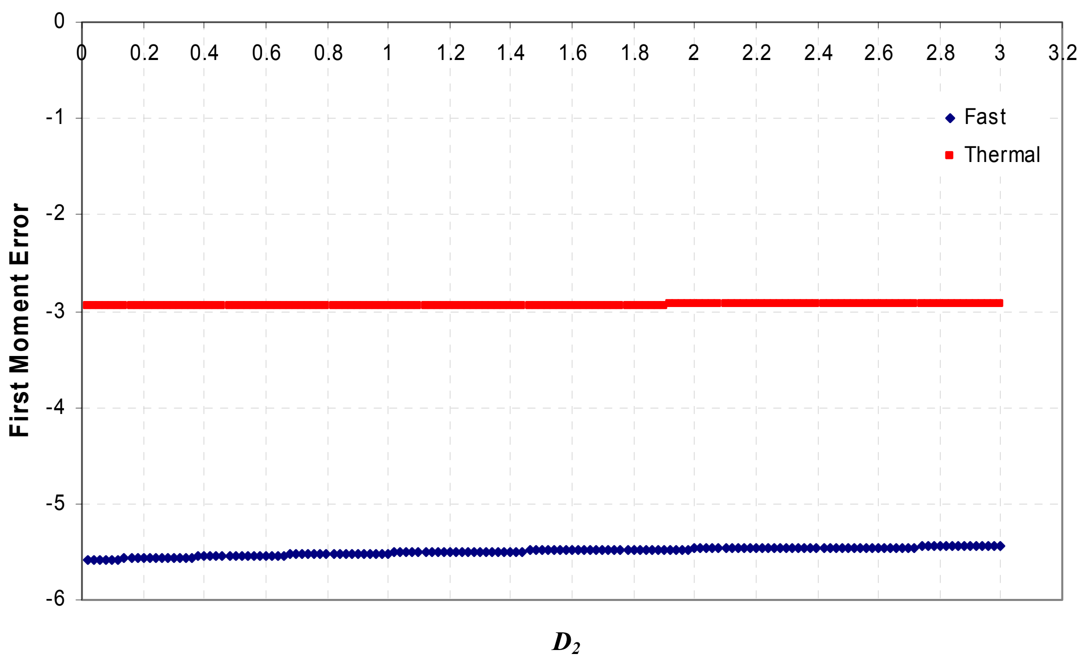

Figure 3.13 Change in the First Moment Error with D_2 for node 6

3.2 Transverse Leakage Approximation

The transverse leakage shape is a key approximation employed in the advanced nodal methods for the exact solution of the 3-D diffusion equation. There have been many approaches tried to improve the transverse leakage approximation as mentioned in Chapter 1. Although the accuracy of the quadratic expansion is acceptable and employed in many nodal codes, it can cause a non-physical Super-Nodal flux shape for the nodes close to the fundamental mode criticality as stated in Section 3.1.1. In this section three different transverse leakage approximations are presented in an effort to prevent the fundamental mode singularity either by improving the transverse leakage approximation or by transforming it into a convenient form so that the buckling term can be altered.

3.2.1 Spline Approach

The coefficients of the quadratic transverse leakage fit are calculated by requiring the intra-nodal transverse leakage shape to satisfy the node average transverse leakages of the node of interest and the two neighboring nodes, extending the polynomial across the neighboring nodes. This leads to discontinuity of the transverse leakage on the surfaces when one uses, quadratic fits of the adjacent nodes evaluated at their common surface. The spline approach is developed to provide physical constraints to the transverse leakage shape, which can be explained as follows:

For simplicity in the derivation, first assume that the original core is composed of homogenous regions (*ADF=1*). The partial current $\vec{J}$ is continuous in the direction that it is pointing, whereas the flux ϕ is continuous in all directions. Since ϕ is continuous across the interface in Figure 3.14, the derivative of the flux in the direction perpendicular to the normal of the surface is also continuous. This implies,

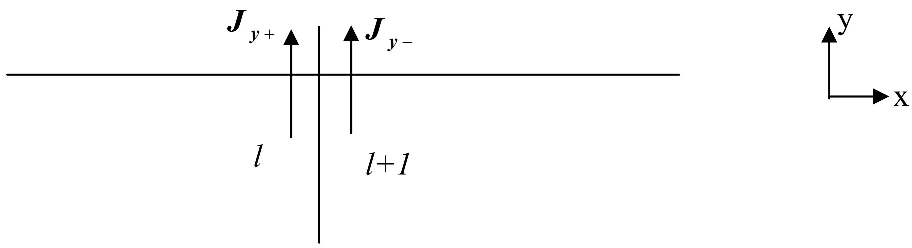

Figure 3.14 Transverse Leakage Jump Discontinuity

$$\left.\frac{\partial \boldsymbol{\phi}^{l}}{\partial \boldsymbol{y}}\right|_{+}=\left.\frac{\partial \boldsymbol{\phi}^{l+1}}{\partial \boldsymbol{y}}\right|_{-} \tag{3.5}$$

Using Fick's Law the current continuity across the interface between node l and node $l+1$ can be written as,

$$\boldsymbol{D}^{l}\frac{\partial}{\partial \boldsymbol{x}}\boldsymbol{\phi}^{l}\,|_{+}=\boldsymbol{D}^{l+1}\frac{\partial}{\partial \boldsymbol{x}}\boldsymbol{\phi}^{l+1}\,|_{-} \tag{3.6}$$

Equations (3.5) and (3.6) also imply that,

$$\boldsymbol{D}^{l}\frac{\partial^{2}}{\partial \boldsymbol{x}\partial \boldsymbol{y}}\boldsymbol{\phi}^{l}\,|_{+}=\boldsymbol{D}^{l+1}\frac{\partial^{2}}{\partial \boldsymbol{x}\partial \boldsymbol{y}}\boldsymbol{\phi}^{l+1}\,|_{-} \tag{3.7}$$

Recall that the transverse leakage is defined as

$$\boldsymbol{L}|_{\pm}=-\boldsymbol{D}\left.\frac{\partial \boldsymbol{\phi}}{\partial \boldsymbol{y}}\right|_{\pm} \tag{3.8}$$

Inserting Equation (3.8) into Equations (3.5) and (3.7) provides two constraints for the transverse leakage shape

$$\left.\frac{\boldsymbol{L}^{l}}{\boldsymbol{D}^{l}}\right|_{+}=\left.\frac{\boldsymbol{L}^{l+1}}{\boldsymbol{D}^{l+1}}\right|_{-} \tag{3.9}$$

and

$$\left.\frac{\partial \boldsymbol{L}^{l}}{\partial \boldsymbol{x}}\right|_{+}=\left.\frac{\partial \boldsymbol{L}^{l+1}}{\partial \boldsymbol{x}}\right|_{-} \tag{3.10}$$

These two constraints couple the nodes in the direction of the transverse integrated equation solution, therefore the transverse leakage coefficients of all the nodes in the direction of the solution need to be calculated simultaneously. The coefficient matrix is block diagonal and the Thomas Algorithm [33] can be employed.

The spline approach is tested using a three loop fresh fuel loaded PWR core. The details of the core model are given in Chapter 4. The error in the radial power shape for the conventional quadratic approach and the spline approach are given in Table 3-6. The reference solution for this problem is obtained by refining each node to 2x2 radial nodes. Both methods produce the same power map for the reference nodalization. For the unrefined radial mesh, although the spline approach reduces the radial power error, the real advantage of this method comes from Equation (3.5) and Equation (3.7), which allows us to express the constraints on the transverse leakage as a function of intra-nodal flux shape. Hence, the spline approach fits nicely into the “buckling shifting” approach to modify the buckling term at singular nodes which have the fundamental mode singularity problem as an alternative to the “coordinate shifting” approach.

Now consider a heterogeneous region that has been homogenized. The heterogeneous flux can be related to the homogenous flux employing CMDF’s as,

$$\left.\boldsymbol{\phi}^{Het}(\boldsymbol{y})\right|_{\pm}=\left.\boldsymbol{\phi}^{Hom}(\boldsymbol{y})\right|_{\pm}\left.\boldsymbol{CMDF}(\boldsymbol{y})\right|_{\pm} \tag{3.11}$$

Then the derivative of the flux in the y direction becomes

$$\left.\frac{\partial \boldsymbol{\phi}^{Het}}{\partial \boldsymbol{y}}\right|_{\pm} = \left.\frac{\partial (\boldsymbol{\phi}^{Hom} \boldsymbol{CMDF})}{\partial \boldsymbol{y}}\right|_{\pm} \tag{3.12}$$

which can be expanded as,

$$\left.\frac{\partial (\boldsymbol{\phi}^{Hom} \boldsymbol{CMDF})}{\partial \boldsymbol{y}}\right|_{\pm} = \left.\frac{\partial \boldsymbol{\phi}^{Hom}}{\partial \boldsymbol{y}}\right|_{\pm} \boldsymbol{CMDF}_{\pm} + \left.\frac{\partial \boldsymbol{CMDF}}{\partial \boldsymbol{y}}\right|_{\pm} \left.\boldsymbol{\phi}^{Hom}\right|_{\pm} \tag{3.13}$$

The corner point CMDFs and the derivative of CMDF in the y direction are unknown; therefore, Equation (3.5) cannot be easily utilized for homogenized nodes. Assuming the second term on the RHS of equation (3.13) is small versus the first term, so can be ignored, and setting the corner point CMDFs to unity, tests revealed the spline approach does not produce accurate results when the ratio of CMDFs at the interface become larger.

Table 3-6 Comparison of Spline Approach Versus the Quadratic Approach

Y|X	1	2	3	4	5	6	7	8
1	1.2720	1.2226	1.3015	1.1802	1.1669	0.9930	0.9183	0.7120
	0.0011	0.0019	0.0008	0.0013	0.0000	0.0000	-0.0014	-0.0017
	0.0001	0.0001	0.0000	-0.0001	-0.0002	-0.0003	-0.0005	**-0.0005**
2	1.2226	1.3125	1.2982	1.2652	1.1528	1.0479	0.9013	0.5475
	0.0019	0.0010	0.0017	0.0005	0.0007	-0.0007	-0.0009	-0.0014
	0.0001	0.0001	0.0000	-0.0001	-0.0002	-0.0003	-0.0004	-0.0003
3	1.3015	1.2982	1.3151	1.2232	1.1322	0.9473	0.8271	
	0.0008	0.0017	***0.0006***	0.0010	-0.0002	-0.0003	-0.0015	
	0.0000	0.0000	***-0.0002***	-0.0002	-0.0003	-0.0004	-0.0004	
4	1.1802	1.2652	1.2232	1.1614	0.9893	0.8691	0.5595	
	0.0013	0.0005	0.0010	-0.0001	-0.0001	-0.0011	-0.0007	
	-0.0001	-0.0001	-0.0002	-0.0003	-0.0003	-0.0004	-0.0004	
5	1.1669	1.1528	1.1322	0.9893	0.8513	0.6336		
	0.0000	0.0007	-0.0002	-0.0001	-0.0008	-0.0011		
	-0.0002	-0.0002	-0.0003	-0.0003	-0.0003	-0.0003		
6	0.9930	1.0479	0.9473	0.8691	0.6336			
	0.0000	-0.0007	-0.0003	-0.0011	-0.0011			
	-0.0003	-0.0003	-0.0004	-0.0004	-0.0003			
7	0.9183	0.9013	0.8271	0.5595				
	-0.0014	-0.0009	-0.0015	-0.0007				
	-0.0005	-0.0004	-0.0004	-0.0004				
8	0.7120	0.5475						
	-0.0017	-0.0014						
	-0.0005	-0.0003						

Reference Solution
Quadratic Approach Error
Spline Approach Error

bold denotes the maximum error
italic denotes the error at the maximum peak power

RMS
5.05E-04
1.19E-04

3.2.2 Cubic Polynomial Approach

One way of preventing the zero buckling singularity is to solve the coupled transverse integrated diffusion equation for the special case of buckling set exactly to zero and use that solution for the nodes near criticality [17]. This approach uses the fact that the particular solution has more constraints when the buckling is zero, and that these constraints can be satisfied by using higher order transverse leakage polynomials. In other words, the solution is consistent when buckling is exactly zero and can still be used when the buckling is in the neighborhood of zero. A similar approach is taken to derive the cubic transverse leakage approximation to prevent the fundamental mode singularities.

Starting with the one-node problem constraints (suppressing node l dependence throughout this derivation)

$$-\left(\boldsymbol{D}_g \frac{d\boldsymbol{\phi}_g^H}{d\boldsymbol{x}}\bigg|_{-\Delta x/2} + \boldsymbol{D}_g \frac{d\boldsymbol{\phi}_g^P}{d\boldsymbol{x}}\bigg|_{-\Delta x/2} \right) = \boldsymbol{J}_g^- \tag{3.14}$$

and

$$-\left(\boldsymbol{D}_g \frac{d\boldsymbol{\phi}_g^H}{d\boldsymbol{x}}\bigg|_{\Delta x/2} + \boldsymbol{D}_g \frac{d\boldsymbol{\phi}_g^P}{d\boldsymbol{x}}\bigg|_{\Delta x/2} \right) = \boldsymbol{J}_g^+ , \tag{3.15}$$

inserting the intra-nodal flux solution from Equation (2-53) into Equation (3.14) and Equation (3.15), and setting $\frac{\kappa \Delta z}{2} = \frac{\pi}{2}$, the two group net currents become,

$$-D_1(ra_{22}\kappa + s\mu(a_{23}\cosh(\mu\frac{\Delta z}{2}) + a_{24}\sinh(\mu\frac{\Delta z}{2})) + D_1 \frac{d\phi_1^P}{dx}\bigg|_{-\Delta x/2} = J_1^- \tag{3.16}$$

$$-D_2(a_{22}\kappa+\mu(a_{23}\cosh(\mu\frac{\Delta z}{2})+a_{24}\sinh(\mu\frac{\Delta z}{2}))-D_2\frac{d\phi_2^P}{dx}\bigg|_{-\Delta x/2}=J_2^- \tag{3.17}$$

$$-D_1(-ra_{22}\kappa+s\mu(a_{23}\cosh(\mu\frac{\Delta z}{2})-a_{24}\sinh(\mu\frac{\Delta z}{2}))-D_1\frac{d\phi_1^P}{dx}\bigg|_{\Delta x/2}=J_1^+ \tag{3.18}$$

$$-D_2(-a_{22}\kappa+\mu(a_{23}\cosh(\mu\frac{\Delta z}{2})-a_{24}\sinh(\mu\frac{\Delta z}{2}))-D_2\frac{d\phi_2^P}{dx}\bigg|_{\Delta x/2}=J_2^+ \tag{3.19}$$

Because of the zero cosine term, there are 4 equations and 3 unknowns. Therefore one equation must be linearly dependent upon the others. Summing Equations (3.16) through (3.19) group wise, two equations are obtained for a_{23}

$$-D_1(2s\mu a_{23}\cosh(\mu\frac{\Delta z}{2}))-D_1\frac{d\phi_1^P}{dx}\bigg|_{\Delta x/2}-D_1\frac{d\phi_1^P}{dx}\bigg|_{-\Delta x/2}=J_1^++J_1^- \tag{3.20}$$

and

$$-D_2(2\mu a_{23}\cosh(\mu\frac{\Delta z}{2}))-D_2\frac{d\phi_1^P}{dx}\bigg|_{\Delta x/2}-D_2\frac{d\phi_1^P}{dx}\bigg|_{-\Delta x/2}=J_2^++J_2^- \tag{3.21}$$

Calculating a_{23} from Equation (3.20) and inserting into Equation (3.21), a constraint between the fast and thermal group particular solution of the fluxes is obtained as follows,

$$\frac{s}{D_1}\left[J_1^++J_1^-+D_1\frac{d\phi_1^P}{dx}\bigg|_{\Delta x/2}+D_1\frac{d\phi_1^P}{dx}\bigg|_{-\Delta x/2}\right]=\frac{1}{D_2}\left[J_2^++J_2^-+D_2\frac{d\phi_2^P}{dx}\bigg|_{\Delta x/2}+D_2\frac{d\phi_2^P}{dx}\bigg|_{-\Delta x/2}\right] \tag{3.22}$$

The particular solution $\phi_g^P(x)$ is dependent on the transverse leakage shape. Therefore Equation (3.22) is in fact a constraint on the transverse leakage approximation for a consistent solution. This constraint can be used to obtain a cubic thermal and fast transverse leakage polynomial, or by setting both sides of Equation (3.22) to zero, to obtain a cubic thermal and fast transverse leakage polynomial approximation.

A similar constraint for the transverse leakages can be derived for the two node problem involving nodes near fundamental mode criticality. Unfortunately, the cubic polynomial approach for the two-node problem couples neighboring nodes and does not provide enough constraint to solve for the transverse leakages without additional assumptions. Although this approach was found to improve the flux shape at the critical nodes, it was found not to be robust for the nodes not exactly critical.

3.2.3 Least Squares Approach

The least-squares approach is very similar to the transverse leakage approximation in the buckling shifting algorithm given in Section 2.2.5.1. The main idea is to approximate the quadratic transverse leakage polynomial as a function of the intra nodal flux shape. A similar approximation was done earlier by Finneman [5]. The approximation is based on the separability of flux and performs poorly as the heterogeneity increases in the reactor. In the least squares approach, a quadratic correction term is added to correct for the non-separability. The coefficients of this residual quadratic polynomial are obtained to reduce the least squares difference between this new form of the transverse leakage and the quadratic approximation by least squares. Dropping the energy group dependence *g,* the least squares transverse leakage approximation for node *l* is defined as,

$$\widetilde{L}^l(z) = {B^l_{xy}}^2 \phi^l(z) + \Delta\widetilde{L}^l(z) \tag{3.23}$$

where

$$\Delta\widetilde{L}^l(z) = \widetilde{b}_1^l f_1(z) + \widetilde{b}_2^l f_2(z) \tag{3.24}$$

and

$$ {B^l_{xy}}^2 = \frac{\overline{L}^l}{\overline{\phi}^l} \tag{3.25}$$

The coefficients of $\Delta\widetilde{L}^l(z)$ are calculated by minimizing,

$$E = \int_{-\Delta z^l/2}^{\Delta z^l/2} \left(L^l(z) - \widetilde{L}^l(z) \right)^2 dz \tag{3.26}$$

which imposes,

$$\frac{\partial E}{\partial \widetilde{b}_i^l} = 0 \quad \boldsymbol{for\ i} = 0{,}1 \tag{3.27}$$

where $L^l(z)$ is the conventional quadratic leakage approximation defined as,

$$L^l(z) = \overline{L}^l + b_1^l f_1(z) + b_2^l f_2(z) \tag{3.28}$$

The $\phi^l(z)$ term in Equation (3.23) complicates the solution since it requires the intra-nodal flux shape for node *l* to be known in Equation (3.27) prior to the nodal solution. For that reason the following approaches are proposed:

a) Approximate Equation (3.23) by using the past iterative value of $\phi^l(z)$,

$$\widetilde{\boldsymbol{L}}^{l^n}(z) \approx \boldsymbol{B}_{xy}^{l\ 2}\boldsymbol{\phi}^{l^{n-1}}(z) + \Delta\widetilde{\boldsymbol{L}}^{l^n}(z) \tag{3.29}$$

noting that the coefficients of $\boldsymbol{\phi}^{l^{n-1}}(z)$ needs to be scaled to preserve node average flux at iteration *n*.

b) Calculate the intra-nodal flux shape $\boldsymbol{\phi}^{l}(z)$ iteratively using $\boldsymbol{\phi}^{l^{n-1}}(z)$ as the initial guess. This approach fails to converge.

c) Solve for $\boldsymbol{\phi}^{l^n}(z)$ and the residual polynomial expansion coefficients simultaneously.

Recall the solution of the one-node problem in Section 2.2.4. The particular and the homogenous solutions have the following relation,

$$\overline{\overline{\boldsymbol{A}}}\vec{\boldsymbol{a}} = \vec{\boldsymbol{m}} \tag{3.30}$$

where $\vec{a}$ is the coefficient vector of the homogenous solution and the $\vec{m}$ vector can be written as ,

$$\vec{\boldsymbol{m}} = \vec{\boldsymbol{h}} + \overline{\overline{\boldsymbol{H}}}\vec{\boldsymbol{c}} + \overline{\overline{\boldsymbol{K}}}\vec{\boldsymbol{c}}_0 \tag{3.31}$$

where $\vec{h}$, $\vec{c}$ and $\vec{c}_0$ are defined as

$$\vec{\boldsymbol{h}} = \begin{bmatrix} \overline{\boldsymbol{\phi}}_1 \\ \overline{\boldsymbol{\phi}}_2 \\ \boldsymbol{J}_1^- \\ \boldsymbol{J}_2^- \end{bmatrix} \quad \vec{c} = \begin{bmatrix} c_{11} \\ c_{12} \\ c_{21} \\ c_{22} \end{bmatrix} \quad \vec{c}_0 = \begin{bmatrix} c_{10} \\ c_{20} \end{bmatrix} \tag{3.32}$$

The coefficients of the particular solution are obtained from the transverse leakage coefficients. However, when the flux component of the transverse leakage is introduced on to the right hand side in Equation (3.23), the transverse leakage coefficients are replaced by the residual polynomial transverse leakage coefficients,

$$\overline{\overline{D}}\vec{c} = \vec{\tilde{L}} \tag{3.33}$$

where

$$\vec{\tilde{\boldsymbol{L}}} = \begin{bmatrix} \tilde{\boldsymbol{b}}_{11} \\ \tilde{\boldsymbol{b}}_{21} \\ \tilde{\boldsymbol{b}}_{12} \\ \tilde{\boldsymbol{b}}_{22} \end{bmatrix} \tag{3.34}$$

The vector $\vec{\tilde{L}}$ is calculated from Equation (3.27). If $\overline{\overline{\boldsymbol{G}}}$ is the least square coefficient matrix, the system of equations is of the form,

$$\overline{\overline{\boldsymbol{G}}}\vec{\tilde{\boldsymbol{L}}} = \overline{\overline{\boldsymbol{B}}}\vec{\boldsymbol{a}} + \vec{\boldsymbol{v}} \tag{3.35}$$

From Equations (3.35) and (3.33), $\vec{c}$ is calculated as

$$\vec{\boldsymbol{c}} = \overline{\overline{\boldsymbol{D}}}^{-1}\overline{\overline{\boldsymbol{G}}}^{-1}\left(\overline{\overline{\boldsymbol{B}}}\vec{\boldsymbol{a}} + \vec{\boldsymbol{v}}\right) \tag{3.36}$$

Inserting Equation (3.36) and (3.30) into Equation (3.31), one obtains the following equation which can be solved for $\vec{\boldsymbol{a}}$.

$$\left(\overline{\overline{\boldsymbol{A}}} - \overline{\overline{\boldsymbol{H}}}\overline{\overline{\boldsymbol{D}}}^{-1}\overline{\overline{\boldsymbol{G}}}^{-1}\overline{\overline{\boldsymbol{B}}}\right)\vec{\boldsymbol{a}} = \vec{\boldsymbol{h}} + \overline{\overline{\boldsymbol{H}}}\overline{\overline{\boldsymbol{D}}}^{-1}\overline{\overline{\boldsymbol{G}}}^{-1}\vec{\boldsymbol{v}} + \overline{\overline{\boldsymbol{K}}}\vec{\boldsymbol{c}}_0 \tag{3.37}$$

Knowing $\vec{\boldsymbol{a}}$, Equation (3.35) can be used to solve for the residual polynomial transverse leakage coefficients A similar derivation can be done for the two-node transverse leakages. However, as explained in Section 2.2.5.1, the quadratic polynomial fails to adequately represent the residual as the hyperbolic component of the intra-nodal flux gets larger. Therefore this method fails as the heterogeneity of the core or $\boldsymbol{B}_{xy}{}^2$ increases.

3.2.4 Pin Power Reconstruction Type Approach

The modern nodal methods provide a fast and accurate solution to the 3-D diffusion equation by assuming spatially constant neutronic properties within each node. Unfortunately this assumption, and separated one dimensional intra-nodal flux solution, causes the loss of detailed information about the flux and power distribution. This problem is solved by the development of various pin-power reconstruction methods. The general idea in pin power reconstruction is to provide a two dimensional higher order intra-nodal flux solution using the converged two radial plane, one dimensional nodal solutions. The first true pin-power reconstruction method by Koebke and Wagner [18] employs a pin-wise flux distribution for node *l* in the form of,

$$\phi_g^l(x,y)=\sum_{i,j}^{i+j\le 5} C_{gij}^l x^i y^j \tag{3.38}$$

The flux expansion in Equation (3.38) requires 21 constraints per node per group. The direct nodal solution provides only 9 constraints and the remaining twelve constraints are provided by corner point interpolations. The corner point flux and currents are calculated employing a lower order bi-quadratic flux shape in the form of

$$\phi_g^l(x,y)=\sum_{i,j}^{i+j\le 3} a_{gij}^l x^i y^j \tag{3.39}$$

Equation (3.39) has 8 coefficients per node per group and is solved over four nodes simultaneously as illustrated in Figure 3.15, from which the corner point fluxes and currents required to solve Equation (3.38) are obtained.

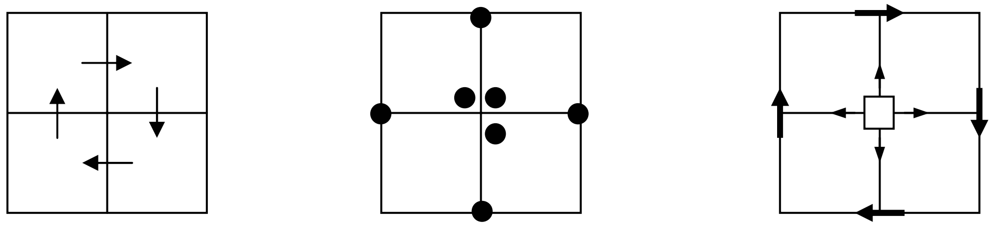

known values of surface fluxes surface currents node average fluxes | **continuity of corner fluxes** | **continuity of corner currents + no net source at the center**

20 + 7 + 5 = 32

Figure 3.15 Bi-Quadratic Pin-Power Reconstruction

A similar pin-power reconstruction method [34] expands the intra-nodal flux into a quartic polynomial with cross product terms for the fast flux and in terms of hyperbolic functions with an asymptotic slowing down component which is proportional to the fast group intra nodal flux for the thermal flux. The required 13 coefficients per group are calculated from 9 known nodal values. The remaining 4 constraints are obtained from corner point fluxes, which are extrapolated from calculations using surface average fluxes at the surfaces crossing that corner and the node average flux. Each node can be solved separately demanding less computer time.

Chang and his colleagues [15] developed an improved transverse leakage approximation which employs an analogous approach to Koebke and Wagner's pin-power reconstruction. Chang used a non separable quartic polynomial in Equation (3.39) to approximate the intra-nodal flux shape in 2–D

$$\phi_g^l(x,y) = \sum_{i,j}^{i+j\leq 4} C_{gij}^l f_i(x) f_j(y) \tag{3.40}$$

where $f_i(x)$ is the i^{th} order NEM polynomial. Using nine known nodal properties, corner point currents are written in terms of corner point fluxes. Then all nodes are coupled demanding zero net leakage around the corner points ("no-net source constraint"). All corner point fluxes are solved for simultaneously. The coefficients of Equation (3.39) are then calculated using corner point fluxes. The intra nodal flux is used to calculate a better estimate of the transverse leakage for the current iteration. Chang has developed this method for 2-D reactor analysis with homogenous regions (*ADF=1*).

The two pin-power reconstruction techniques presented above are developed to provide an accurate intra-nodal flux solution using the converged nodal solution. However, the calculation of the transverse leakages requires a computationally efficient method since transverse leakages are calculated for each nodal update. Although Chang's approach is computationally more efficient, it requires a solution of an N^2 coefficient matrix where N is the total number of nodes in 2-D. When Chang's approach is applied to 3-D this number increases to N^3. In addition, this transverse leakage approximation requires surface averaged flux values to be known prior to the transverse leakage calculation. Therefore, even if this method can be applied to the two-node problem using past iterative values; it cannot be applied to the one-node problem since the coarse mesh surface flux values are not known when initiating collapsing, *i.e.* solving the one-node problems.

Unfortunately, even as simple as a bi-quadratic expansion of the flux is in 3-D it requires 160 constraints for each 8 nodes, compared to 32 constraints for each 4 nodes in 2-D. This high number of constraints are difficult, if not impossible, to obtain in the absence of the surface flux information. Therefore, the pin-power reconstruction type approach to obtain a better estimate of the transverse leakage is impractical to employ in a 3-D super-nodal method.

4. Implementation and Results

4.1 Implementation

The developed Super Nodal method is implemented in the NESTLE 6.1 reactor core simulation code which employs ANM as the nodal kernel. The basic Super-Nodal algorithm illustrated in Figure 2.2 is implemented with a modification which allows multiple time steps at the fine mesh level after a refining step. A more detailed description of the Super-Nodal method is depicted in Figure 4.1.

Implementation of the refining step demands additional calculations at the coarse mesh level. Because of the semi implicit solution methodology employed for the T-H calculations in NESTLE, the past time step fine mesh T-H parameters are required to calculate the new time step fine mesh T-H parameters during a refining step. A solution to this problem is to continue to perform the T-H calculations at the fine mesh level even after the collapsing at $t=0$ sec. The fine mesh thermal-hydraulic parameters are then collapsed to provide coarse mesh T-H feedback parameters as explained in Section 2.2.2.3. This procedure provides more accurate coarse mesh T-H feedback calculations and the required past time step fine mesh T-H parameters for the refining step. A similar discussion is valid for calculation of the fine mesh fission product densities, *i.e.* Xe^{135} and Sm^{149}. Therefore the first follow-up step shown in Figure 4.1 also includes calculation of fine mesh fission product densities at the coarse mesh level. The second follow-up step is necessary for calculation of the fine mesh delayed neutron precursor densities. This step is placed at the end of each time step since it involves calculation of fine mesh fission and precursor densities which do not need iteration and can be calculated from refined coarse mesh flux, past time step fine mesh precursor densities and fine mesh fission cross section. The fine mesh cross sections are easily obtained using fine mesh T-H feedback parameters from the first follow-up step.

Another important point in the implementation is calculation of the rodded cross sections and CMDFs. As mentioned in discussing the error analysis in Section 2.3, it is not trivial to provide homogenization parameters for the nodes which were not rodded during collapsing and become rodded or partially rodded afterwards, or vice versa. Two approaches are proposed in Section 2.3. The first approach is to collapse the rodded and unrodded cross sections using the same flux shape. The second approach is similar to the approach in assembly calculations. The rodded cross sections are obtained by fully inserting the control rods and performing a collapsing step while the unrodded cross sections are obtained from collapsing when the control rods are fully withdrawn. In this research, the first approach is preferred to the second one. There are two reasons for this choice. First, the collapsing is performed in the axial direction and full insertion of the control rods only changes the magnitude of the flux but not the shape of the flux in the axial direction, causing the rodded and unrodded cross section to be collapsed using the same flux shape. Therefore, this approach produces the same results as the first approach and takes more CPU time. Second, it is not possible to use the second approach for collapsing during a transient to update the cross sections

Since a detailed error analysis is not covered in this research, the error checkpoints in the implementation in Figure 4.1 is replaced by predetermined time intervals for the fine and the coarse mesh calculations.

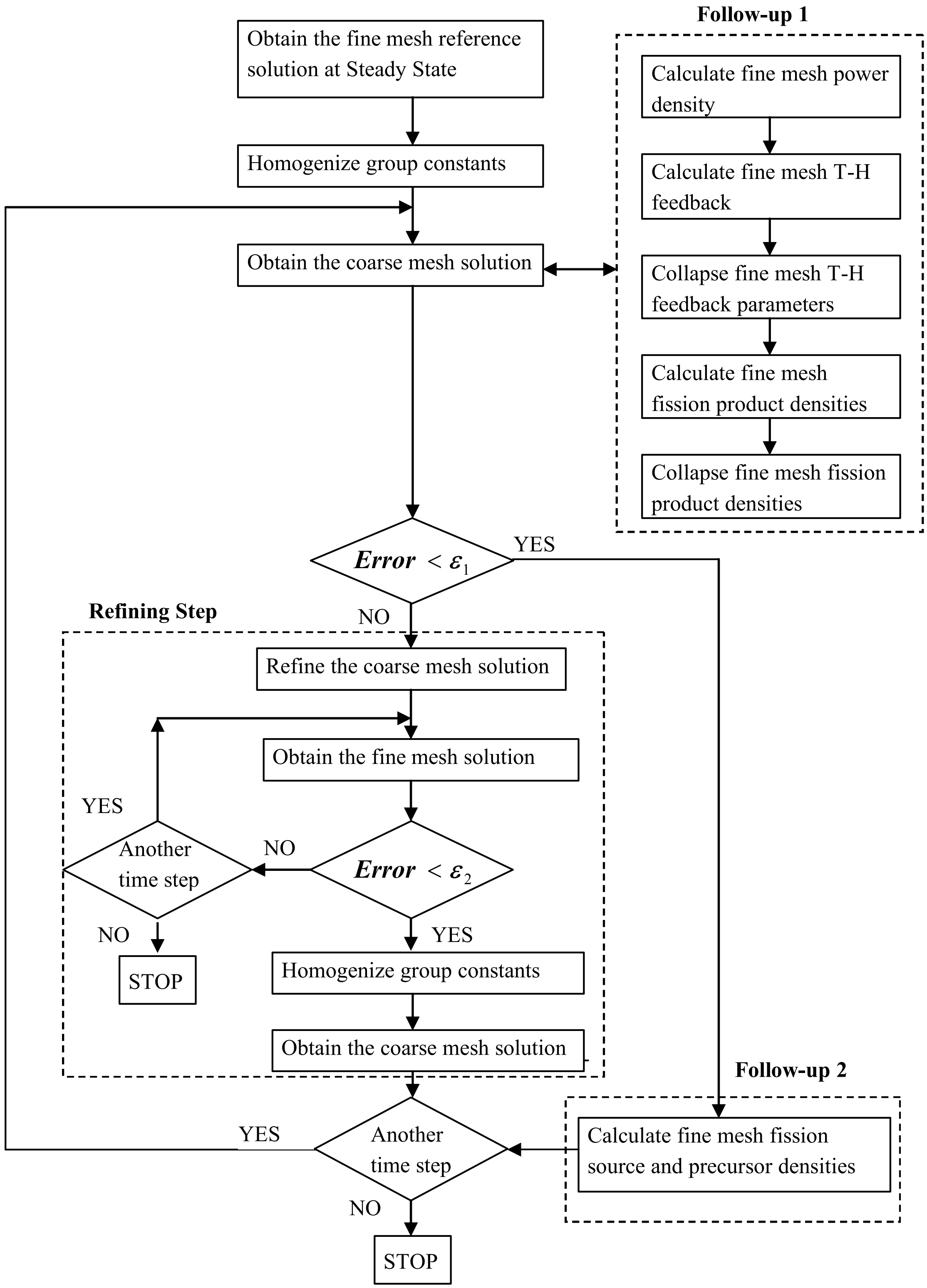

Figure 4.1 Implementation of the Super-Nodal Method

4.2 Results and Discussion

4.2.1 Test Cases

In this section, descriptions of four test cases are given and the computational performances of the developed Super-Nodal method for these test cases are presented. For each test case, the run times and accuracy of coarse mesh nodalization for different collapsing schemes are compared with the fine mesh solution. Collapsing from fine mesh to coarse mesh is always performed in the axial direction, although the present code allows collapsing in the radial direction as well. The radial direction collapse feature has never been tested. The fine mesh reference solutions for all test cases are obtained by using four nodes per assembly in the radial direction and 18 meshes in the axial direction. In the axial direction the fuel region is divided into 12 equally spaced meshes, while the reflector mixed and pure water regions are represented by one and two meshes, respectively, as shown in Figure 4.2. Two different coarse mesh nodalizations, SN1 and SN2, are used in this research. SN1 and SN2 coarse mesh nodalizations are illustrated in Figure 4.3 and Figure 4.4, respectively. In the SN1 nodalization, the core is axially collapsed from 18 nodes (30.48 cm fuel nodes) to 12 nodes (60.96 cm fuel nodes) by collapsing all nodes except the ones about the upper and lower fuel-reflector interfaces. In the SN2 nodalization, the core is axially collapsed from 18 nodes to 8 nodes by collapsing every two fuel nodes to one fuel node and by collapsing the reflector nodes to one node.

All four test cases presented in this section are based on a Westinghouse 3-Loop PWR core model. The reactor contains 157 fuel assemblies arranged in a checkerboard pattern radially. Each assembly has a radial dimension of 21.50x21.50 cm. The core is reflected radially and axially by 21.50 cm (minimum) and 27.40 cm of pure water, respectively. In addition, a homogenized baffle/former plate/reflector region that is 10.75 cm thick radially surrounds the core. The active core height is 365.76 cm. Quarter and full core geometry models of this core are given in Sections 4.2.2 and 4.2.3 in detail.

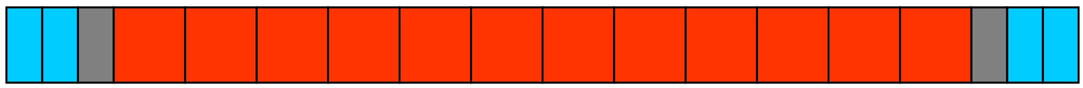

Figure 4.2 Fine Mesh Nodalization

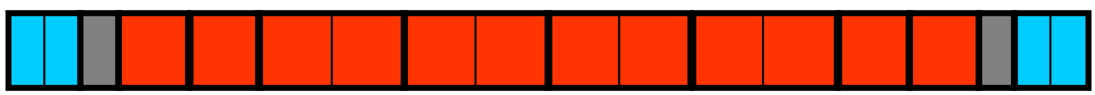

Figure 4.3 Coarse Mesh SN1 Nodalization

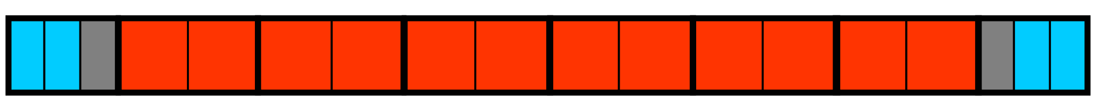

Figure 4.4 Coarse Mesh SN2 Nodalization

4.2.2 Test Case 1

This test problem is a small variation of the general core geometry presented in the previous section. A strong axial heterogeneity is introduced in four of the central fuel assemblies shown in Figure 4.5 by part length burnable rods. This test case is designed to show the effect of homogenization on an extreme case, as well as the effect of two singularity treatments. These singularity treatments are Buckling Shifting and Coordinate Shifting approaches that addresses two types of singularities, which are zero buckling and fundamental mode singularities as presented in Section 2.2.5.

For Beginning of Cycle (BOC) conditions, Figure 4.5 shows some of the radial node locations where the zero buckling singularity is seen. Figure 4.6 solution shows an un-converged flux shape for one of these radial nodes using the reference solution, *i.e.* fine mesh solution. The coarse mesh solution employing SN1 nodalization for the singular node introduces more singularity in the solution as seen in Figure 4.7. The buckling shifting approach helps convergence and the resulting fine and coarse mesh solutions have smaller discontinuities as seen in Figure 4.8 and Figure 4.9, respectively.

3	6	6	B	B	6	6	3	3	S_1	S_1	D	D	S_2	S_2	1	2	2
6	A	A	5	5	3	3	5	5	F	F	9	9	7	7	1	2	2
6	A	A	5	5	3	3	5	5	F	F	9	9	7	7	1	2	2
B	5	5	E	E	5	5	H	H	5	5	G	G	1	1	1	2	2
B	5	5	E	E	5	5	H	H	5	5	G	G	1	2	2	2	2
6	3	3	5	5	A	A	5	5	C	C	7	7	1	2	2	2	2
6	3	3	5	5	A	A	5	5	C	C	7	7	1	2	2		
3	5	5	H	H	5	5	3	3	7	7	1	1	1	2	2		
3	5	5	H	H	5	5	3	3	7	7	1	2	2	2	2		
S_1	F	F	5	5	C	C	7	7	1	1	1	2	2	2	2		
S_1	F	F	5	5	C	C	7	7	1	2	2	2	2				
D	9	9	G	G	7	7	1	1	1	2	2	2	2				
D	9	9	G	G	7	7	1	2	2	2	2						
S_2	7	7	1	1	1	1	1	2	2	2	2						
S_2	7	7	1	2	2	2	2	2	2								
1	1	1	1	2	2	2	2	2	2								
2	2	2	2	2	2												
2	2	2	2	2	2												

Legend:

(red)	Partial Length BP Assembly
S_1	Zero Buckling Singularity
S_2	Fundamental Mode Singularity
1	Reflector
2	Water

A,B,C,D,E,F,G,H: Control Rod Assemblies

Figure 4.5 Quarter Core Fuel Map for Test Case 1

The second type of singularity, fundamental mode singularity, is severer for axially heterogeneous nodes; therefore, the core is depleted to 15,000 MWD/MTU for this test. For the fuel node location marked as S_2 in Figure 4.5 the transverse integrated flux shape is plotted in Figure 4.18 and Figure 4.19 for the SN1 and SN2 nodalizations, respectively. A significant improvement is seen in Figure 4.16 and Figure 4.17 at the same radial node location after a coordinate shifting for $\varepsilon = -0.2$ is applied. Although these singularities cause non-realistic CMDF's, large CMDF's are also caused by homogenization of the nodes at the fuel reflector interfaces as seen in Figure 4.16 and Figure 4.17 for SN2 nodalization. However, the flux shapes for SN1 and SN2 nodalizations also differ at the central nodes. The different transverse leakage shapes obtained from these two nodalizations as shown in Figure 4.14 and Figure 4.15 are responsible for the differences in the remaining axial nodes, even though those nodes span the same axial length.

In the absence of any singularities, the Super-Nodal method can still produce unrealistic flux shapes if the homogenized nodes are strongly heterogeneous. Such behavior can be observed when the transverse integrated flux shape is plotted for a node in the BP assembly, as illustrated in Figure 4.16 and Figure 4.17. The effect of the heterogeneity is more drastic when the thermal-hydraulic feedback is treated for the same node, as seen in Figure 4.18 and Figure 4.19.

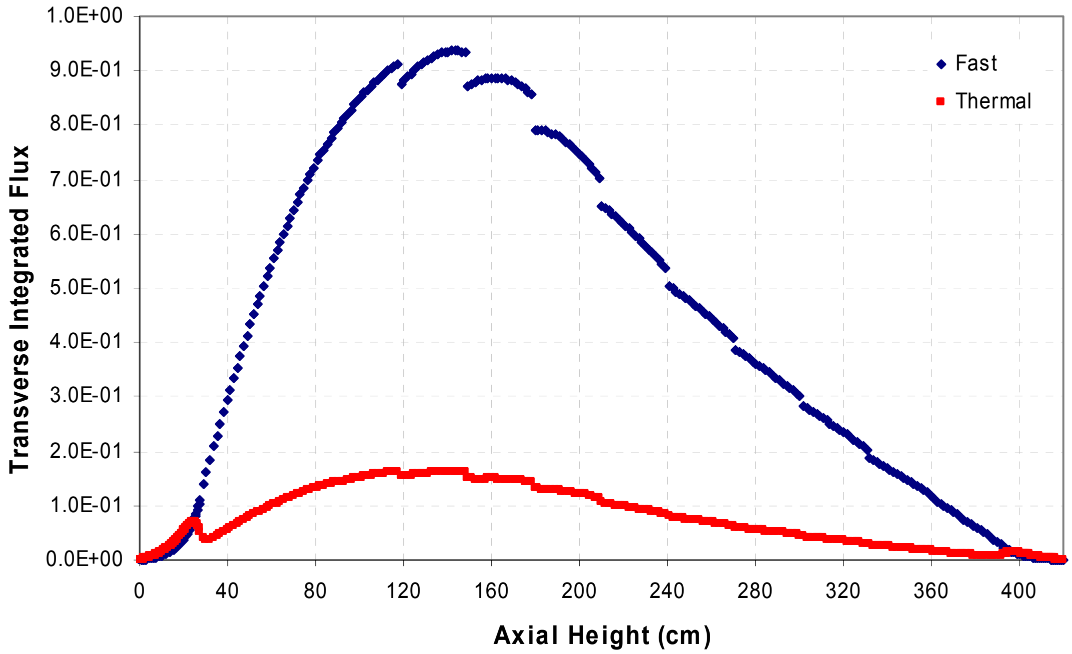

Figure 4.6 **Transverse Integrated Flux for the Reference Solution for a Node with Zero Buckling Singularity**

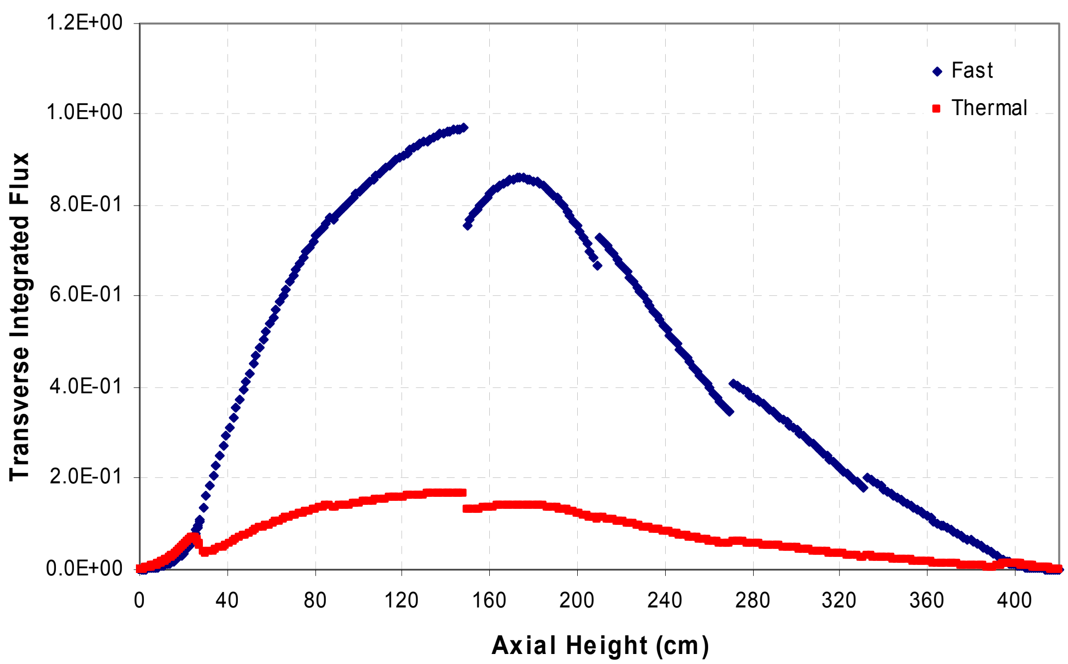

Figure 4.7 **Coarse Transverse Integrated Flux for SN1 Nodalization Solution for a Node with Zero Buckling Singularity**

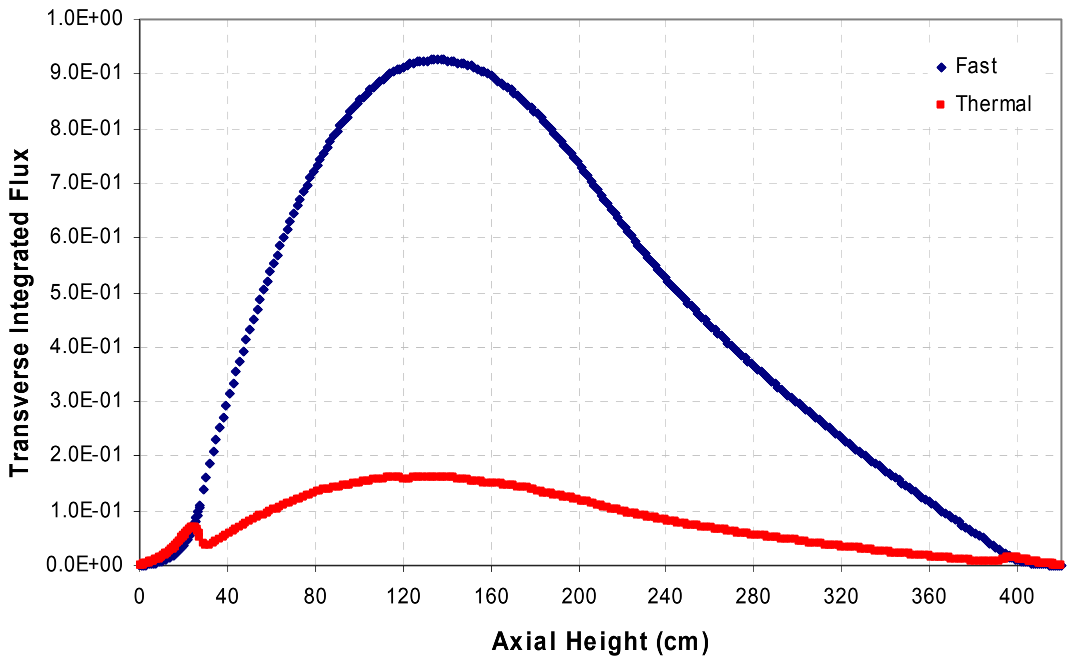

Figure 4.8 **Transverse Integrated Flux for the Reference Solution for a Node with Zero Buckling Singularity With the Buckling Shift Applied**

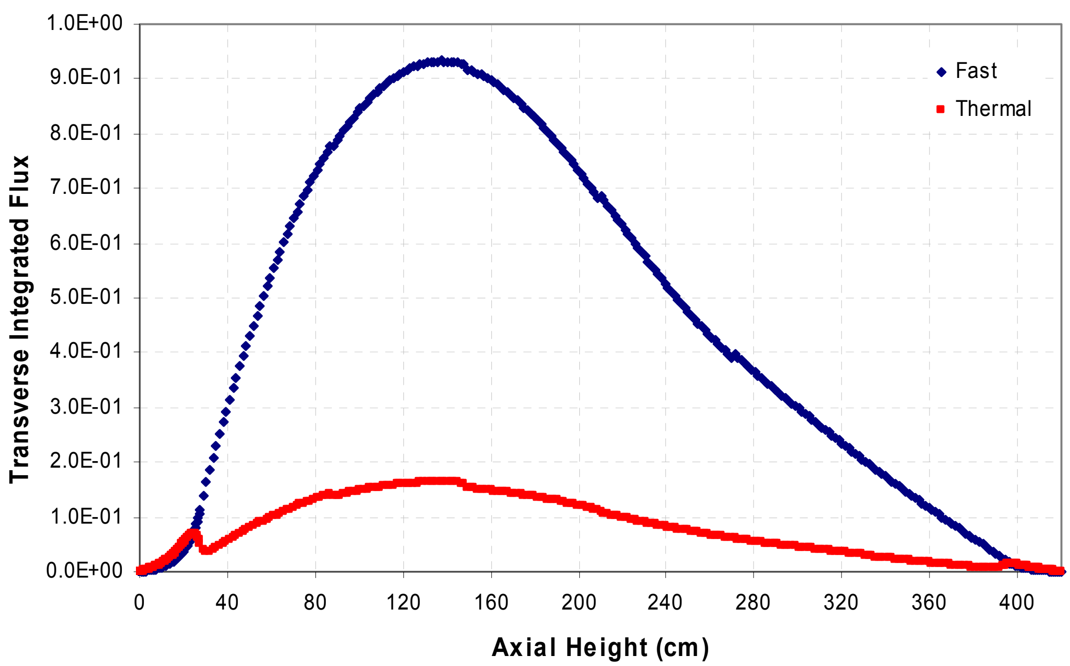

Figure 4.9 **Transverse Integrated Flux for the SN1 Nodalization for a Node with Zero Buckling Singularity with the Buckling Shift Applied**

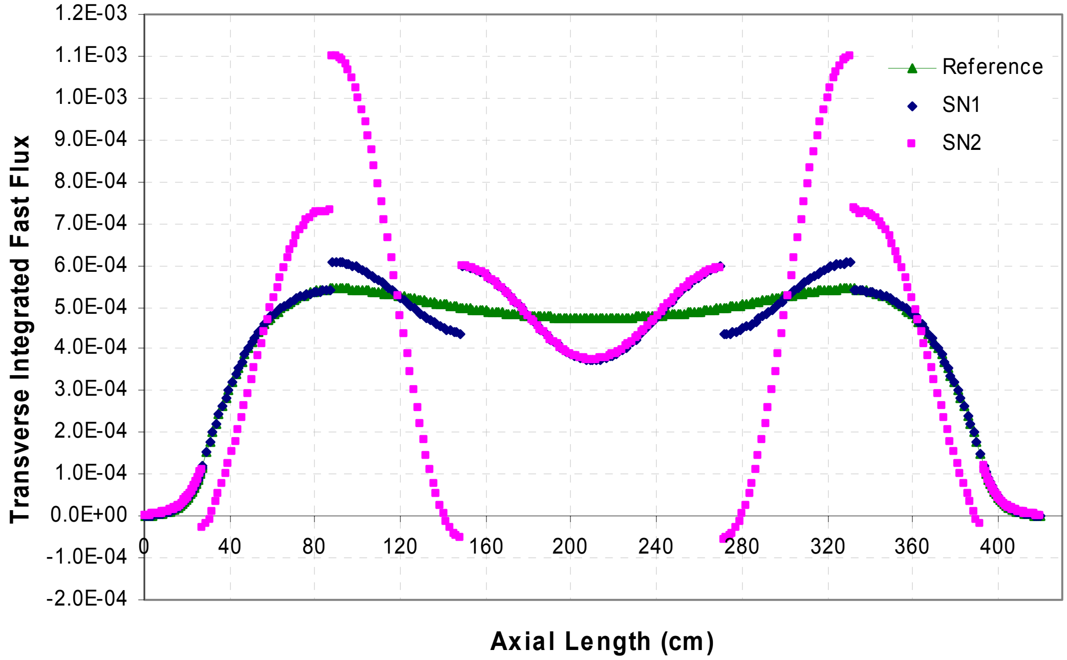

Figure 4.10 **Transverse Integrated Fast Flux for a Radial Node Location with the Fundamental Mode Singularity Problem.**

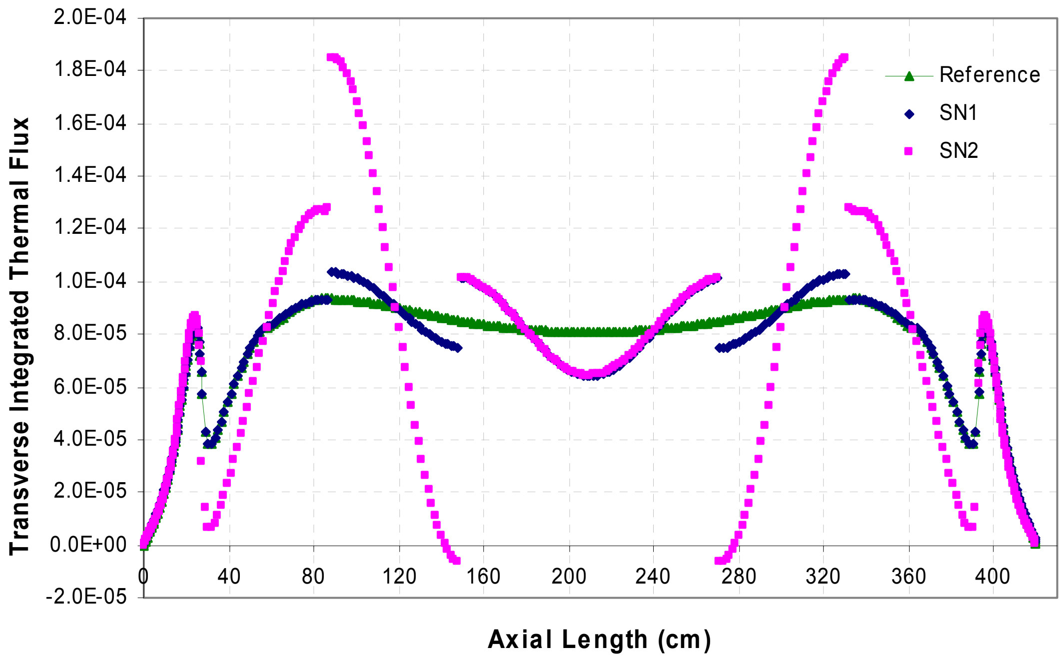

Figure 4.11 **Transverse Integrated Thermal Flux for a Radial Node Location with the Fundamental Mode Singularity Problem.**

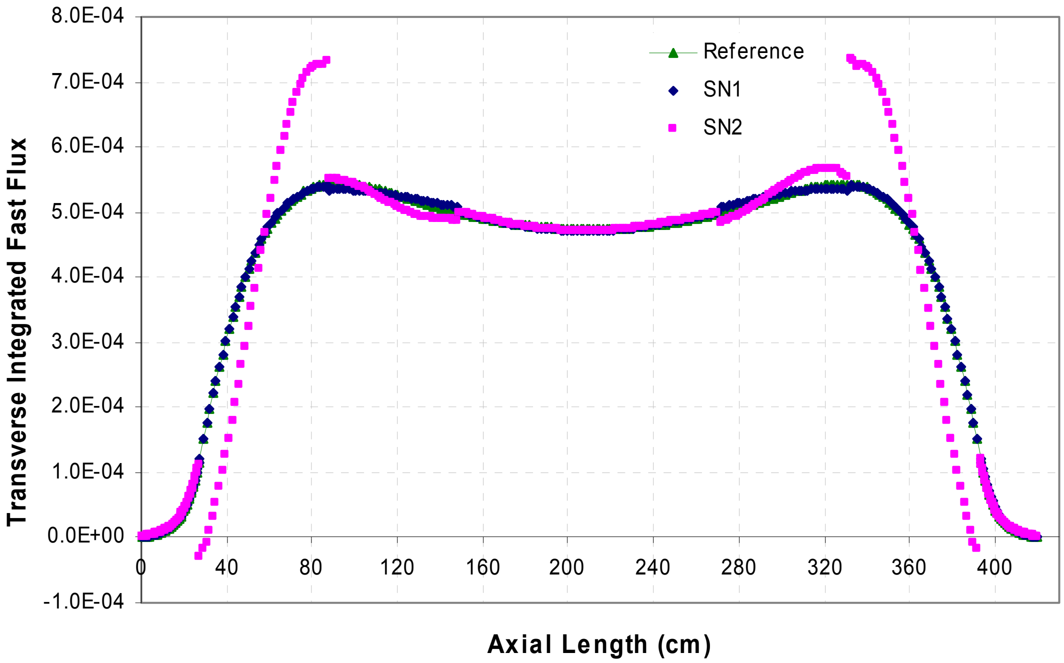

Figure 4.12 Transverse Integrated Fast Flux for a Radial Node Location with the Fundamental Mode Singularity Problem with Coordinate Shifting

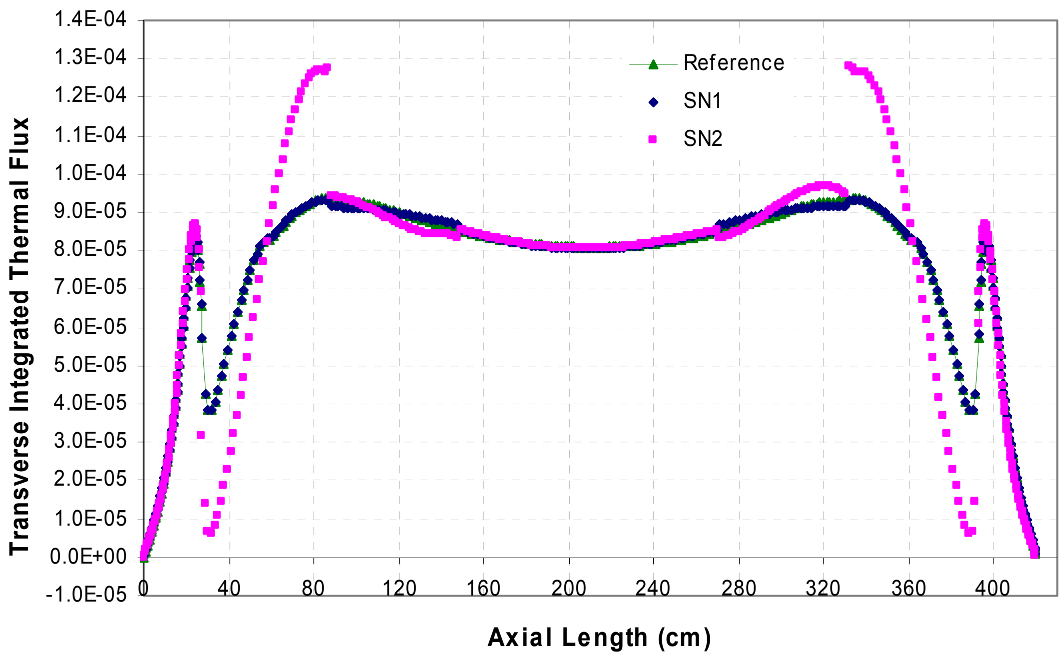

Figure 4.13 Transverse Integrated Thermal Flux for a Radial Node Location with the Fundamental Mode Singularity Problem After with the Coordinate Shifting.

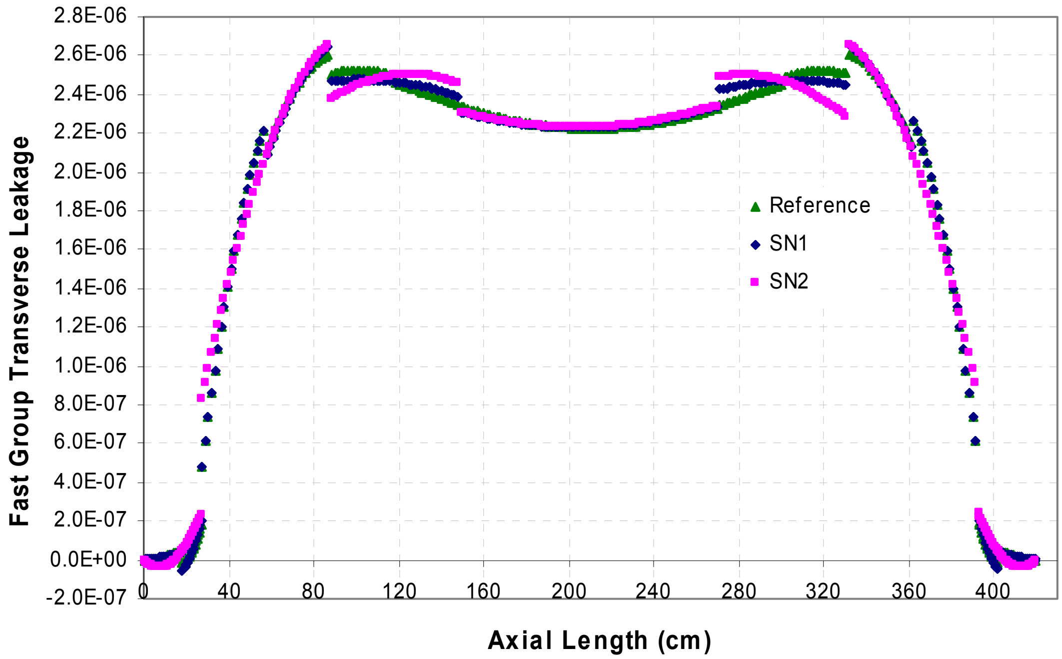

Figure 4.14 Fast Group Transverse Leakage for a Radial Node Location

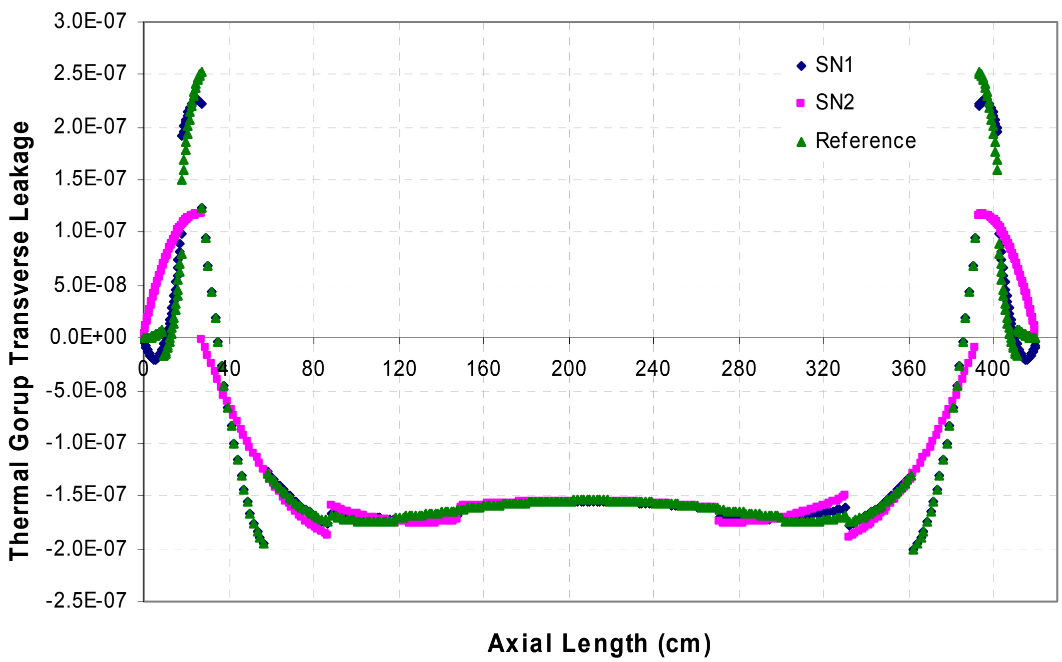

Figure 4.15 Thermal Group Transverse Leakage for a Radial Node Location

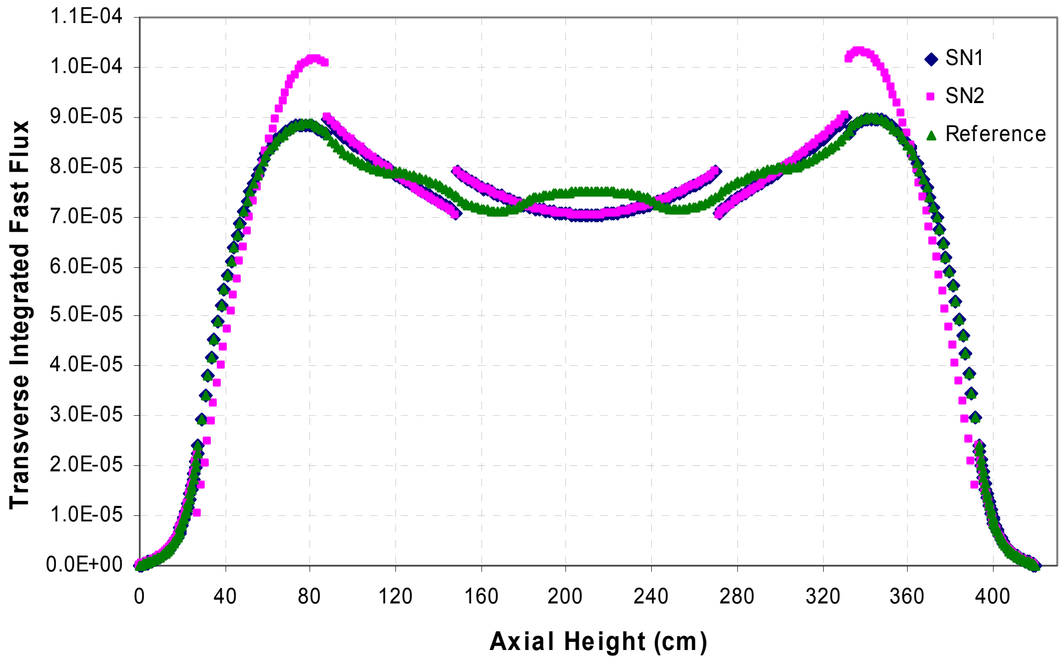

Figure 4.16 **Transverse Integrated Fast Flux for a Node in BP Assembly (w/o T-H Feedback)**

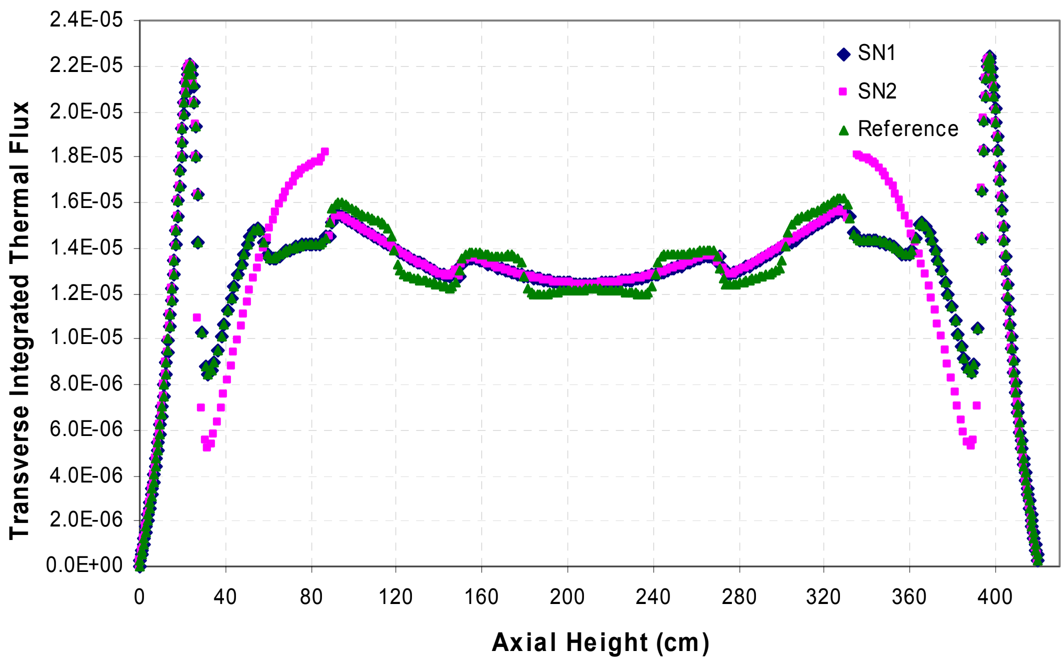

Figure 4.17 **Transverse Integrated Thermal Flux for a Node in The BP Assembly (w/o T-H Feedback)**

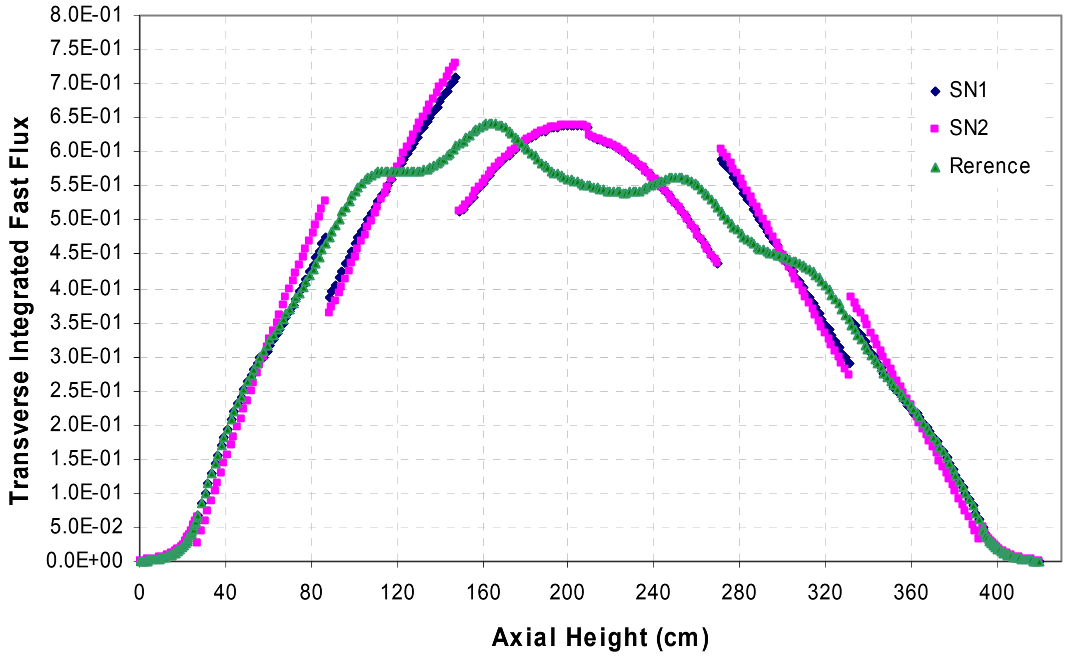

Figure 4.18 Transverse Integrated Fast Flux for a Node in BP Assembly (w/ T-H Feedback)

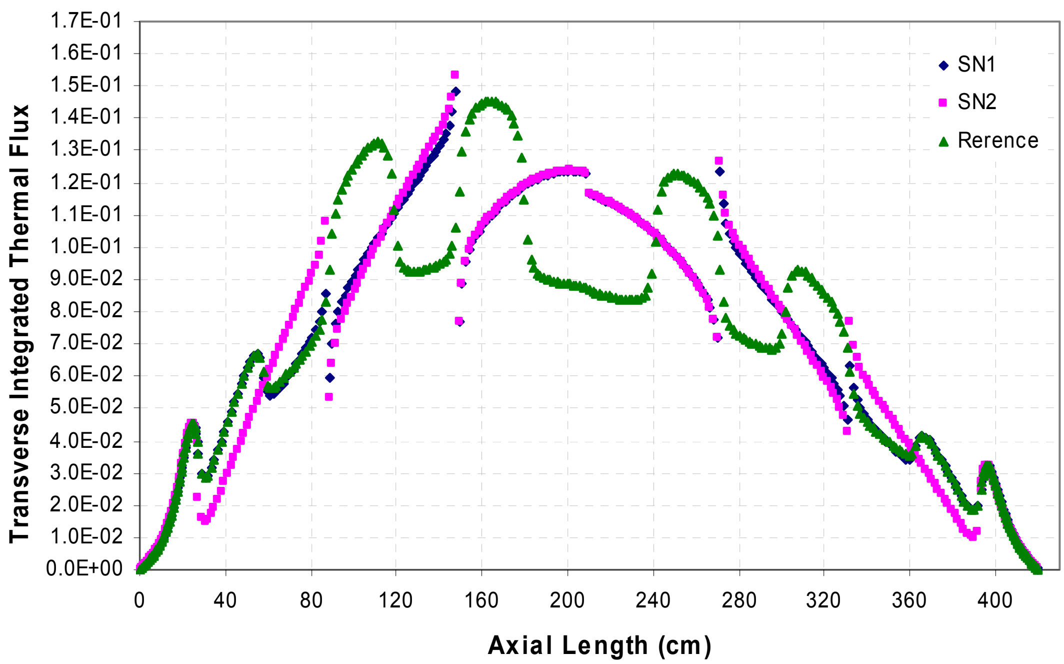

Figure 4.19. Transverse Integrated Thermal Flux for a Node in BP Assembly (w/ T-H Feedback)

4.2.3 Test Case 2

This test case is modeled to test SN1 and SN2 nodalizations for a severe control rod insertion transient, for the same depleted core model depicted in Figure 4.5. The transient is achieved by fully inserting Bank A over 25 seconds starting at 1 second, holding its position constant for 1 second, and linearly withdrawing it to its original position from 27 to 40 seconds as shown in Figure 4.20.

Three different collapsing schemes were compared with thermal-hydraulic feedback treated. For Scheme 1, the SN1 nodalization is used. The collapse occurs at 0 seconds and the resulting coarsened core model is used throughout the transient. For Scheme 2, the SN2 nodalization is used. The core model is again collapsed at 0 seconds. Finally, for Scheme 3 the core model is collapsed as in Scheme 1, but now refined several times during the transient. The coarse mesh solution is refined at 21 seconds and collapsed again at 22 seconds. At 29 seconds it is refined again and collapsed back to the SN1 nodalization at 31 seconds. This scheme is denoted as SN1-r in the figures. In all collapsing schemes the “rod cusping” treatment in NESTLE 6.1 is used to reduce the increased effect of “rod cusping” on the coarse nodalizations.

The reference, *i.e.* fine mesh predicted, peak node, core power level and associated errors as a function of time are shown in Figure 4.22 through Figure 4.27. The peak node powers (relative) are normalized such that the average node power equals 1; whereas, the peak node powers (% FP) are normalized such that the average node power equals the core power as % of full rated power.

All three cases demonstrate good agreement with the reference case for the core power level except at $t=20$ and $t=28$ seconds where the rod cusping effect is prominent in spite of the treatment that is used. The strong effect of thermal-hydraulic feedback is seen from the sudden drop in the power at $t=29$. The SN1 and SN2 schemes cannot follow this sudden change in the power accurately; however, the SN1-r scheme reduces the error considerably. The error in the peak node power (Figure 4.25) is more visible. The peak node power error increases with time for both SN1 and SN2 nodalizations, especially when the control rods are almost fully inserted. This increase in the error is expected since the homogenization parameters; such as CMDFs and homogenized cross section, lose their accuracy to represent the current status of the core as the core deviates from the state that the collapsing was performed at. Although a refine-collapse step improves the accuracy, the error is not zero since previous time step fine mesh parameters, used in the solution to recover fine mesh properties from coarse mesh properties, are approximated and hence, in error. The effect of the previous time step on the refined solution is obvious as the error increases at the first refined steps at 21 seconds and 29 seconds as seen in Figure 4.23 and Figure 4.25. The errors decrease sharply at the next refined solution steps since the past time errors become less important. Near the end of the transient, the SN1 scheme provides a more accurate result than the SN1-r scheme since the state of the reactor at the end of the transient is closer to the initial state of the reactor than when the last refine step was performed. Therefore, axial and radial power maps presented in Table 4-1 through Table 4-4, show that the RMS error for SN1-r is smaller at $t=26$ seconds than SN1, while the RMS error for SN1 is smaller than SN1-r at $t=40$ seconds. The relative residual also reflects this behavior of the collapsing schemes as shown in Figure 4.28. The large errors in the peak node powers between *18* and *32* seconds are also reflected in the axial power distribution. Table 4-2 shows that the SN1 and SN2 schemes miss the axial redistribution badly while the SN1-r scheme demonstrates good agreement with the reference solution.

The errors in peak node powers can be contributed to both the Super-Nodal solution errors and the errors in the flux form factors. In order to separate these two errors, the Super-Nodal solution peak node powers are calculated without employing flux form factors and compared with the collapsed fine mesh reference peak node powers for SN1 and SN2 nodalizations at each time step. The coarse mesh relative peak node powers and the associated errors are depicted for fine and coarse mesh determined peak node locations in Figure 4.29 through Figure 4.32, respectively. Since the fine and coarse mesh determined coarse mesh peak node locations are the same Figure 4.29 and Figure 4.31 are identical. Figure 4.30 shows a small reduction in the relative peak node power errors compared to Figure 4.25, which indicates that, the form factor errors are negligible in this test case.

The CPU times of the three collapsing schemes are compared with the reference solution in Table 4-5. The table shows that as the node size increases the run time decreases with an increasing number of outer iterations. The CPU time decreases as the number of nodes decreases as expected. On the other hand the increase in the number of outer iterations is also expected. As the node size increases, ANM corrections ($\tilde{\boldsymbol{D}}$ values) to the FDM calculated node leakages increase. Each ANM update is a perturbation on the converging FDM solution, therefore as the perturbation increases with the increased node size, more outer iterations are required for convergence. The thermal-hydraulic feedback is another factor in the increased number of outer iterations, since the change in the thermal-hydraulic feedback parameters is larger at increased node sizes. Table 4-5 also shows that considerable time is spent in the two refining steps. A large part of CPU time for the refining step is spent calculating the first fine mesh solution. Since the fine mesh $\tilde{\boldsymbol{D}}$ values are not known at the coarse mesh level, for the first fine mesh solution at the refining step, the last known fine mesh $\tilde{\boldsymbol{D}}$ values are used as the initial estimate. However, this estimate is usually bad since a refine step is required only when the state of the reactor deviates from the state that the collapsing is performed at. In other words, the last fine mesh $\tilde{\boldsymbol{D}}$ values are not able to accurately represent the current state of the reactor.

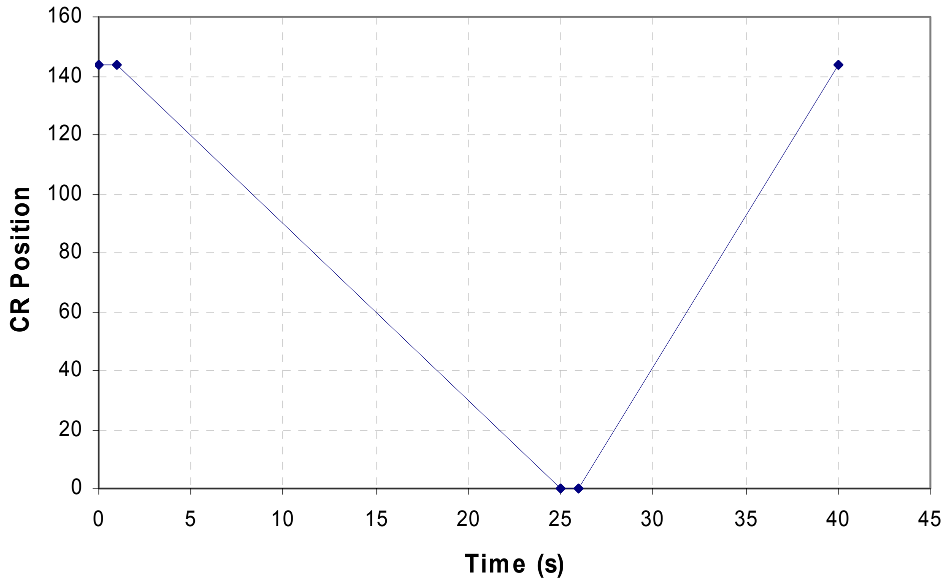

Figure 4.20 Control Rod Position Versus Time for Test Case 2

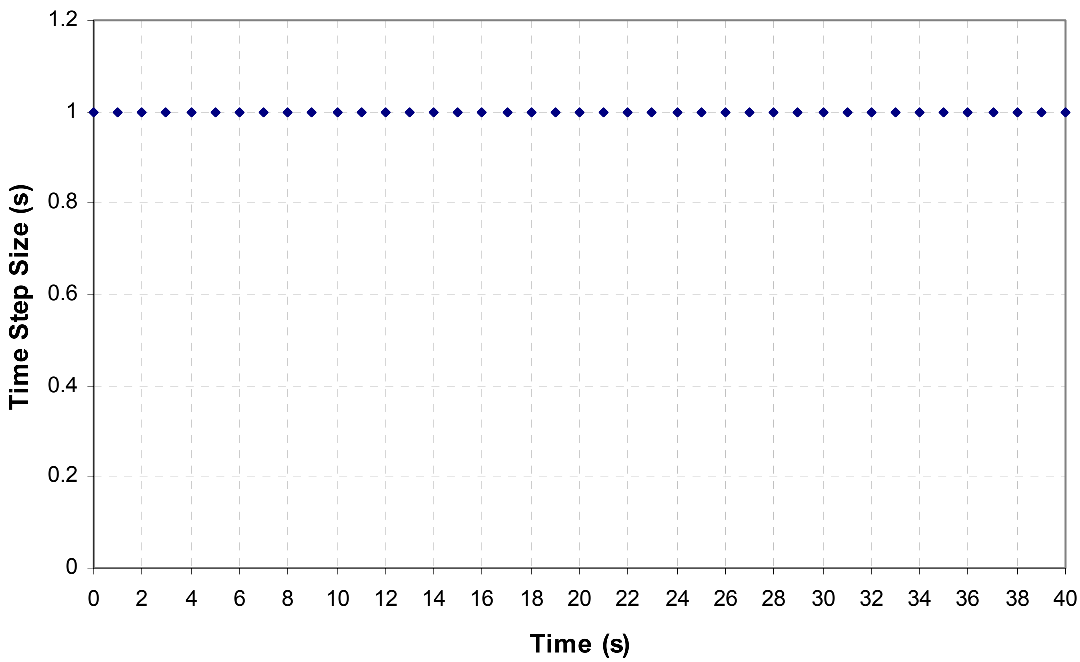

Figure 4.21 Time Step Size for Test Case 2

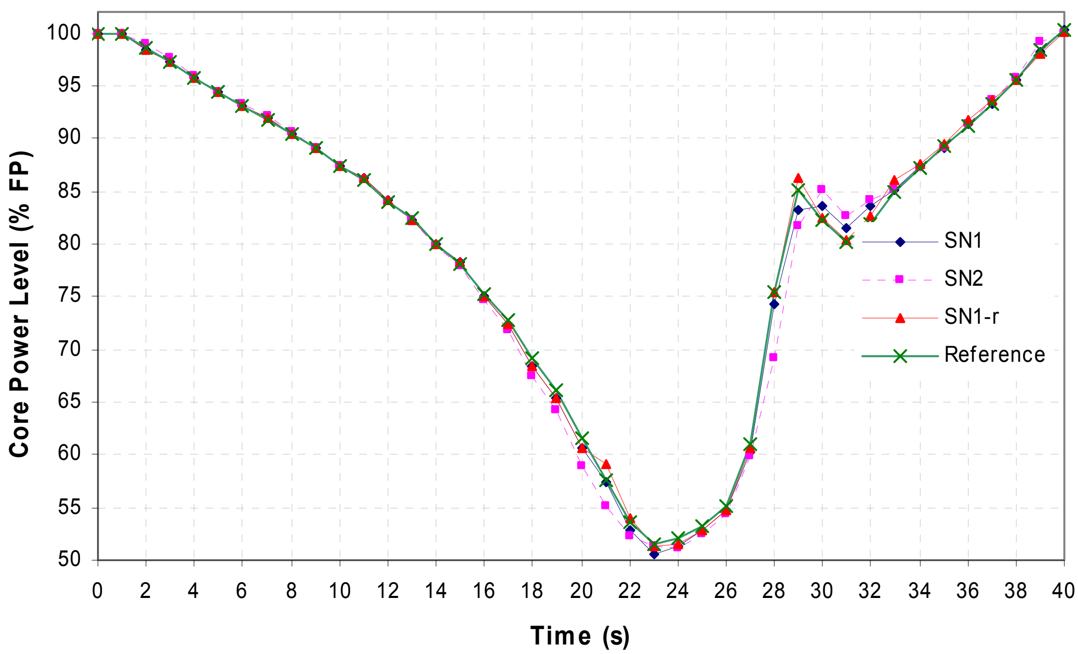

Figure 4.22 Core Power Level for Test Case 2

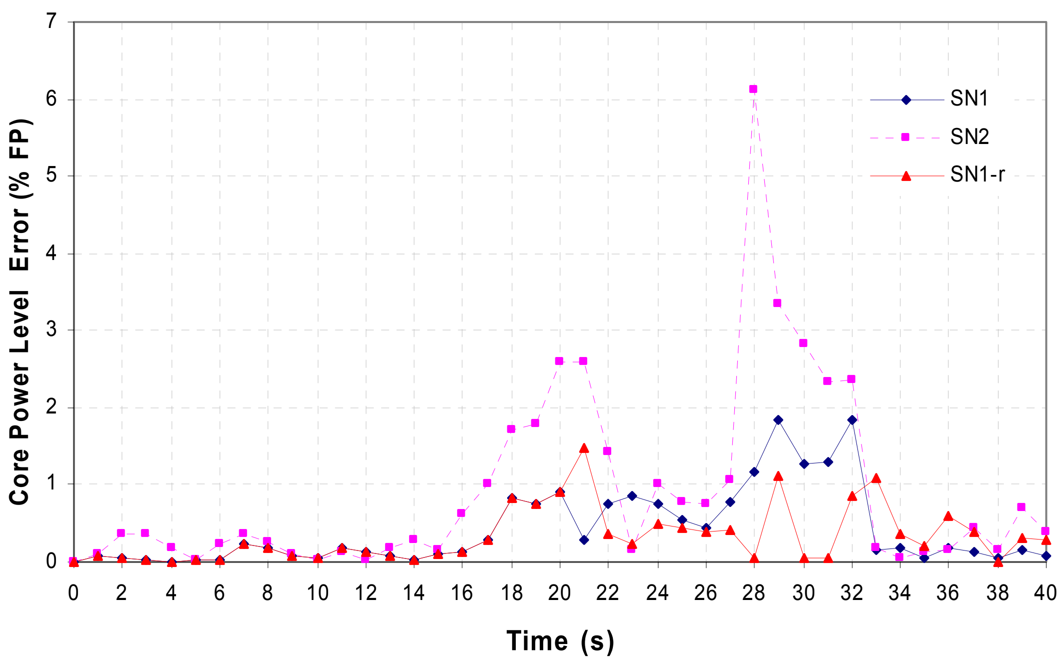

Figure 4.23 Core Power Level Error for Test Case 2

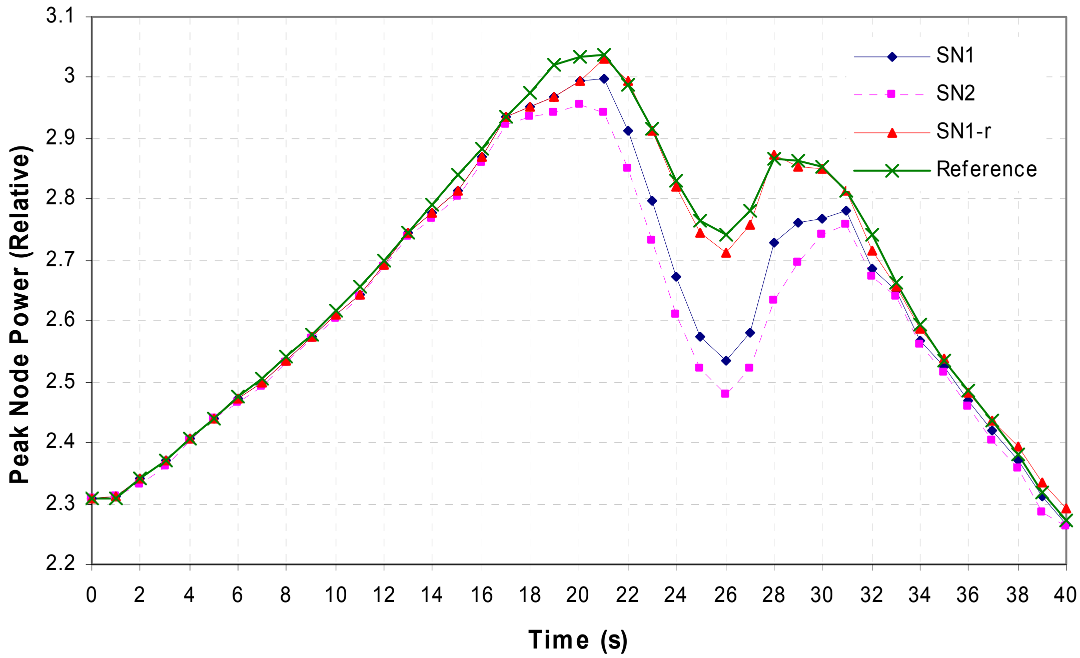

Figure 4.24 Relative Peak Node Power for Test Case 2

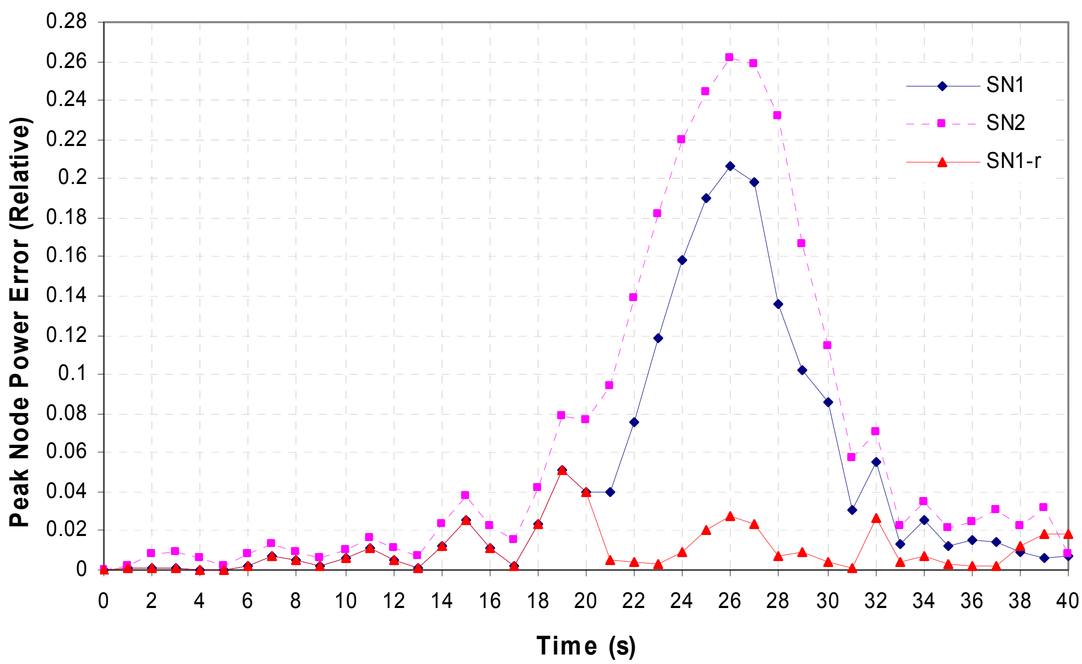

Figure 4.25 Relative Peak Node Power Error for Test Case 2

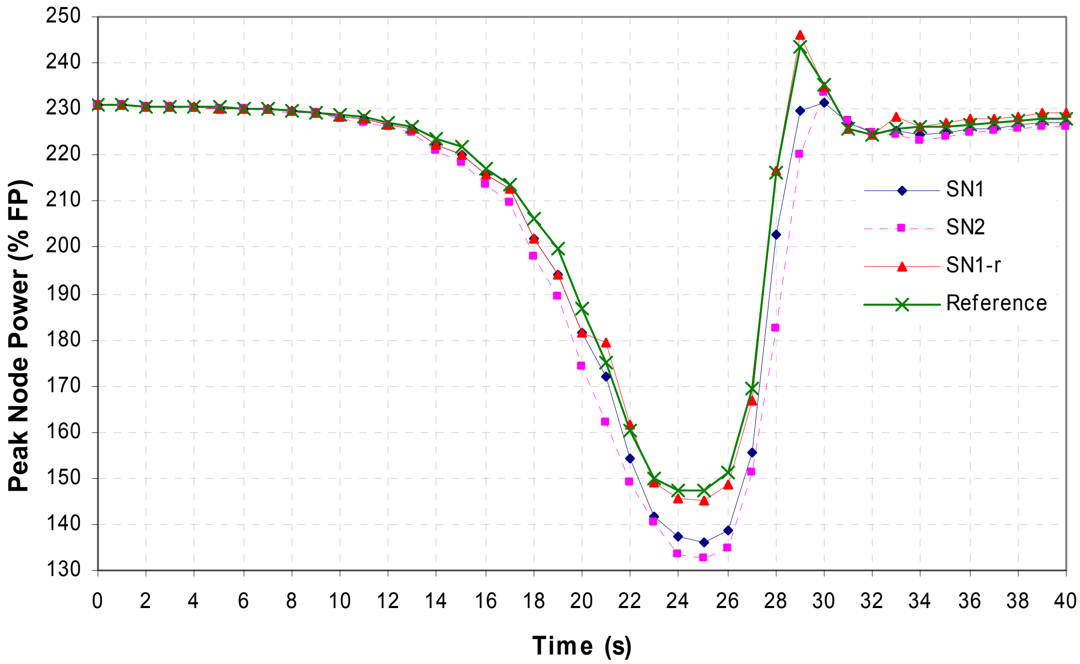

Figure 4.26 Peak Node Power for Test Case 2

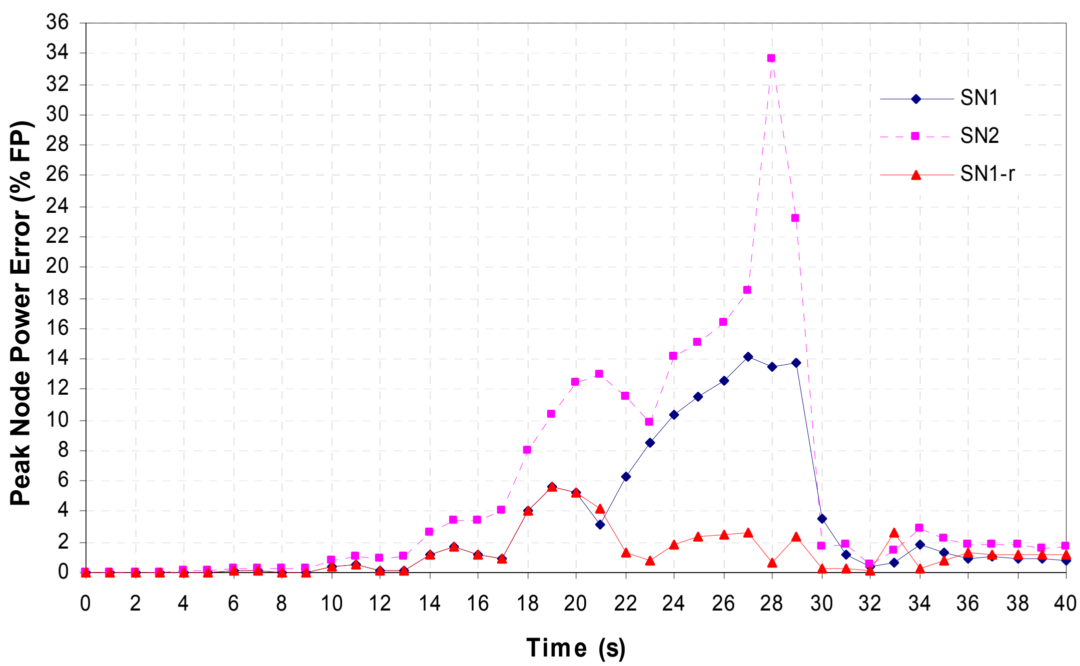

Figure 4.27 Peak Node Power Error for Test Case 2

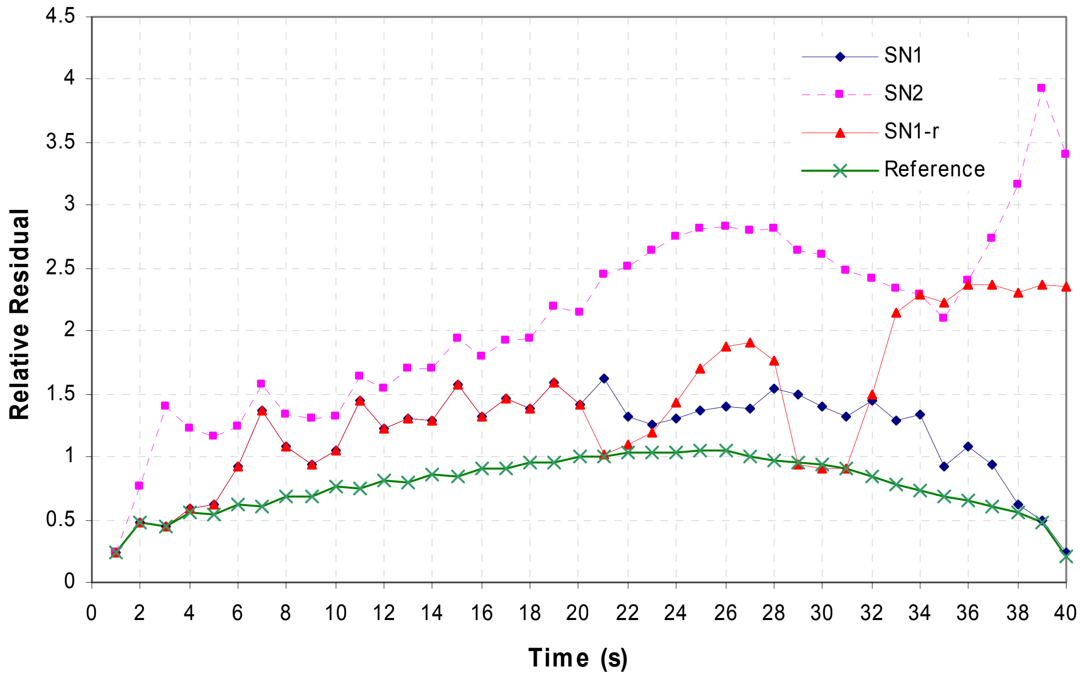

Figure 4.28 Relative Residual for Test Case 2

Table 4-1 Axial Power Map for Test Case 2

Axial Location (in)	**12**	**36**	**60**	**84**	**108**	**132**	**RMS**
Time=0 sec.							
Reference	***1.8348***	1.5238	0.9859	0.6877	0.5407	0.4270	
SN1 Error	***0.0001***	0.0000	-0.0001	0.0000	-0.0001	0.0000	7.07E-05
SN2 Error	***-0.0001***	0.0001	0.0000	0.0000	0.0000	-0.0001	7.07E-05
SN1-r Error	***0.0001***	0.0000	-0.0001	0.0000	-0.0001	0.0000	7.07E-05
Time=26 sec.							
Reference	1.5351	1.3721	0.9903	0.7842	0.7064	0.6119	
SN1 Error	***0.0975***	**0.1234**	-0.0205	-0.0672	-0.0715	-0.0617	8.02E-02
SN2 Error	***0.1534***	**0.1572**	-0.0235	-0.0894	-0.1064	-0.0912	1.13E-01
SN1-r Error	***0.0177***	**0.0272**	0.0200	-0.0174	-0.0264	-0.0211	2.20E-02
Time=40 sec.							
Reference	1.8060	1.5039	0.9791	0.6934	0.5617	0.4558	
SN1 Error	***0.0067***	0.0063	-0.0022	-0.0045	-0.0027	-0.0036	4.65E-03
SN2 Error	***0.0070***	**0.0072**	-0.0049	-0.0057	-0.0040	0.0004	5.38E-03
SN1-r Error	***0.0098***	0.0067	0.002	-0.0081	0.0015	-0.0120	7.71E-03

bold denotes the maximum error
italic denotes the error at the maximum peak power

Table 4-2 Radial Relative Power Distribution for Test Case 2 at Time=0 sec.

Y|X	1	2	3	4	5	6	7	8
1	1.0745	***1.1192***	1.0532	1.0956	1.0497	1.1159	0.9885	0.8018
	0.0000	***-0.0001***	-0.0001	0.0000	0.0000	-0.0001	0.0000	0.0000
	0.0000	***0.0001***	0.0000	0.0000	0.0000	0.0000	0.0000	-0.0001
	0.0000	***-0.0001***	-0.0001	0.0000	0.0000	-0.0001	0.0000	0.0000
2	1.1192	1.0903	1.1102	1.0460	1.1118	1.0478	1.0481	0.6716
	0.0000	0.0000	0.0000	0.0000	0.0000	0.0000	0.0000	0.0000
	0.0001	0.0000	0.0000	0.0000	0.0001	0.0000	0.0000	-0.0001
	0.0000	0.0000	0.0000	0.0000	0.0000	0.0000	0.0000	0.0000
3	1.0533	1.1102	1.0479	1.1101	1.0600	1.0804	0.9259	
	0.0000	0.0000	0.0000	-0.0001	0.0000	0.0000	0.0000	
	0.0001	0.0000	0.0000	0.0000	0.0000	0.0000	-0.0001	
	0.0000	0.0000	0.0000	-0.0001	0.0000	0.0000	0.0000	
4	1.0957	1.0461	1.1102	1.0558	1.0943	1.0509	0.6948	
	0.0000	0.0000	0.0000	0.0000	0.0000	0.0000	0.0000	
	0.0001	0.0000	0.0000	0.0000	0.0000	0.0000	-0.0001	
	0.0000	0.0000	0.0000	0.0000	0.0000	0.0000	0.0000	
5	1.0498	1.1118	1.0601	1.0944	0.9397	0.7581		**Ref.**
	0.0000	0.0000	0.0000	0.0000	0.0000	0.0000		**SN1 Err**
	0.0001	0.0000	0.0001	0.0000	0.0000	0.0000		**SN2 Err**
	0.0000	0.0000	0.0000	0.0000	0.0000	0.0000		**SN1-r Err**
6	1.1161	1.0479	1.0805	1.0509	0.7581			
	0.0000	0.0000	0.0000	0.0000	0.0000			
	0.0000	0.0000	0.0000	-0.0001	0.0000			
	0.0000	0.0000	0.0000	0.0000	0.0000			
7	0.9886	1.0482	0.9260	0.6949				**RMS**
	0.0000	0.0000	0.0000	0.0000				**2.9175E-5**
	0.0000	0.0000	0.0000	0.0000				**4.8372E-5**
	0.0000	0.0000	0.0000	0.0000				**2.9171E-5**
8	0.8019	0.6717						
	0.0000	0.0000						
	0.0000	0.0000						
	0.0000	0.0000						

bold denotes the maximum error

italic denotes the error at the maximum peak power

Table 4-3 Radial Relative Power Distribution for Test Case 2 at Time=26 sec.

Y|X	1	2	3	4	5	6	7	8
1	1.3575	***1.3989***	1.2643	1.2064	0.9784	0.8476	0.7802	0.6645
	0.0042	***0.0055***	0.0026	0.0023	0.0004	0.0002	**-0.0046**	-0.0079
	-0.0203	***-0.0194***	-0.0151	-0.0079	0.0034	0.0152	0.0137	0.0084
	-0.0013	***-0.0014***	-0.0008	-0.0006	0.0000	0.0005	0.0007	0.0009
2	1.3989	1.3493	1.3272	1.1569	1.0391	0.6773	0.8262	0.5568
	0.0055	0.0045	0.0043	0.0015	0.002	-0.0012	-0.0035	-0.0045
	-0.0193	-0.0177	-0.0144	-0.0078	0.0034	0.0155	0.0142	0.0102
	-0.0014	-0.0013	-0.001	-0.0004	-0.0001	0.0008	0.0007	0.0008
3	1.2643	1.3272	1.2278	1.2424	1.0814	0.9798	0.8227	
	0.0026	0.0043	0.0021	0.0031	0.0005	-0.0004	-0.0025	
	-0.015	-0.0144	-0.0122	-0.0077	-0.0011	0.0062	0.0082	
	-0.0009	-0.001	-0.0006	-0.0005	-0.0001	0.0003	0.0005	
4	1.2065	1.157	1.2424	1.1785	1.1875	1.0902	0.6844	
	0.0024	0.0015	0.0031	0.0008	0.0005	-0.0005	0.0002	
	-0.0077	-0.0076	-0.0076	-0.0072	-0.0049	-0.0007	0.0036	
	-0.0006	-0.0004	-0.0006	-0.0002	-0.0002	0.0001	0.0004	
5	0.9785	1.0392	1.0815	1.1876	1.0324	0.8176		**Ref.**
	0.0004	0.002	0.0006	0.0005	-0.0033	-0.0012		**SN1 Err**
	0.0038	0.0038	-0.0009	-0.0047	-0.0077	-0.0033		**SN2 Err**
	0.0000	-0.0001	-0.0001	-0.0001	0.0002	0.0004		**SN1-r Err**
6	0.8476	0.6773	0.9798	1.0902	0.8176			
	0.0001	-0.0013	-0.0005	-0.0006	-0.0013			
	0.0158	0.0159	0.0066	-0.0005	-0.0032			
	0.0003	0.0007	0.0001	0.0000	0.0004			
7	0.7803	0.8263	0.8227	0.6845				**RMS**
	-0.0046	-0.0035	-0.0026	0.0002				**3.1316E-3**
	0.0149	0.0155	0.0089	0.0040				**1.0907E-2**
	0.0006	0.0007	0.0004	0.0005				**6.5330E-4**
8	0.6646	0.5568						
	-0.0078	-0.0046						
	0.0102	0.0122						
	0.0008	0.0007						

bold denotes the maximum error

italic denotes the error at the maximum peak power

Table 4-4 Radial Relative Power Distribution for Test Case 2 at Time=40 sec.

Y|X	**1**	**2**	**3**	**4**	**5**	**6**	**7**	**8**	
1	1.0760	***1.1208***	1.0543	1.0963	1.0496	1.1155	0.9874	0.8003	
	0.0004	***0.0005***	0.0003	0.0002	0.0000	0.0000	-0.0005	**-0.0008**	
	-0.0002	***-0.0002***	-0.0002	-0.0001	-0.0001	0.0001	0.0000	0.0000	
	-0.0025	***-0.0023***	-0.0010	0.0003	0.0012	0.0016	0.0004	0.0002	
2	1.1208	1.0917	1.1113	1.0465	1.1119	1.0474	1.0472	0.6702	
	0.0004	0.0004	0.0004	0.0001	0.0002	-0.0005	-0.0004	-0.0005	
	-0.0002	-0.0001	-0.0001	-0.0002	-0.0001	-0.0002	0.0000	**0.0015**	
	-0.0024	-0.0018	-0.001	0.0002	0.0011	0.0011	-0.0007	0.0000	
3	1.0543	1.1114	1.0487	1.1108	1.0601	1.0803	0.9251		
	0.0003	0.0005	0.0002	0.0003	0.0001	-0.0001	-0.0003		
	-0.0002	-0.0001	-0.0001	-0.0001	-0.0002	-0.0001	-0.0001		
	-0.0011	-0.0010	-0.0003	0.0003	0.0004	-0.0006	-0.0001		
4	1.0963	1.0466	1.1108	1.0562	1.0947	1.0509	0.6942		
	0.0002	0.0002	0.0003	0.0002	0.0001	0.0000	0.0001		
	-0.0001	-0.0001	-0.0001	-0.0001	-0.0002	-0.0001	0.0000		
	0.0001	0.0002	0.0003	0.0004	0.0004	0.0003	0.0001		
5	1.0497	1.112	1.0602	1.0947	0.9397	0.7577			**Ref.**
	0.0001	0.0002	0.0001	0.0001	-0.0002	-0.0001			**SN1 Err**
	0.0000	0.0000	-0.0001	-0.0002	-0.0004	-0.0002			**SN2 Err**
	0.0011	0.001	0.0004	0.0004	-0.0004	0.0001			**SN1-r Err**
6	1.1156	1.0475	1.0804	1.051	0.7578				
	0.0000	-0.0005	0.0000	0.0001	0.0000				
	0.0002	-0.0001	0.0000	0.0000	-0.0001				
	0.0014	0.0009	-0.0007	0.0003	0.0001				
7	0.9875	1.0473	0.9252	0.6942					**RMS.**
	-0.0005	-0.0004	-0.0002	0.0000					**3.3101E-4**
	0.0002	0.0002	0.0001	0.0000					**3.0106E-4**
	0.0002	-0.0009	-0.0002	0.0000					**9.2519E-4**
8	0.8004	0.6703							
	-0.0008	-0.0005							
	0.0003	0.0015							
	0.0001	-0.0001							

bold denotes the maximum error
italic denotes the error at the maximum peak power

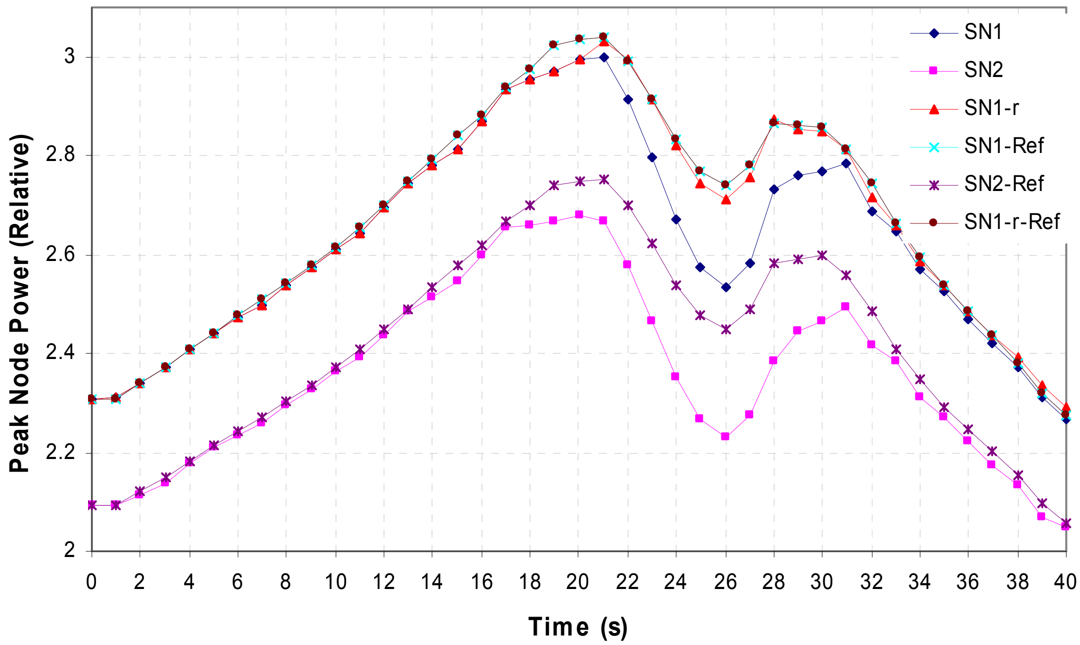

Figure 4.29 **Coarse Mesh Relative Peak Node Power for Test Case 2 "Fine Mesh Determined Peak Node Location"**

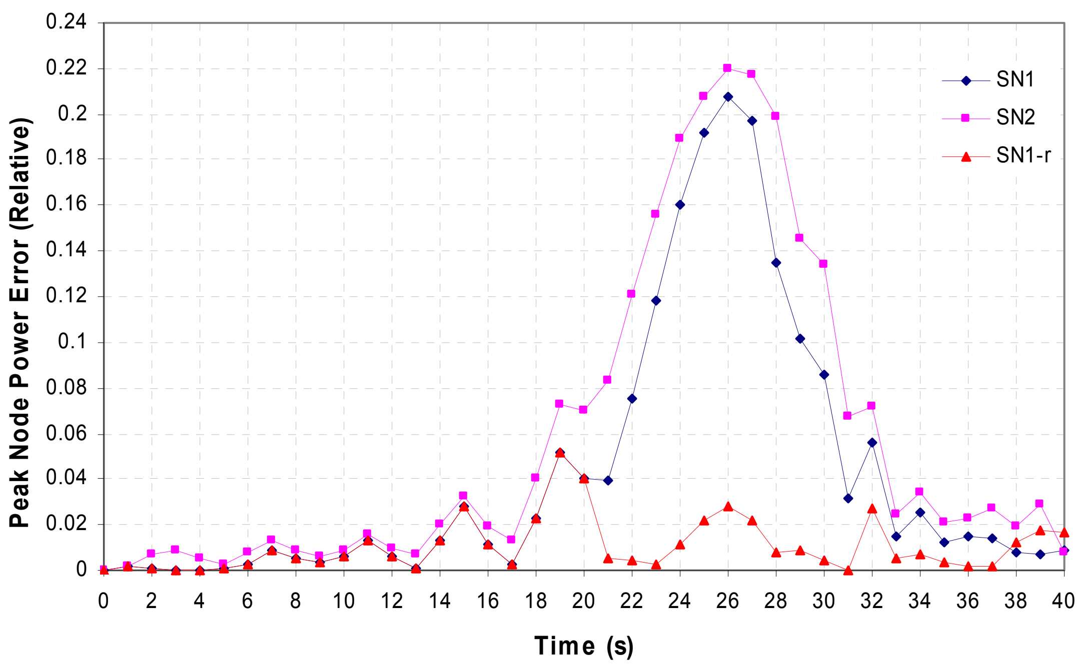

Figure 4.30 **Coarse Mesh Relative Peak Node Power Error for Test Case 2 "Fine Mesh Determined Peak Node Location"**

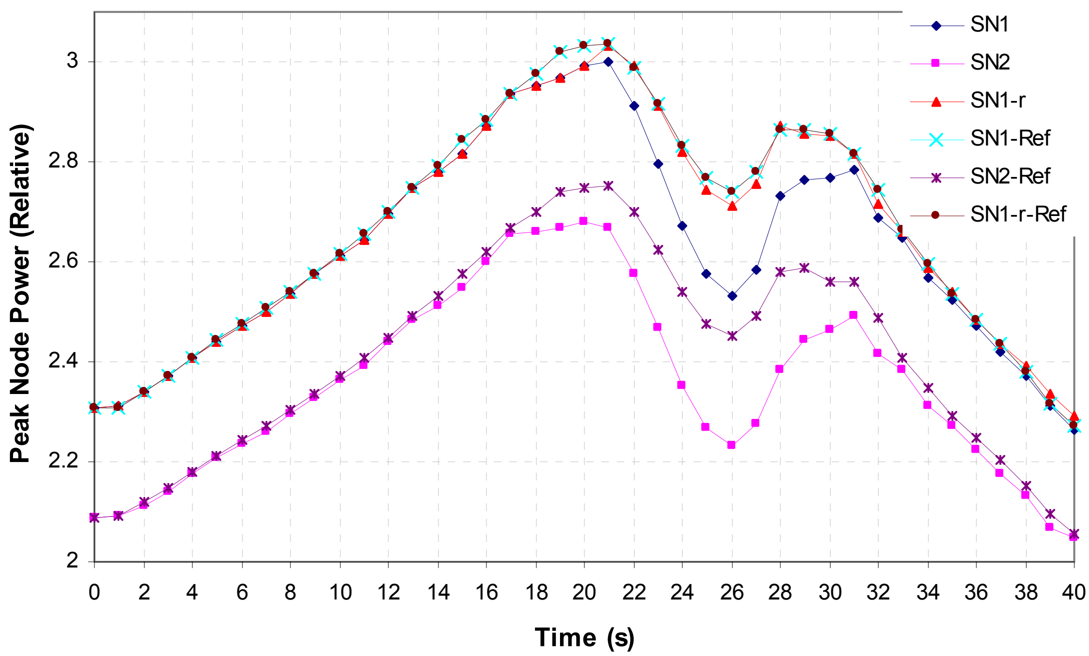

Figure 4.31 Coarse Mesh Relative Peak Node Power for Test Case 2 "Coarse Mesh Determined Peak Node Location"

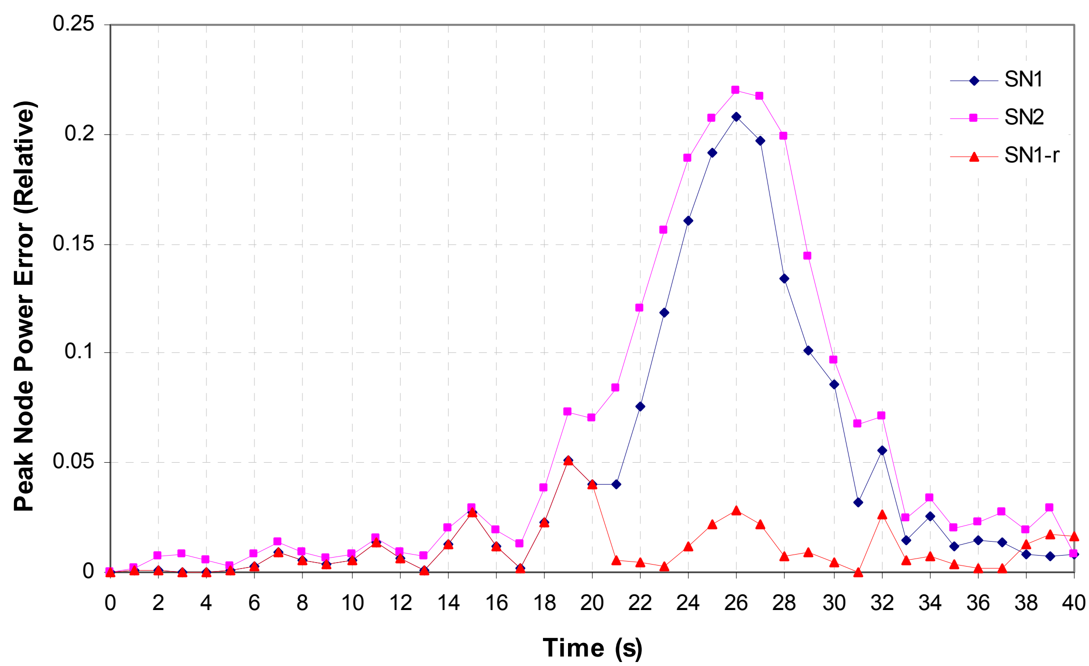

Figure 4.32 Coarse Mesh Relative Peak Node Power Error for Test Case 2 "Coarse Mesh Determined Peak Node Location"

Table 4-5 CPU Time Comparison for Test Case 2

	Reference	SN1	SN2	SN1-r
CPU Time In Steady State Collapsing	0.0	1.27	1.04	1.27
CPU Time In Transient Collapsing (average)	0.0	0.0	0.0	1.31
CPU Time In Refine Steps (fine+coarse)	0.0	0.0	0.0	42.85
Total Number Outer Iteration	987	999	1315	1173
Total Code CPU Time	211.37	137.70	128.73	170.15

4.2.4 Test Case 3: Rod Ejection Accident

This accident is defined as the mechanical failure of a control rod mechanism pressure housing resulting in the ejection of a control rod assembly and drive shaft. The consequence of this mechanical failure is a rapid positive reactivity insertion together with an adverse core power distribution, possibly leading to localized fuel damage [35]. In Final Safety Analysis Reports (FSAR) this accident is analyzed for four different initial states of the reactor, explicitly BOC full power, BOC zero power, End of Cycle (EOC) full power and EOC zero power. The BOC full power state is selected for modeling as Test Case 3 in this research. For a realistic accident analysis, the core model is created with the help of the 2001 McGuire Updated Final Safety Analysis Report (UFSAR) [35] as follows:

1. A full core geometry model of the Westinghouse PWR core as depicted in Figure 4.33 is created from the quarter core symmetry model depicted in Figure 4.5.
2. For all control rods out, the critical boron concentration is calculated.
3. At the critical reactivity condition, the insertion position of bank D which gives $0.5\ \%\ \Delta\rho$ ($k \approx 0.995$) is calculated.
4. Bank D is inserted to this insertion position and a new critical boron concentration is calculated.
5. With the reactor critical with bank D at this insertion position, a control rod assembly in bank D is ejected in 0.06 seconds.

The transient analysis of the core is started after Step 4. Following the control rod ejection, all control rods are inserted at 0.56 sec. as stated in the FSAR. Again for a realistic analysis, the control rod insertion curve is modeled as shown in Figure 4.34.

This accident is again analyzed for SN1 and SN2 nodalizations. Three similar collapsing schemes are used as in Test Case 1. For the first two schemes the core is collapsed axially at *t=0* second using either SN1 or SN2 nodalizations. The third case, denoted as SN-r in the figures, after initially collapsing at 0 sec the axial nodalization is refined at 0.02 sec. and collapsed at 0.08 sec, refined at 1.56 second and collapsed at 1.7 sec, and finally refined at 2.25 sec. and collapsed at 2.45 sec. These refine and collapse steps are selected to minimize the error throughout the transient. Since bank D is partially inserted at *t=0* sec., the "rod-cusping" treatment is not used for this test case.

As shown in Figure 4.36 the core power level starts to decrease after 0.08 seconds because of the thermal-hydraulic feedback following the initial burst in the reactor core power with the rod ejection. Until the control rod insertion at 0.56 second all three collapsing schemes demonstrate good agreement. The effect of control rod insertion is seen after 0.65 second with an increased drop in the core power level and a strong rod-cusping effect noted for all three collapsing schemes. The peak node power error also is significant for the SN1 and SN2 schemes as shown in Figure 4.39 and Figure 4.41. However, a refining step at 0.02 sec. corrects the large error in the peak node power as the SN1-r scheme verifies. The large improvement in the error level shows that the initial flux form factors (FF) calculated at t=0 second are not applicable with the initiation of the rod ejection right after the collapsing. The second collapsing at t=0.08 gives a better estimate of the form factors which helps the SN1-r scheme to follow the fine mesh solution with a better accuracy.

Figure 4.36 through Figure 4.42 shows core power level, peak node power and related errors for the three collapsing schemes. The axial and radial core power errors presented in Table 4-6 to Table 4-9 are also consistent with the core and peak node power level errors. The SN1-r has the smallest RMS error, while the SN1 scheme performs better than the SN2 scheme as expected.

Although the relative residual in Figure 4.42 does not reflect the error in the peak node power for the SN1 and SN2 schemes, the reduced error at 0.02 second and 1.56 second indicate the improvement in the results due to the refining steps for the SN1-r scheme. The relative power error does not decrease through the end of the transient as in Test Case 1 since beginning and end states of the reactor are quite different.

The coarse mesh peak node powers are also calculated and compared with the related collapsed fine mesh peak node powers for fine and coarse mesh determined peak node locations, as seen Figure 4.43 through Figure 4.46, respectively. Figure 4.44 and Figure 4.46 show that the errors in the peak node powers are decreased compared to the fine mesh peak node power errors, depicted in Figure 4.39. This behavior indicates that the flux form factor errors are significant for this test case. On the other hand, the increase in the SN1-r scheme errors and sharp peaks in the SN1 and SN2 scheme errors show that the Super-Nodal solution errors are also large. The large peak values in Figure 4.44 and Figure 4.46 appears when the peak node location shifts to the fuel reflector interface. Since the SN2 nodalization is expected to have larger errors at the fuel reflector interface due to the homogenization of fuel nodes at the interface, the SN2 scheme shows larger peaks in general. The largest peak appears at 1.56 sec in Figure 4.44 and Figure 4.46. The transverse integrated reference flux solution as seen in Figure 4.48 shows that the peak in the intra-nodal flux shape is increased at 1.56 sec. compared to 0 sec. as seen in Figure 4.47.

The CPU times given in Table 4-10 are consistent with the Test Case 2 results. While SN2 nodalization gives the best run time out of the three schemes, the refine steps in the SN1-r scheme decreases the CPU time savings obtained from SN1 nodalization.

0	0	0	0	0	0	0	0	0	0	0	0	2	2	2	2	2	2	2	2	2	2	2	2	0	0	0	0	0	0	0	0	0	0	0	0
0	0	0	0	0	0	0	0	0	0	0	0	2	2	2	2	2	2	2	2	2	2	2	2	0	0	0	0	0	0	0	0	0	0	0	0
0	0	0	0	0	0	0	0	2	2	2	2	2	2	1	1	1	1	1	1	1	1	2	2	2	2	2	2	0	0	0	0	0	0	0	0
0	0	0	0	0	0	0	0	2	2	2	2	2	2	1	7	7	7	7	7	7	1	2	2	2	2	2	2	0	0	0	0	0	0	0	0
0	0	0	0	0	0	2	2	2	2	1	1	1	1	1	7	7	7	7	7	7	1	1	1	1	1	2	2	2	2	0	0	0	0	0	0
0	0	0	0	0	0	2	2	2	2	1	7	7	G	G	9	9	D	D	9	9	G	G	7	7	1	2	2	2	2	0	0	0	0	0	0
0	0	0	0	2	2	2	2	1	1	1	7	7	G	G	9	9	D	D	9	9	G	G	7	7	1	1	1	2	2	2	2	0	0	0	0
0	0	0	0	2	2	2	2	1	7	7	C	C	5	5	F	F	4	4	F	F	5	5	C	C	7	7	1	2	2	2	2	0	0	0	0
0	0	2	2	2	2	1	1	1	7	7	C	C	5	5	F	F	4	4	F	F	5	5	C	C	7	7	1	1	1	2	2	2	2	0	0
0	0	2	2	2	2	1	7	7	3	3	5	5	H	H	5	5	3	3	5	5	H	H	5	5	3	3	7	7	1	2	2	2	2	0	0
0	0	2	2	1	1	1	7	7	3	3	5	5	H	H	5	5	3	3	5	5	H	H	5	5	3	3	7	7	1	1	1	2	2	0	0
0	0	2	2	1	7	7	C	C	5	5	A	A	5	5	3	3	6	6	3	3	5	5	A	A	5	5	C	C	7	7	1	2	2	0	0
2	2	2	2	1	7	7	C	C	5	5	A	A	5	5	3	3	6	6	3	3	5	5	A	A	5	5	C	C	7	7	1	2	2	2	2
2	2	2	2	1	G	G	5	5	H	H	5	5	E	E	5	5	B	B	5	5	E	E	5	5	H	H	5	5	G	G	1	2	2	2	2
2	2	1	1	1	G	G	5	5	H	H	5	5	E	E	5	5	B	B	5	5	E	E	5	5	H	H	5	5	G	G	1	1	1	2	2
2	2	1	7	7	9	9	F	F	5	5	3	3	5	5	3	3	6	6	3	3	5	5	3	3	5	5	F	F	9	9	7	7	1	2	2
2	2	1	7	7	9	9	F	F	5	5	3	3	5	5	3	3	6	6	3	3	5	5	3	3	5	5	F	F	9	9	7	7	1	2	2
2	2	1	7	7	D	D	4	4	3	3	6	6	B	B	6	6	3	3	6	6	B	B	6	6	3	3	4	4	D	D	7	7	1	2	2
2	2	1	7	7	D	D	4	4	3	3	6	6	B	B	6	6	3	3	6	6	B	B	6	6	3	3	4	4	D	D	7	7	1	2	2
2	2	1	7	7	9	9	F	F	5	5	3	3	5	5	3	3	6	6	3	3	5	5	3	3	5	5	F	F	9	9	7	7	1	2	2
2	2	1	7	7	9	9	F	F	5	5	3	3	5	5	3	3	6	6	3	3	5	5	3	3	5	5	F	F	9	9	7	7	1	2	2
2	2	1	1	1	G	G	5	5	H	H	5	5	E	E	5	5	B	B	5	5	E	E	5	5	H	H	5	5	G	G	1	1	1	2	2
2	2	2	2	1	G	G	5	5	H	H	5	5	E	E	5	5	B	B	5	5	E	E	5	5	H	H	5	5	G	G	1	2	2	2	2
2	2	2	2	1	7	7	C	C	5	5	A	A	5	5	3	3	6	6	3	3	5	5	A	A	5	5	C	C	7	7	1	2	2	2	2
0	0	2	2	1	7	7	C	C	5	5	A	A	5	5	3	3	6	6	3	3	5	5	A	A	5	5	C	C	7	7	1	2	2	0	0
0	0	2	2	1	1	1	7	7	3	3	5	5	H	H	5	5	3	3	5	5	H	H	5	5	3	3	7	7	1	1	1	2	2	0	0
0	0	2	2	2	2	1	7	7	3	3	5	5	H	H	5	5	3	3	5	5	H	H	5	5	3	3	7	7	1	2	2	2	2	0	0
0	0	2	2	2	2	1	1	1	7	7	C	C	5	5	F	F	4	4	F	F	5	5	C	C	7	7	1	1	1	2	2	2	2	0	0
0	0	0	0	2	2	2	2	1	7	7	C	C	5	5	F	F	4	4	F	F	5	5	C	C	7	7	1	2	2	2	2	0	0	0	0
0	0	0	0	2	2	2	2	1	1	1	7	7	G	G	9	9	D	D	9	9	G	G	7	7	1	1	1	2	2	2	2	0	0	0	0
0	0	0	0	0	0	2	2	2	2	1	7	7	G	G	9	9	D	D	9	9	G	G	7	7	1	2	2	2	2	0	0	0	0	0	0
0	0	0	0	0	0	2	2	2	2	1	1	1	1	1	7	7	7	7	7	7	1	1	1	1	1	2	2	2	2	0	0	0	0	0	0
0	0	0	0	0	0	0	0	2	2	2	2	2	2	1	7	7	7	7	7	7	1	2	2	2	2	2	2	0	0	0	0	0	0	0	0
0	0	0	0	0	0	0	0	2	2	2	2	2	2	1	1	1	1	1	1	1	1	2	2	2	2	2	2	0	0	0	0	0	0	0	0
0	0	0	0	0	0	0	0	0	0	0	0	2	2	2	2	2	2	2	2	2	2	2	2	0	0	0	0	0	0	0	0	0	0	0	0
0	0	0	0	0	0	0	0	0	0	0	0	2	2	2	2	2	2	2	2	2	2	2	2	0	0	0	0	0	0	0	0	0	0	0	0

Legend:

D	Ejected or Stuck Control Rod Assembly
D	D Control Rod Bank
1	Reflector
2	Water

Figure 4.33 Full Core Fuel Map for Test Case 3 and Test Case 4

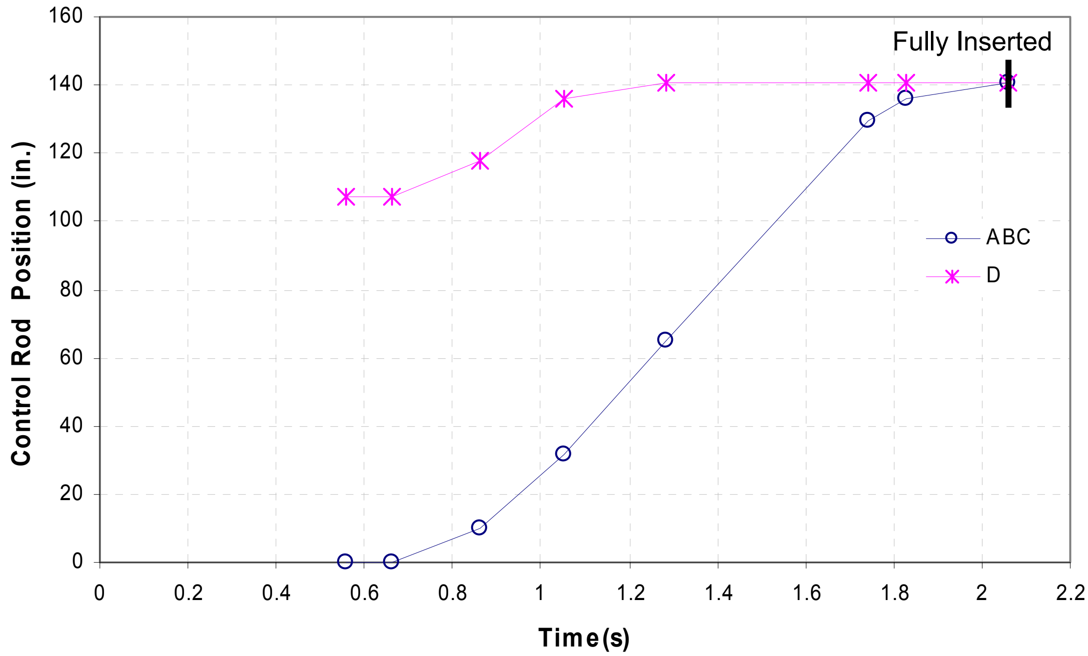

Figure 4.34 Control Rod Insertion Curve for Test Case 3

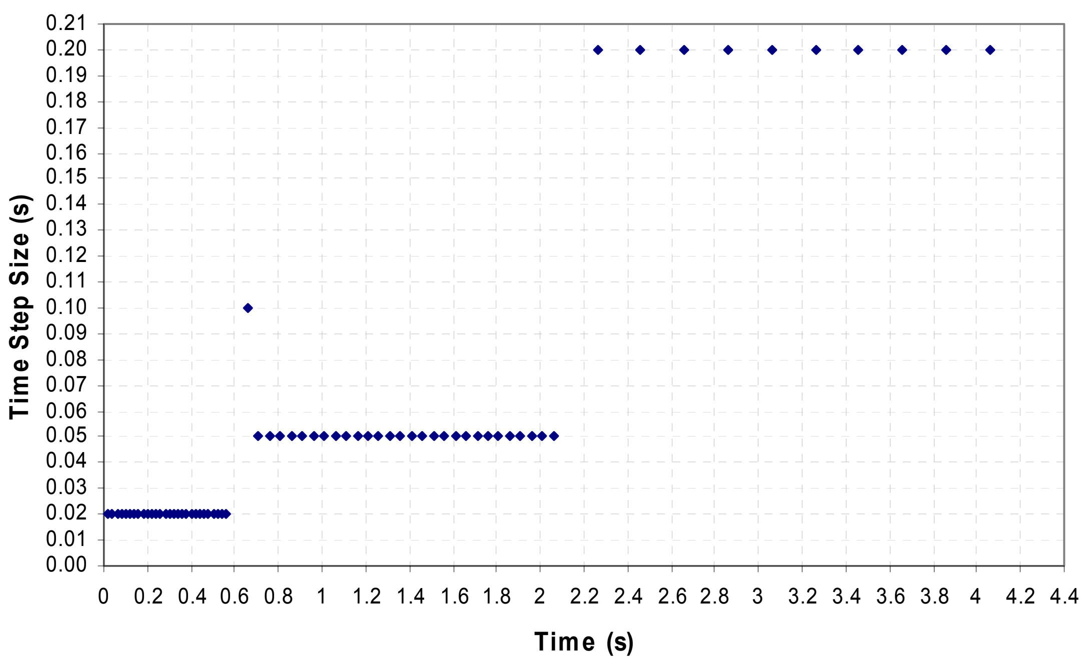

Figure 4.35 Time Step Size for Test Case 3

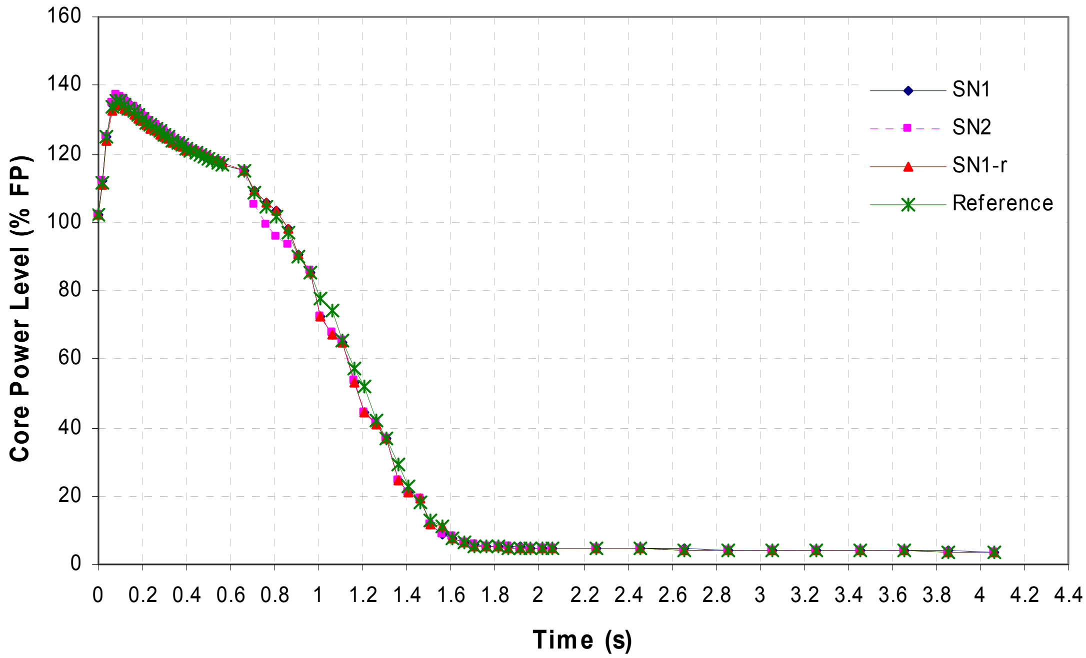

Figure 4.36 Core Power Level for Test Case 3

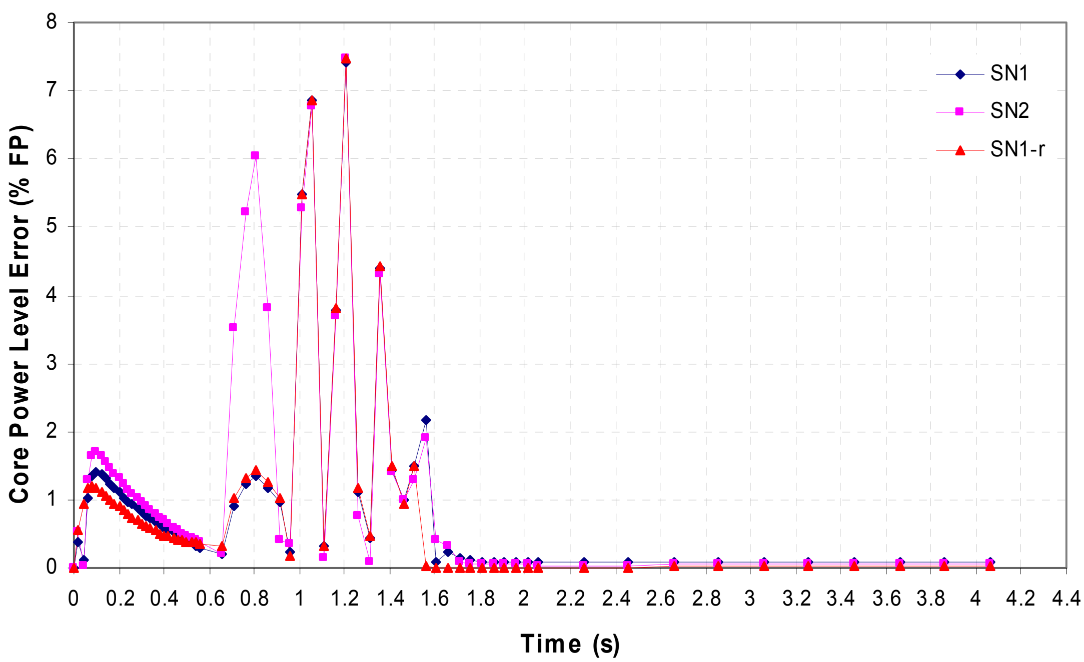

Figure 4.37 Core Power Level Error for Test Case 3

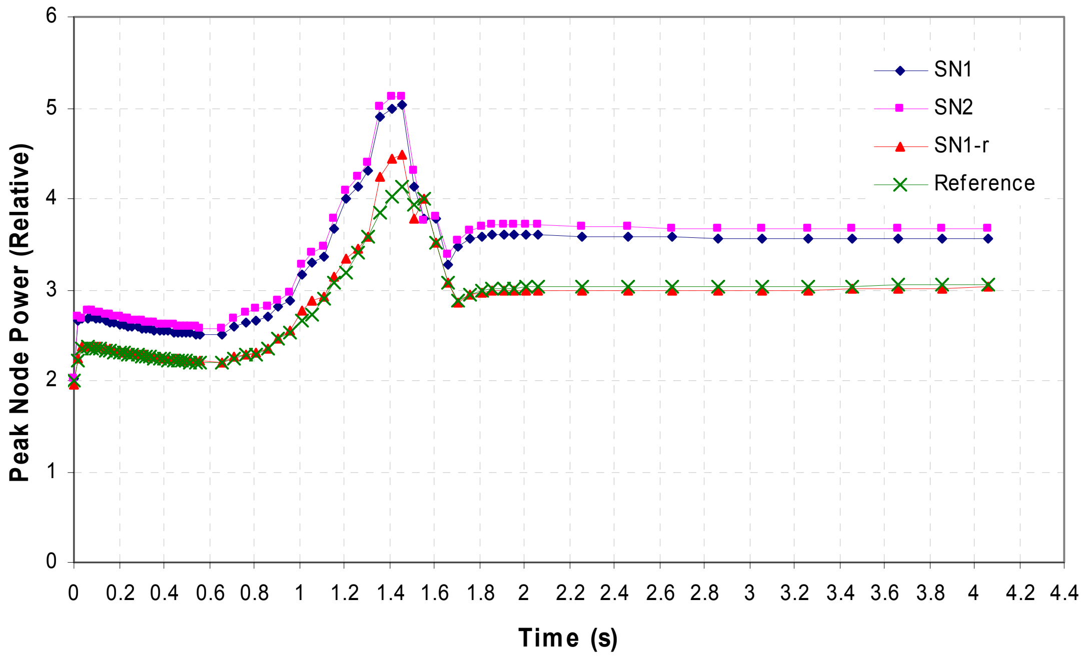

Figure 4.38 Relative Peak Node Power for Test Case 3

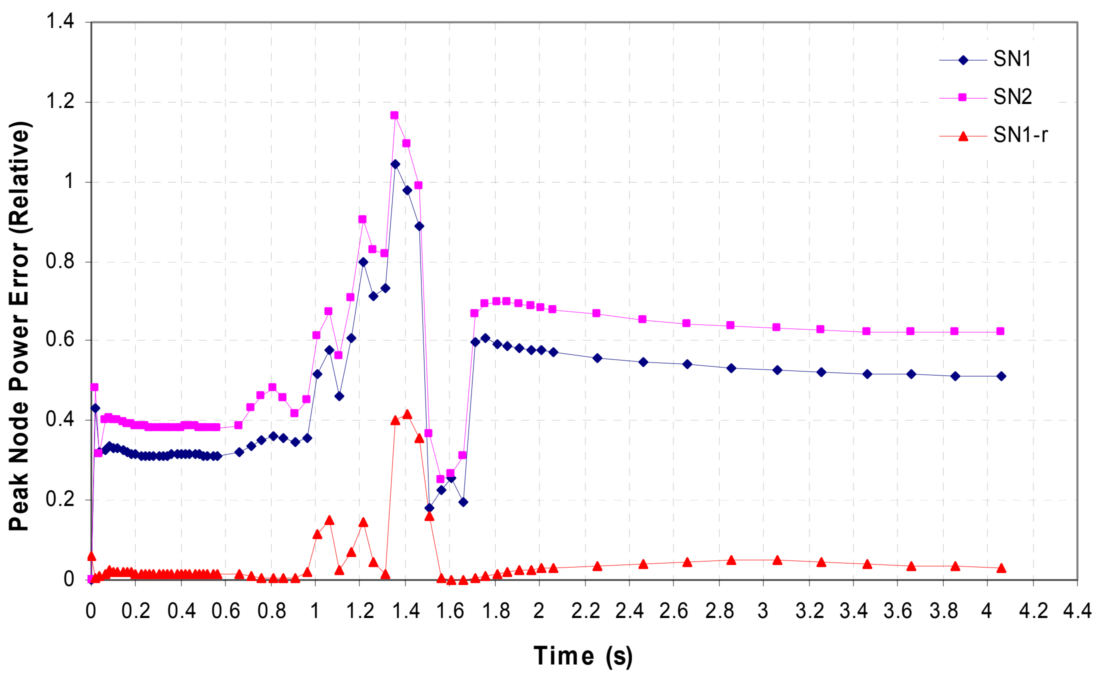

Figure 4.39 Relative Peak Node Power Error for Test Case 3

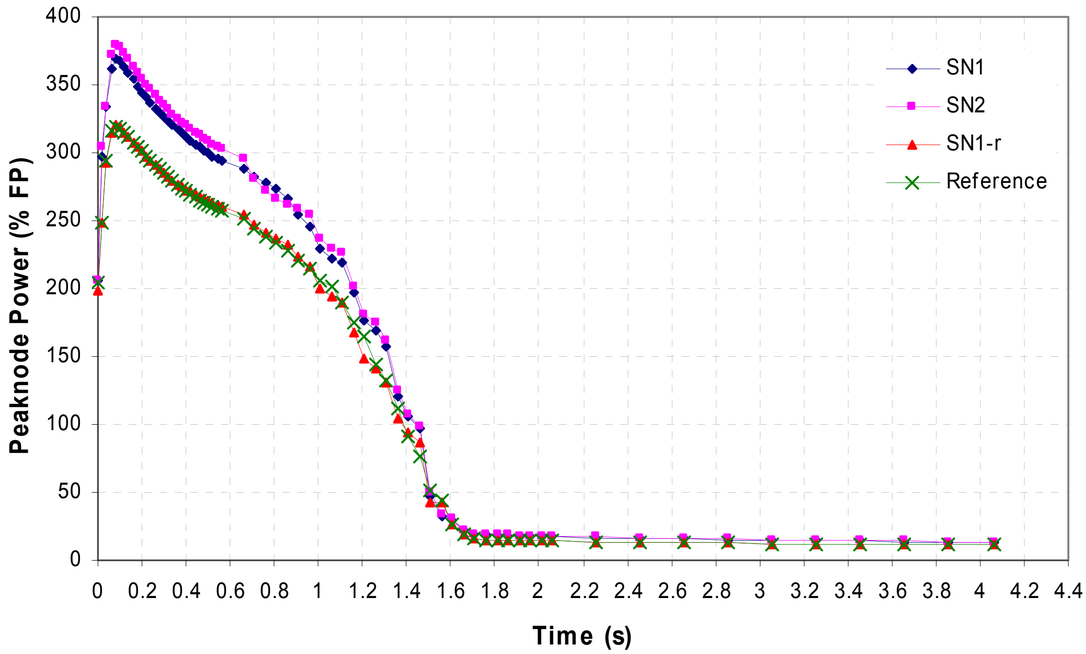

Figure 4.40 Peak Node Power for Test Case 3

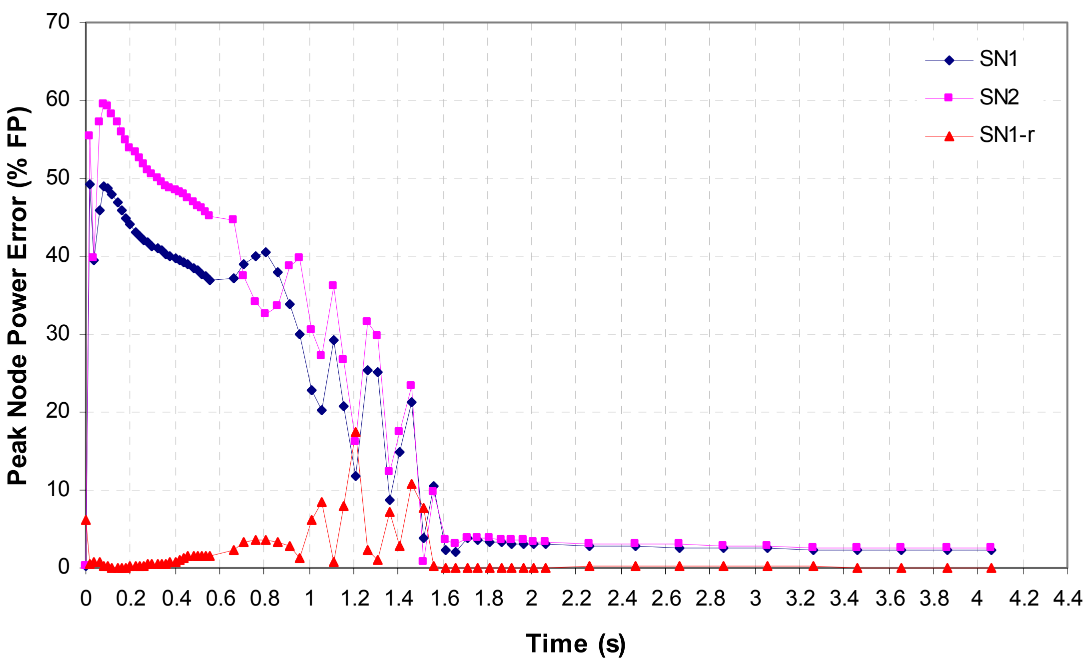

Figure 4.41 Peak Node Power Error for Test Case 3

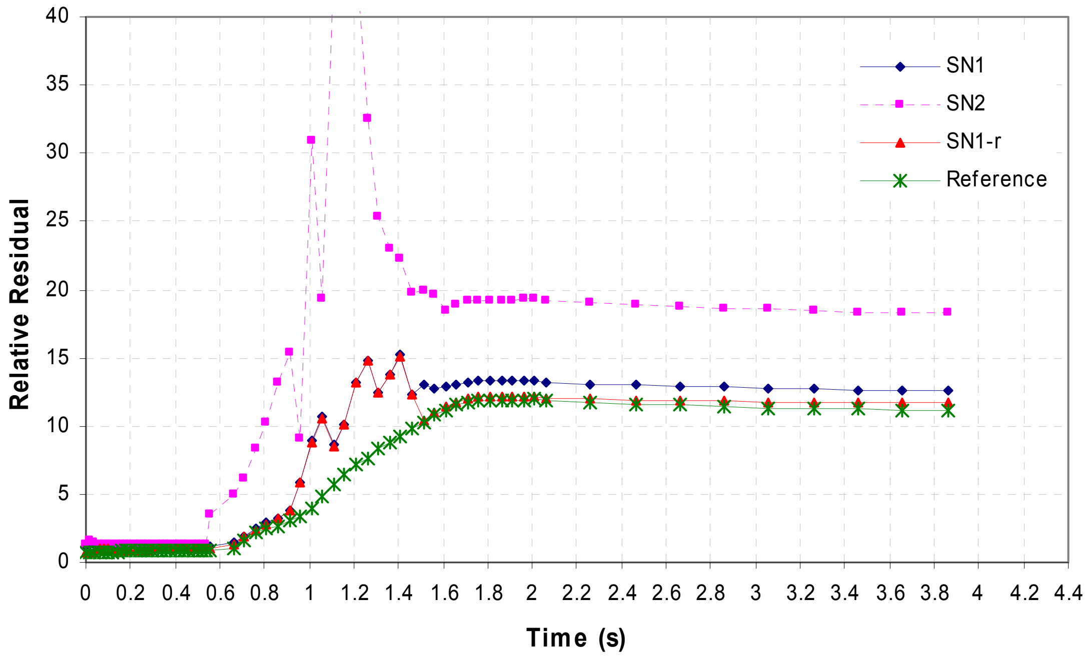

Figure 4.42 Relative Residual for Test Case 3

Table 4-6 Axial Power Map for Test Case 3

Axial Location (in)	**12**	**36**	**60**	**84**	**108**	**132**	**RMS**
Time=0.8 sec.							
Reference	0.8423	***1.4109***	1.3738	1.1510	0.8330	0.3896	
SN1 Error	-0.0066	***0.0043***	**0.0089**	-0.0027	-0.0026	-0.0012	5.11E-03
SN2 Error	-0.0075	***0.0038***	**0.0100**	-0.0019	-0.0021	-0.0022	5.53E-03
SN1-r Error	0.0008	***0.0014***	0.0004	-0.0008	-0.0011	-0.0007	9.22E-04
Time=1.46 sec.							
Reference	1.9480	***2.5497***	0.8675	0.3397	0.2048	0.0908	
SN1 Error	-0.0400	***-0.0364***	**0.0918**	-0.0115	-0.0012	-0.0021	4.38E-02
SN2 Error	-0.0589	***-0.0359***	**0.1046**	-0.0121	0.0023	0.0000	5.14E-02
SN1-r Error	-0.0349	***-0.0122***	**0.0706**	-0.0115	-0.0055	-0.0044	3.30E-02
Time=4.06 sec.							
Reference	0.8229	***1.4170***	1.4060	1.1606	0.8200	0.3736	
SN1 Error	-0.0248	***-0.0171***	-0.0280	0.0303	**0.0327**	0.0069	2.49E-02
SN2 Error	**-0.0615**	***-0.0507***	-0.0009	0.0489	0.0449	0.0188	4.30E-02
SN1-r Error	0.0001	***-0.0016***	-0.0006	**0.0020**	0.0010	-0.0008	1.20E-03

bold denotes the maximum error
italic denotes the error at the maximum peak power

Table 4-7 Radial Relative Power Distribution for Test Case 3 at Time=0.08 sec.

Y|X	**1**	**2**	**3**	**4**	**5**	**6**	**7**	**8**
1		**Ref.** **SN1 Err** **SN2 Err** **SN1-r Err**					0.3919 0.0067 0.0069 0.0004	0.4529 0.0106 0.0106 0.0006
2					0.5177 0.0035 0.0040 0.0002	0.7049 0.0066 0.0072 0.0005	0.6675 0.0100 0.0103 0.0007	0.4909 0.0185 0.0176 0.0007
3		**RMS** **9.45E-3** **9.95E-3** **4.36E-4**		0.6097 0.0028 0.0034 0.0001	0.7996 0.0044 0.0052 0.0002	0.8373 0.0060 0.0069 0.0003	0.8925 0.0098 0.0106 0.0005	0.8825 0.0160 0.0166 0.0006
4			0.6147 0.0026 0.0032 0.0001	0.8090 0.0034 0.0041 0.0001	0.9131 0.0041 0.0049 0.0001	1.0157 0.0054 0.0062 0.0001	1.0236 0.0068 0.0076 0.0001	1.0447 0.0081 0.0090 0.0001
5		0.5298 0.0029 0.0034 0.0002	0.8135 0.0037 0.0044 0.0002	0.9221 0.0037 0.0044 0.0001	1.0601 0.0039 0.0047 0.0000	1.0984 0.0041 0.0048 -0.0001	1.1289 0.0047 0.0054 -0.0001	1.0604 0.0046 0.0053 -0.0001
6		0.7281 0.0055 0.0059 0.0005	0.8616 0.0049 0.0056 0.0002	1.0388 0.0043 0.0049 0.0000	1.1132 0.0034 0.0040 -0.0001	1.1837 0.0030 0.0035 -0.0002	1.1682 0.0028 0.0033 -0.0002	1.1737 0.0028 0.0033 -0.0003
7	0.4115 0.0058 0.0058 0.0003	0.6980 0.0085 0.0085 0.0005	0.9318 0.0079 0.0084 0.0003	1.0648 0.0048 0.0053 0.0000	1.1655 0.0028 0.0033 -0.0001	1.1915 0.0017 0.0020 -0.0002	1.2074 0.0011 0.0013 -0.0004	1.1349 0.0009 0.0011 -0.0003
8	0.4816 0.0093 0.0090 0.0005	0.5215 0.0173 0.0160 0.0006	0.9400 0.0134 0.0136 0.0004	1.1117 0.0048 0.0052 -0.0001	1.1237 0.0014 0.0016 -0.0003	1.2320 -0.0002 -0.0001 -0.0003	1.1701 -0.0009 -0.0009 -0.0003	1.2178 -0.0012 -0.0012 -0.0003
9	0.4235 0.0078 0.0078 0.0005	0.7259 0.0137 0.0138 0.0008	0.9742 0.0079 0.0082 0.0001	1.1204 0.0025 0.0027 -0.0002	1.2367 -0.0008 -0.0008 -0.0003	1.2742 -0.0026 -0.0028 -0.0003	1.2992 -0.0037 -0.0040 -0.0004	1.2239 -0.0037 -0.0040 -0.0003
10		0.7837 0.0047 0.0049 0.0001	0.9381 0.0021 0.0025 -0.0001	1.1488 -0.0009 -0.0009 -0.0003	1.2529 -0.0037 -0.0040 -0.0003	1.3552 -0.0059 -0.0065 -0.0003	1.3557 -0.0071 -0.0078 -0.0003	1.3693 -0.0074 -0.0081 -0.0003
11		0.5880 0.0007 0.0008 -0.0001	0.9225 -0.0013 -0.0012 -0.0002	1.0737 -0.0040 -0.0042 -0.0003	1.2710 -0.0071 -0.0077 -0.0002	1.3582 -0.0098 -0.0106 -0.0001	1.4324 -0.0119 -0.0129 -0.0002	1.3612 -0.0114 -0.0125 -0.0002
12			0.7272 -0.0030 -0.0031 -0.0001	0.9948 -0.0062 -0.0067 -0.0001	1.1746 -0.0099 -0.0107 -0.0001	1.3774 -0.0145 -0.0157 0.0001	1.4614 -0.0178 -0.0193 0.0001	1.5291 -0.0191 -0.0206 0.0000
13				0.7944 -0.0071 -0.0075 -0.0001	1.1116 -0.0125 -0.0134 0.0002	1.2668 -0.0176 -0.0192 0.0002	1.5034 -0.0260 -0.0277 0.0006	***1.6143*** ***-0.0298*** ***-0.0314*** ***0.0005***
14					0.7744 -0.0104 -0.0112 0.0002	1.1803 -0.0195 -0.0208 0.0004	1.3869 -0.0295 -0.0310 0.0006	1.4989 **-0.0363** **-0.0374** 0.0001
15							0.9017 -0.0154 -0.0163 -0.0003	1.1831 -0.0112 -0.0122 **-0.0016**

bold denotes the maximum error
italic denotes the error at the maximum peak power

Table 4-7 (continued)

Y|X	9	10	11	12	13	14	15
1	0.3919 0.0092 0.0095 0.0005						
2	0.6675 0.0164 0.0170 0.0010	0.7049 0.0087 0.0095 0.0003	0.5177 0.0043 0.0050 0.0001				
3	0.8925 0.0119 0.0129 0.0003	0.8373 0.0073 0.0084 0.0001	0.7996 0.0052 0.0061 0.0000	0.6097 0.0031 0.0038 -0.0001			
4	1.0236 0.0074 0.0083 0.0000	1.0157 0.0061 0.0070 -0.0001	0.9131 0.0045 0.0053 0.0000	0.8090 0.0036 0.0043 0.0000	0.6147 0.0027 0.0032 0.0001		
5	1.1289 0.0049 0.0056 -0.0001	1.0984 0.0044 0.0051 -0.0001	1.0601 0.0041 0.0048 0.0000	0.9221 0.0037 0.0044 0.0001	0.8135 0.0037 0.0044 0.0002	0.5298 0.0029 0.0034 0.0003	
6	1.1682 0.0028 0.0033 -0.0002	1.1837 0.0030 0.0036 -0.0002	1.1132 0.0032 0.0038 0.0000	1.0388 0.0039 0.0045 0.0002	0.8616 0.0046 0.0052 0.0004	0.7281 0.0057 0.0062 0.0006	
7	1.2074 0.0011 0.0013 -0.0003	1.1915 0.0016 0.0019 -0.0001	1.1655 0.0025 0.0029 0.0001	1.0648 0.0039 0.0043 0.0003	0.9318 0.0063 0.0067 0.0006	0.6980 0.0094 0.0094 0.0007	0.4115 0.0091 0.0092 0.0006
8	1.1701 -0.0009 -0.0009 -0.0003	1.2320 -0.0002 -0.0002 -0.0002	1.1237 0.0010 0.0012 0.0000	1.1117 0.0036 0.0038 0.0003	0.9400 0.0079 0.0078 0.0006	0.5215 0.0187 0.0176 0.0005	0.4816 0.0183 0.0181 0.0016
9	1.2992 -0.0036 -0.0039 -0.0004	1.2742 -0.0025 -0.0027 -0.0002	1.2367 -0.0009 -0.0009 -0.0002	1.1204 0.0018 0.0019 0.0000	0.9741 0.0064 0.0066 0.0002	0.7259 0.0146 0.0148 0.0008	0.4235 0.0111 0.0112 0.0008
10	1.3557 -0.0067 -0.0074 -0.0004	1.3552 -0.0054 -0.0059 -0.0004	1.2529 -0.0033 -0.0036 -0.0003	1.1488 -0.0008 -0.0008 -0.0002	0.9381 0.0021 0.0025 -0.0001	0.7837 0.0052 0.0054 0.0002	
11	1.4324 -0.0110 -0.0120 -0.0004	1.3582 -0.0086 -0.0094 -0.0005	1.2710 -0.0061 -0.0066 -0.0005	1.0737 -0.0033 -0.0035 -0.0004	0.9225 -0.0008 -0.0007 -0.0003	0.5880 0.0010 0.0011 -0.0001	
12	1.4614 -0.0159 -0.0172 -0.0004	1.3774 -0.0122 -0.0132 -0.0006	1.1746 -0.0082 -0.0088 -0.0006	0.9948 -0.0051 -0.0055 -0.0005	0.7272 -0.0024 -0.0024 -0.0003		
13	1.5034 -0.0204 -0.0217 -0.0006	1.2668 -0.0138 -0.0149 -0.0009	1.1116 -0.0099 -0.0106 -0.0007	0.7944 -0.0057 -0.0060 -0.0005			
14	1.3869 -0.0141 -0.0149 -0.0016	1.1803 -0.0138 -0.0148 -0.0010	0.7744 -0.0079 -0.0084 -0.0006				
15	0.9017 -0.0095 -0.0101 -0.0012						

Table 4-8 Radial Relative Power Distribution for Test Case 3 at Time=1.46 sec.

Y|X	1	2	3	4	5	6	7	8
1		**Ref. Err** **SN1 Err** **SN2 Err** **SN1-r Err**					0.4140 -0.0026 0.0027 -0.0017	0.4668 -0.0024 0.0056 -0.0013
2					0.5502 -0.0010 -0.0009 -0.0021	0.6875 -0.0004 0.0002 -0.0021	0.6704 -0.0064 0.0020 -0.0038	0.4148 -0.0011 0.0051 -0.0020
3		**RMS** **4.59E-3** **5.31E-3** **2.84E-3**		0.7011 -0.0005 -0.0003 -0.0014	0.8214 -0.0004 0.0001 -0.0007	0.8697 -0.0096 -0.0015 -0.0035	0.8719 -0.0031 0.0037 -0.0001	0.9358 0.0035 0.0114 0.0055
4			0.7022 -0.0004 -0.0003 -0.0014	0.9312 -0.0048 -0.0009 -0.0019	0.9872 -0.0044 -0.0024 -0.0034	1.0199 -0.0022 -0.0001 -0.0011	1.1567 -0.0023 0.0014 -0.0012	1.2355 -0.0002 0.0049 0.0016
5		0.5529 -0.0008 -0.0009 -0.0020	0.8245 0.0000 0.0001 -0.0006	0.9894 -0.0041 -0.0024 -0.0033	1.0590 -0.0014 -0.0012 -0.0016	1.1930 -0.0026 -0.0024 -0.0035	1.3139 -0.0008 0.0006 -0.0012	1.2392 0.0000 0.0018 -0.0002
6		0.6926 -0.0001 0.0003 -0.0020	0.8755 -0.0085 -0.0015 -0.0033	1.0257 -0.0014 0.0000 -0.0009	1.1973 -0.0021 -0.0024 -0.0034	1.1923 0.0018 0.0000 -0.0003	1.2621 -0.0005 -0.0023 -0.0032	1.1872 0.0028 0.0008 0.0003
7	0.4188 -0.0023 0.0028 -0.0016	0.6776 -0.0057 0.0020 -0.0037	0.8816 -0.0020 0.0037 0.0002	1.1687 -0.0011 0.0013 -0.0008	1.3256 0.0002 0.0006 -0.0008	1.2699 0.0001 -0.0024 -0.0029	1.1839 0.0028 -0.0011 -0.0009	1.1858 0.0004 -0.0030 -0.0035
8	0.4741 -0.0020 0.0056 -0.0011	0.4217 -0.0008 0.0050 -0.0019	0.9519 0.0049 0.0113 0.0060	1.2567 0.0015 0.0046 0.0022	1.2610 0.0016 0.0015 0.0005	1.2074 0.0041 0.0004 0.0010	1.1994 0.0011 -0.0033 -0.0031	1.2977 0.0016 -0.0027 -0.0027
9	0.4228 0.0019 0.0069 0.0027	0.6870 0.0054 0.0126 0.0074	0.8958 0.0027 0.0074 0.0046	1.1893 0.0012 0.0021 0.0010	1.3540 0.0021 0.0003 0.0004	1.3041 0.0015 -0.0032 -0.0021	1.2218 0.0042 -0.0021 -0.0001	1.2245 0.0017 -0.0041 -0.0029
10		0.7114 0.0040 0.0040 0.0027	0.9032 -0.0035 0.0007 0.0002	1.0663 0.0022 0.0004 0.0017	1.2544 0.0009 -0.0034 -0.0015	1.2649 0.0044 -0.0020 0.0015	1.3508 0.0019 -0.0050 -0.0019	1.2768 0.0053 -0.0018 0.0018
11		0.5746 0.0015 0.0005 0.0004	0.8660 0.0029 0.0010 0.0023	1.0525 0.0001 -0.0030 -0.0008	1.1481 0.0023 -0.0036 0.0009	1.3185 0.0005 -0.0066 -0.0014	1.4774 0.0022 -0.0046 0.0009	1.4071 0.0029 -0.0032 0.0014
12			0.7510 0.0012 -0.0005 0.0006	1.0166 0.0004 -0.0024 0.0005	1.1128 -0.0005 -0.0063 -0.0007	1.2029 0.0010 -0.0071 0.0024	1.4181 -0.0016 -0.0089 0.0014	***1.5454*** ***0.0002*** ***-0.0062*** ***0.0031***
13				0.7915 -0.0006 -0.0027 0.0006	0.9797 -0.0012 -0.0052 0.0029	1.1223 0.0004 -0.0117 0.0003	1.2699 -0.0062 -0.0143 0.0056	1.4992 -0.0125 -0.0150 0.0037
14					0.6948 -0.0045 -0.0060 0.0004	0.9834 -0.0095 -0.0098 0.0041	1.2581 -0.0118 -0.0144 0.0027	1.3928 **-0.0291** -0.0107 0.0059
15							0.8558 -0.0003 0.0017 0.0034	1.1380 0.0160 **0.0216** 0.0077

bold denotes the maximum error
italic denotes the error at the maximum peak power

Table 4-8 (continued)

Y|X	9	10	11	12	13	14	15
1	0.4140						
	0.0014						
	0.0069						
	0.0025						
2	0.6704	0.6875	0.5502				
	0.0040	0.0036	0.0008				
	0.0127	0.0044	0.0009				
	0.0069	0.0020	-0.0002				
3	0.8719	0.8697	0.8214	0.7011			
	0.0006	-0.0071	0.0012	0.0002			
	0.0076	0.0013	0.0018	0.0004			
	0.0039	-0.0006	0.0010	-0.0006			
4	1.1567	1.0199	0.9872	0.9312	0.7022		
	-0.0012	-0.0009	-0.0037	-0.0045	-0.0004		
	0.0027	0.0013	-0.0016	-0.0006	-0.0003		
	0.0001	0.0003	-0.0025	-0.0016	-0.0014		
5	1.3139	1.1930	1.0590	0.9894	0.8245	0.5529	
	-0.0005	-0.0022	-0.0013	-0.0043	-0.0004	-0.0010	
	0.0010	-0.0020	-0.0011	-0.0026	-0.0003	-0.0011	
	-0.0008	-0.0031	-0.0015	-0.0036	-0.0011	-0.0023	
6	1.2621	1.1923	1.1973	1.0257	0.8755	0.6926	
	-0.0005	0.0016	-0.0027	-0.0025	-0.0095	-0.0001	
	-0.0023	-0.0002	-0.0031	-0.0012	-0.0027	0.0001	
	-0.0033	-0.0006	-0.0042	-0.0022	-0.0046	-0.0022	
7	1.1839	1.2699	1.3256	1.1687	0.8816	0.6776	0.4188
	0.0026	-0.0004	-0.0010	-0.0034	-0.0053	-0.0051	0.0023
	-0.0012	-0.0030	-0.0007	-0.0011	0.0001	0.0025	0.0074
	-0.0012	-0.0037	-0.0024	-0.0035	-0.0035	-0.0032	0.0029
8	1.1994	1.2074	1.2610	1.2567	0.9519	0.4217	0.4741
	0.0009	0.0035	0.0004	-0.0015	-0.0049	0.0005	0.0103
	-0.0035	-0.0002	0.0001	0.0014	0.0012	0.0064	0.0180
	-0.0034	0.0000	-0.0013	-0.0015	-0.0044	-0.0006	0.0111
9	1.2218	1.3041	1.3540	1.1893	0.8958	0.6870	0.4228
	0.0041	0.0013	0.0011	-0.0008	-0.0004	0.0061	0.0064
	-0.0021	-0.0036	-0.0007	0.0000	0.0040	0.0133	0.0114
	-0.0005	-0.0030	-0.0014	-0.0018	0.0008	0.0077	0.0071
10	1.3508	1.2649	1.2544	1.0663	0.9032	0.7114	
	0.0023	0.0047	0.0008	0.0016	-0.0041	0.0042	
	-0.0046	-0.0016	-0.0034	-0.0003	-0.0001	0.0041	
	-0.0022	0.0008	-0.0026	0.0001	-0.0013	0.0023	
11	1.4774	1.3185	1.1481	1.0525	0.8660	0.5746	
	0.0034	0.0020	0.0034	0.0007	0.0031	0.0016	
	-0.0032	-0.0049	-0.0023	-0.0024	0.0012	0.0006	
	0.0007	-0.0017	0.0003	-0.0017	0.0015	-0.0001	
12	1.4181	1.2029	1.1128	1.0166	0.7510		
	0.0015	0.0044	0.0019	0.0018	0.0019		
	-0.0055	-0.0033	-0.0036	-0.0008	0.0002		
	0.0014	0.0023	-0.0010	0.0001	0.0001		
13	1.2699	1.1223	0.9797	0.7915			
	0.0032	0.0066	0.0030	0.0015			
	-0.0040	-0.0044	-0.0007	-0.0004			
	0.0058	0.0005	0.0029	0.0005			
14	1.2581	0.9834	0.6948				
	0.0150	0.0004	-0.0001				
	0.0132	0.0006	-0.0013				
	0.0036	0.0045	0.0005				
15	0.8558						
	0.0102						
	0.0126						
	0.4140						

Table 4-9 Radial Relative Power Distribution for Test Case 3 at Time=4.06 sec.

Y|X	1	2	3	4	5	6	7	8
1		**Ref. Err**					0.6092	0.7465
		SN1 Err					0.0014	0.0041
		SN2 Err					0.0010	0.0019
		SN1-r Err					0.0014	0.0024
2					0.5408	0.5112	0.7747	0.5524
					-0.0052	0.0103	-0.0013	0.0063
					-0.0056	0.0160	-0.0034	0.0013
					-0.0008	0.0037	0.0003	0.0026
3		**RMS**		0.8561	0.6575	0.7877	0.6880	1.1398
		1.10E-2		-0.0093	0.0096	-0.0074	0.0169	0.0002
		1.48E-2		-0.0077	0.0161	-0.0099	0.0222	-0.0050
		6.44E-3		-0.0041	0.0027	-0.0021	0.0046	-0.0015
4			0.8566	1.1394	0.9759	0.7374	1.4104	1.7424
			-0.0093	-0.0109	-0.0112	0.0139	-0.0079	-0.0005
			-0.0077	-0.0075	-0.0130	0.0198	-0.0111	-0.0015
			-0.0034	-0.0016	-0.0031	0.0050	-0.0035	0.0007
5		0.5419	0.6585	0.9767	0.7297	1.1997	1.6847	1.6329
		-0.0052	0.0096	-0.0112	0.0118	-0.0125	-0.0063	-0.0051
		-0.0056	0.0162	-0.0130	0.0174	-0.0174	-0.0087	-0.0067
		-0.0001	0.0031	-0.0025	0.0047	-0.0039	-0.0007	-0.0021
6		0.5128	0.7899	0.7393	1.2019	0.8620	1.2626	0.8895
		0.0103	-0.0074	0.0140	-0.0125	0.0179	-0.0127	0.0179
		0.0160	-0.0100	0.0199	-0.0174	0.0248	-0.0181	0.0249
		0.0042	-0.0005	0.0061	-0.0034	0.0065	-0.0044	0.0063
7	0.6123	0.7782	0.6911	1.4165	1.6911	1.2659	0.7968	1.1000
	0.0014	-0.0014	0.0170	-0.0080	-0.0062	-0.0127	0.0137	-0.0110
	0.0010	-0.0036	0.0223	-0.0113	-0.0087	-0.0182	0.0190	-0.0158
	0.0017	0.0011	0.0060	-0.0019	0.0001	-0.0042	0.0047	-0.0037
8	0.7510	0.5559	1.1469	1.7534	1.6434	0.8951	1.1046	1.3820
	0.0041	0.0064	0.0002	-0.0004	-0.0052	0.0180	-0.0111	-0.0099
	0.0018	0.0013	-0.0052	-0.0016	-0.0070	0.0249	-0.0159	-0.0137
	0.0026	0.0029	-0.0001	0.0022	-0.0016	0.0064	-0.0037	-0.0022
9	0.6137	0.7810	0.6941	1.4233	1.7023	1.2785	0.8078	1.1153
	0.0041	0.0048	0.0183	-0.0076	-0.0063	-0.0131	0.0136	-0.0115
	0.0036	0.0025	0.0235	-0.0111	-0.0089	-0.0187	0.0189	-0.0165
	0.0019	0.0011	0.0086	-0.0027	-0.0003	-0.0044	0.0047	-0.0039
10		0.5172	0.7981	0.7486	1.2211	0.8846	1.3097	0.9256
		0.0117	-0.0064	0.0144	-0.0129	0.0180	-0.0143	0.0179
		0.0173	-0.0092	0.0202	-0.0181	0.0249	-0.0204	0.0248
		0.0033	-0.0612	0.0036	-0.0044	0.0066	-0.0047	0.0065
11		0.5495	0.6707	1.0000	0.7534	1.2594	1.7978	1.7585
		-0.0047	0.0101	-0.0114	0.0119	-0.0145	-0.0092	-0.0088
		-0.0053	0.0166	-0.0136	0.0174	-0.0203	-0.0128	-0.0116
		-0.0015	0.0004	-0.0057	0.0040	-0.0045	-0.0006	-0.0025
12			0.8795	1.1788	1.0257	0.8019	1.5877	***2.0010***
			-0.0096	-0.0113	-0.0123	0.0139	-0.0138	***-0.0082***
			-0.0084	-0.0085	-0.0149	0.0198	-0.0187	***-0.0111***
			-0.0055	-0.0044	-0.0033	0.0059	-0.0034	***0.0010***
13				0.8976	0.7135	0.9246	0.9223	1.6860
				-0.0103	0.0097	-0.0107	0.0179	**-0.0193**
				-0.0093	0.0161	-0.0145	0.0248	**-0.0267**
				-0.0090	0.0035	0.0025	0.0084	-0.0035
14					0.6139	0.6752	1.4158	1.8013
					-0.0068	0.0113	-0.0118	-0.0019
					-0.0082	0.0179	-0.0159	-0.0079
					-0.0030	0.0045	-0.0033	0.0052
15							1.1752	1.6603
							0.0032	0.0173
							-0.0003	0.0100
							-0.0051	-0.0005

bold denotes the maximum error
italic denotes the error at the maximum peak power

Table 4-9 (continued)

Y|X	9	10	11	12	13	14	15
1	0.6092 0.0041 0.0037 0.0022						
2	0.7747 0.0049 0.0026 0.0014	0.5112 0.0116 0.0172 0.0039	0.5408 -0.0045 -0.0049 -0.0026				
3	0.6880 0.0181 0.0234 0.0052	0.7877 -0.0063 -0.0088 -0.0016	0.6575 0.0100 0.0166 0.0028	0.8561 -0.0090 -0.0074 -0.0040			
4	1.4104 -0.0074 -0.0107 -0.0032	0.7374 0.0142 0.0201 0.0052	0.9759 -0.0109 -0.0126 -0.0029	1.1394 -0.0106 -0.0073 -0.0016	0.8566 -0.0092 -0.0076 -0.0035		
5	1.6847 -0.0061 -0.0085 -0.0006	1.1997 -0.0124 -0.0172 -0.0039	0.7297 0.0118 0.0174 0.0047	0.9767 -0.0112 -0.0130 -0.0029	0.6585 0.0096 0.0162 0.0026	0.5419 -0.0051 -0.0055 -0.0005	
6	1.2626 -0.0127 -0.0181 -0.0044	0.8620 0.0178 0.0247 0.0064	1.2019 -0.0128 -0.0177 -0.0039	0.7393 0.0137 0.0196 0.0055	0.7899 -0.0076 -0.0102 -0.0018	0.5128 0.0106 0.0163 0.0035	
7	0.7968 0.0136 0.0189 0.0047	1.2659 -0.0130 -0.0185 -0.0045	1.6911 -0.0070 -0.0095 -0.0007	1.4165 -0.0091 -0.0124 -0.0033	0.6911 0.0161 0.0215 0.0120	0.7782 0.0002 -0.0020 -0.0006	0.6123 0.0059 0.0053 0.0021
8	1.1046 -0.0112 -0.0160 -0.0038	0.8951 0.0178 0.0247 0.0063	1.6434 -0.0061 -0.0079 -0.0022	1.7534 -0.0022 -0.0034 0.0009	1.1469 -0.0047 -0.0100 -0.0022	0.5559 0.0078 0.0026 0.0026	0.7510 0.0145 0.0119 0.0040
9	0.8078 0.0136 0.0188 0.0047	1.2785 -0.0133 -0.0190 -0.0046	1.7023 -0.0070 -0.0097 -0.0005	1.4233 -0.0087 -0.0122 -0.0026	0.6941 0.0175 0.0227 0.0079	0.7810 0.0064 0.0040 0.0020	0.6137 0.0085 0.0079 0.0033
10	1.3097 -0.0142 -0.0203 -0.0047	0.8846 0.0180 0.0249 0.0066	1.2211 -0.0131 -0.0184 -0.0041	0.7486 0.0142 0.0200 0.0060	0.7981 -0.0066 -0.0093 0.0112	0.5172 0.0120 0.0176 0.0041	
11	1.7978 -0.0089 -0.0125 -0.0005	1.2594 -0.0142 -0.0200 -0.0045	0.7534 0.0120 0.0175 0.0041	1.0000 -0.0113 -0.0135 -0.0047	0.6707 0.0102 0.0166 0.0036	0.5495 -0.0046 -0.0052 -0.0009	
12	1.5877 -0.0129 -0.0177 -0.0032	0.8019 0.0145 0.0204 0.0058	1.0257 -0.0118 -0.0144 -0.0036	1.1788 -0.0109 -0.0081 -0.0044	0.8795 -0.0094 -0.0082 -0.0051		
13	0.9223 0.0205 0.0273 0.0089	0.9246 -0.0087 -0.0125 0.0018	0.7135 0.0105 0.0168 0.0018	0.8976 -0.0097 -0.0088 -0.0101			
14	1.4158 0.0024 -0.0018 0.0001	0.6752 0.0139 0.0204 0.0048	0.6139 -0.0055 -0.0070 -0.0075				
15	1.1752 0.0091 0.0058 0.0013						

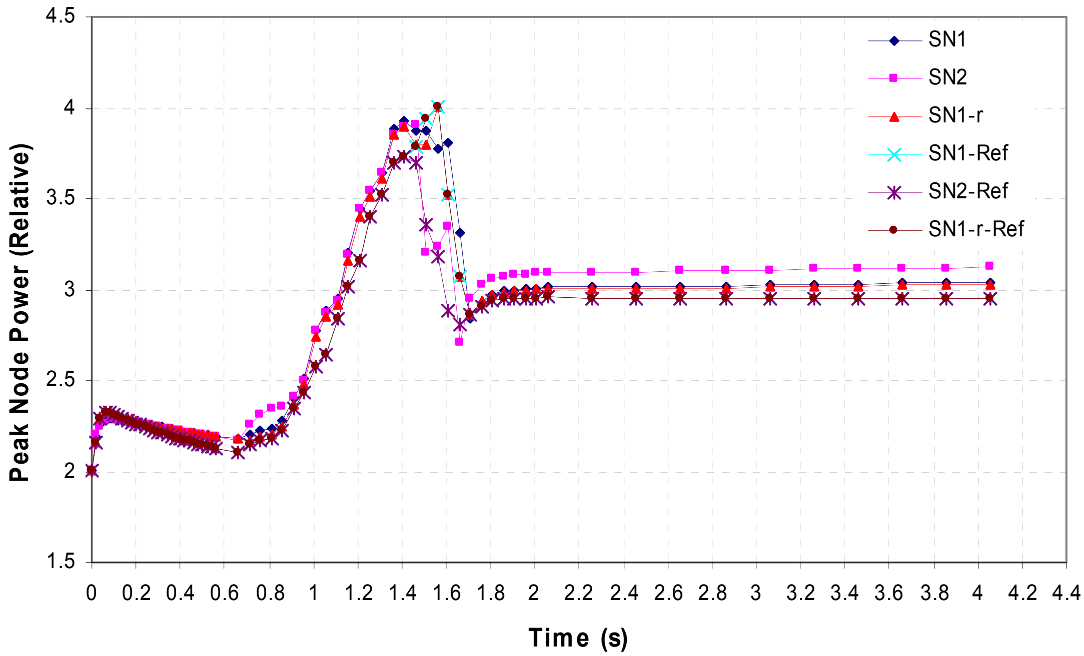

Figure 4.43 **Coarse Mesh Relative Peak Node Power for Test Case 3 "Fine Mesh Determined Peak Node Location"**

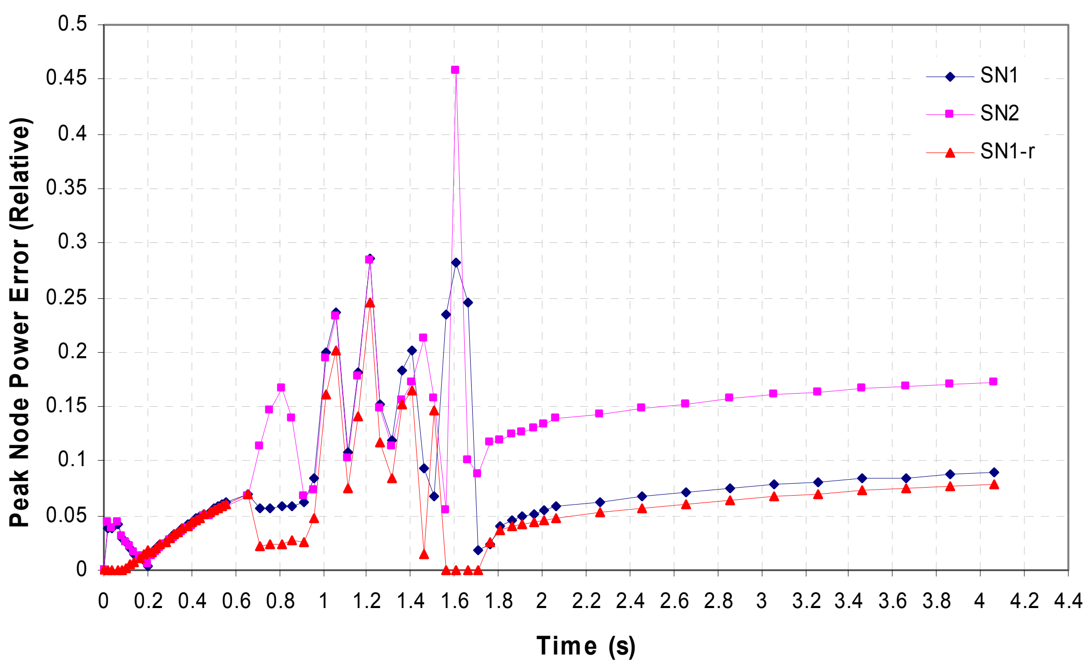

Figure 4.44 **Coarse Mesh Relative Peak Node Power Error for Test Case 3 "Fine Mesh Determined Peak Node Location"**

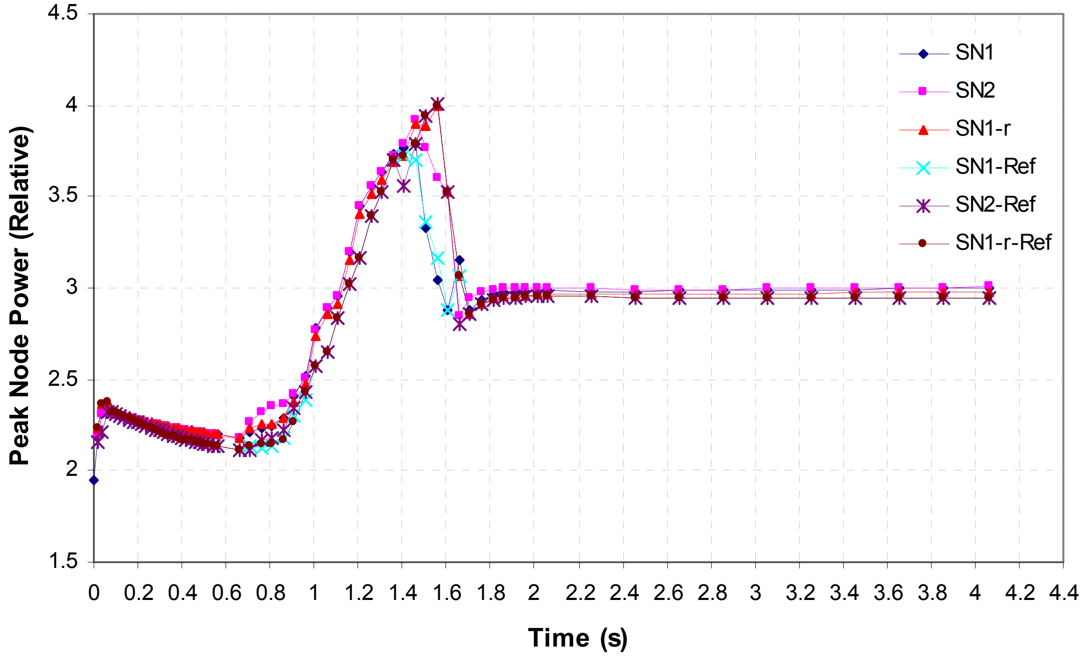

Figure 4.45 **Coarse Mesh Relative Peak Node Power for Test Case 3 "Coarse Mesh Determined Peak Node Location"**

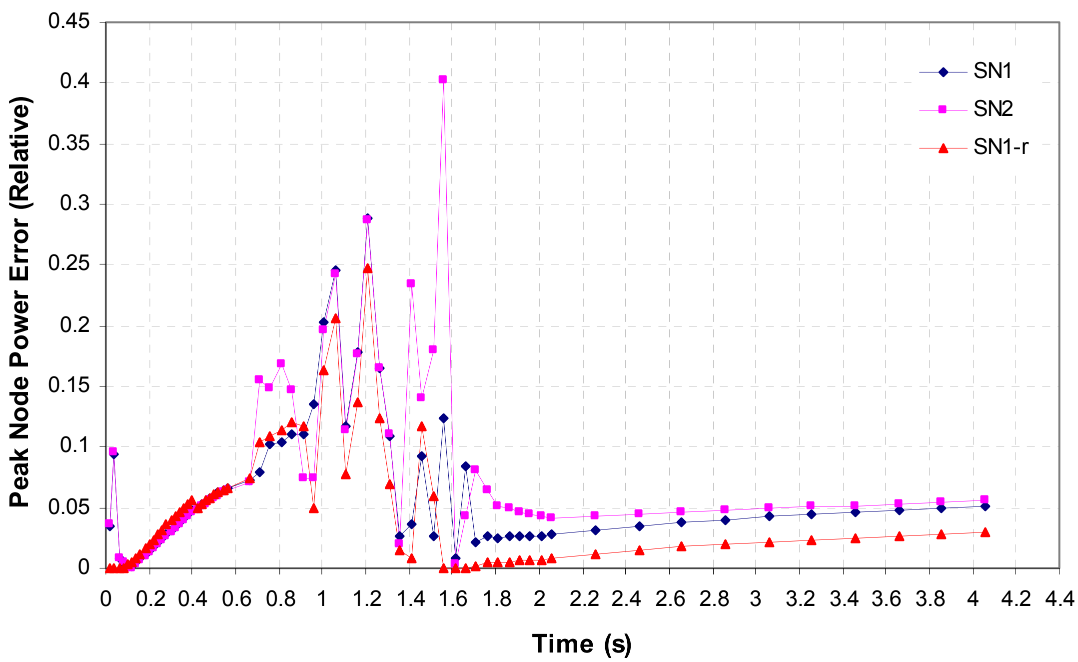

Figure 4.46 **Coarse Mesh Relative Peak Node Power Error for Test Case 3 "Coarse Mesh Determined Peak Node Location"**

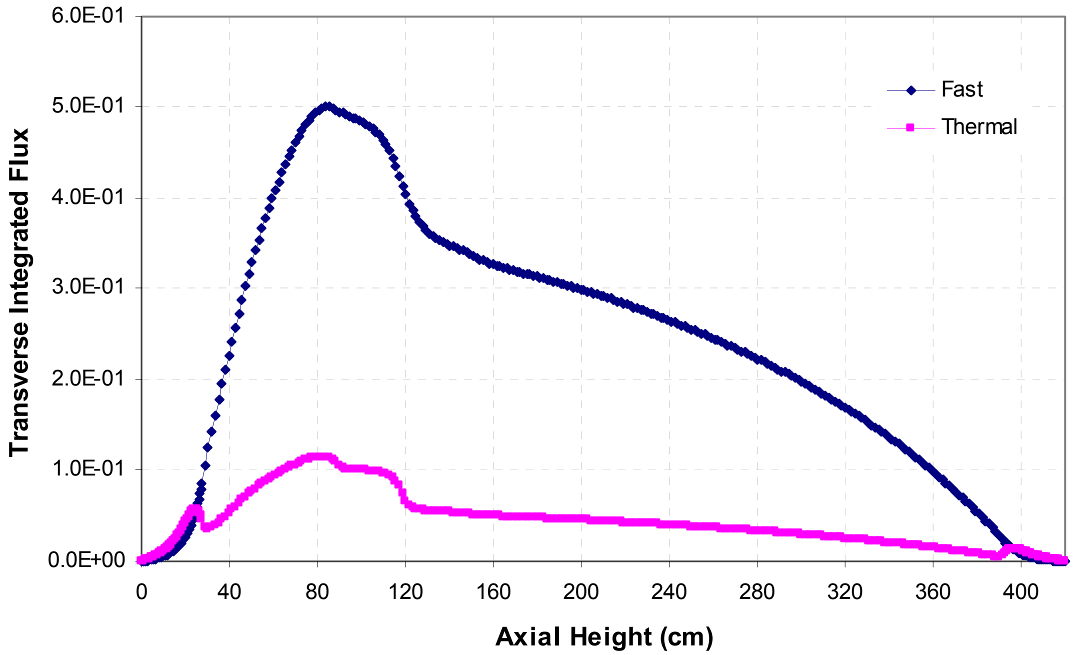

Figure 4.47 **Transverse Integrated Flux for the Reference Solution for a Representative Node at Time=0 sec. for Test Case 3**

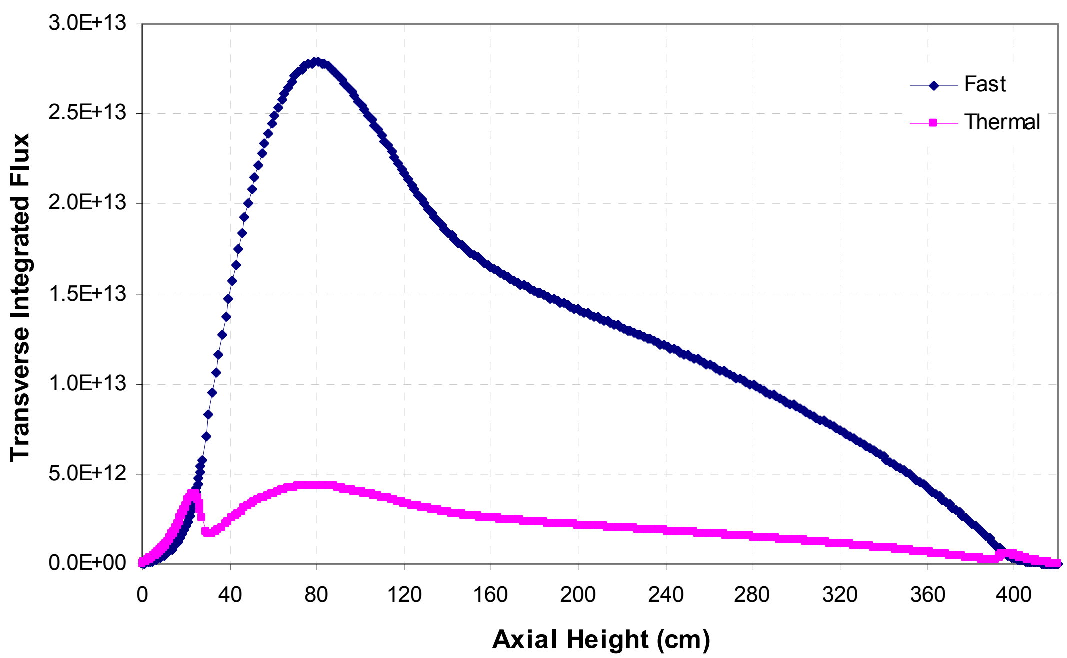

Figure 4.48 **Transverse Integrated Flux for the Reference Solution for a Representative Node at Time=1.56 sec. for Test Case 3**

Table 4-10 CPU Time Comparison for Test Case 3

	Reference	SN1	SN2	SN1-r
CPU Time In Steady State Collapsing	0.0	4.32	3.67	4.33
CPU Time In Transient Collapsing (average)	0.0	0.0	0.0	4.08
CPU Time In Refining Step (fine+coarse)	0.0	0.0	0.0	40.55
Total Number Outer Iteration	708	669	609	777
Total Code CPU Time	263.49	171.12	126.12	207.53

4.2.5 Test Case 4: Steam Line Break Accident

This is the second accident analyzed, taken from the 2001 McGuire UFSAR [35]. The steam line break accident is initiated by a rupture in the main steam piping between the steam generators and the turbine. The steam release from the ruptured line results in an increase in steam flow for a period of time. With the increasing energy removal from the Reactor Cooling System (RCS), a reduction in the reactor coolant temperature and the pressure occur. The reactor would trip on a low primary system pressure signal, or on low steam generator pressure or low level signal. As the primary system temperature decreases, there is neutronics feedback through the moderator temperature reactivity effect. In the presence of a negative moderator temperature coefficient, the cooldown results in an insertion of positive reactivity. Therefore, there is a potential for a recriticality event and return to power even after reactor trip if one assumes a stuck out control rod assembly. If there is a return to the power, there is a potential problem for some fuel rods to exceed the burnout heat flux because of the adverse power profile after the scram with the stuck out control assembly. Borated water via the Emergency Core Cooling System, which is activated for this transient, is injected in the primary system to mitigate the return to power [36].

In order to simulate the accident conditions, the reactor is modeled in full core geometry. The core is depleted to 10,000 MWD/MTU to create EOC conditions, which results in the core being 1300 pcm subcriticality at zero ppm boron concentration with all control rod assemblies in except the stuck control rod assembly. The stuck control rod assembly which has the highest reactivity worth is calculated to be the same control rod assembly as ejected in the Test Case 3 as indicated in Figure 4.33. The first 100 seconds of the accident after the insertion of N-1 rods is simulated by applying the core average inlet temperature transient as given in Figure 4.49. Since the non-uniform core inlet temperature distribution is not known, a uniform distribution was used. The core power level, peak node power and related errors are calculated for the SN1 nodalization with multiple refine and collapse steps, the results presented in Figure 4.51 through Figure 4.56. Unfortunately, for this test case SN2 nodalization fails beyond 14 sec, the time that prompt criticality is achieved. Multiple refine and collapse steps are also necessary to achieve convergence for SN1 nodalization independent of accuracy requirements. The time intervals for refine-collapse are shown in Table 4-11. The axial and radial power maps presented in Table 4-12 through Table 4-15 show that RMS errors for the SN1-r scheme increase in time, but note that the highest RMS at the end of the transient is still very low.

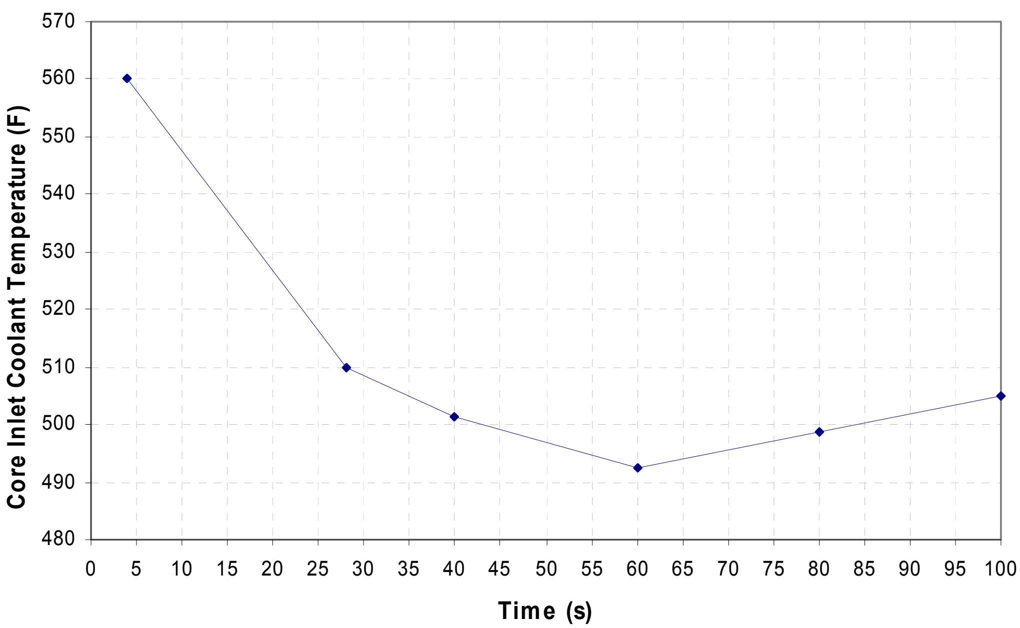

Figure 4.49 Core Average Inlet Coolant Temperature for Test Case 4

The coarse mesh relative peak node powers and related errors are shown in Figure 4.58 and Figure 4.59, respectively. Since the fine mesh and coarse mesh determined coarse mesh peak node locations are identical only one of them is presented for this test case. The insignificant change in the magnitude of the peak node power errors between Figure 4.59 and Figure 4.54 shows that the flux form factor errors are negligible compared to the Super-Nodal solution errors.

The steam line break accident analysis is a difficult problem to analyze even using fine mesh nodalization because of strong thermal-hydraulic feedback and drastic changes in the power level and distribution throughout the transient. Therefore it is necessary to carry the solution to the fine mesh level many times for this test case. Thus the savings in CPU time is very small for this test case, as shown in Table 4-16.

The relative residual plot represents well the error in the coarse mesh solution for this test case. As can easily be seen in Figure 4.57, the residual starts to increase sharply before each refine step. The large residual at the initial refined solution steps and sudden drop in the error at the time steps after that are also consistent with the error in the collapsed solution.

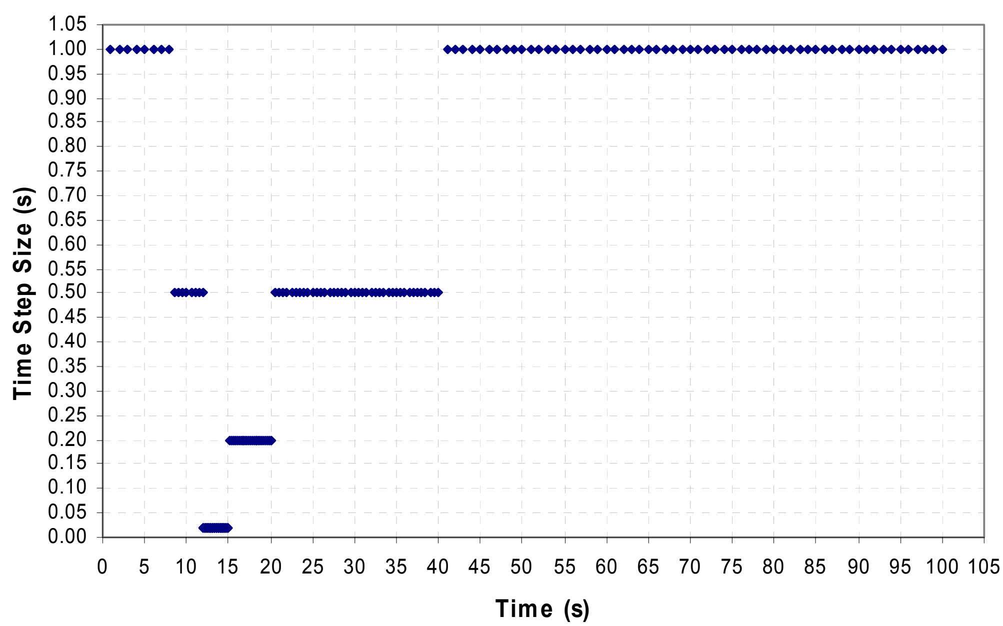

Figure 4.50 Time Step Size for Test Case 4

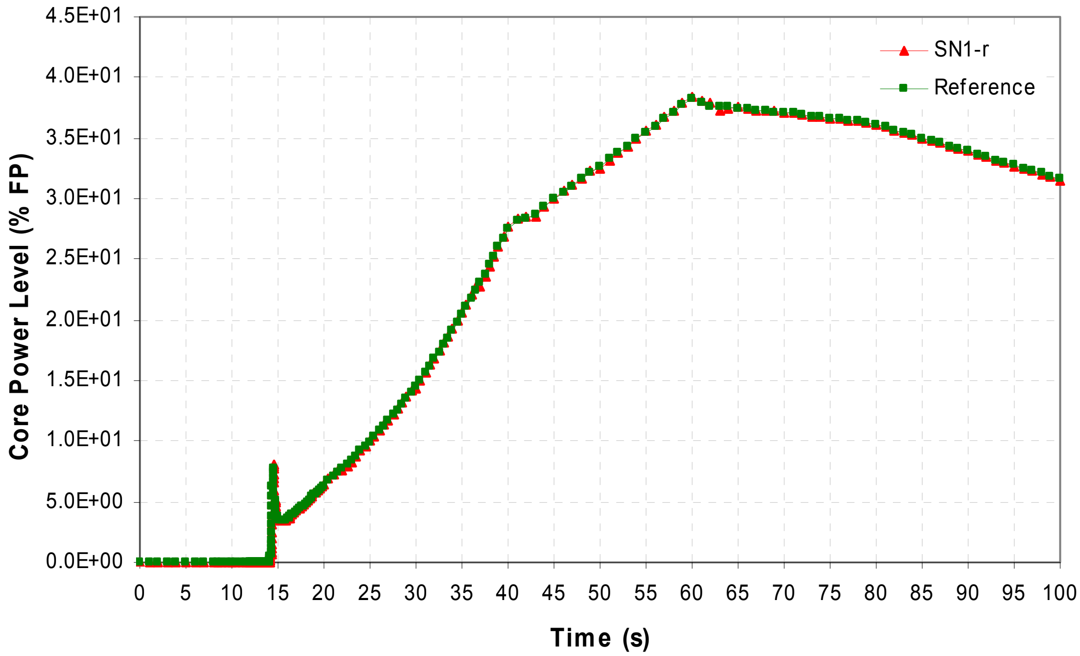

Figure 4.51 Core Power Level for Test Case 4

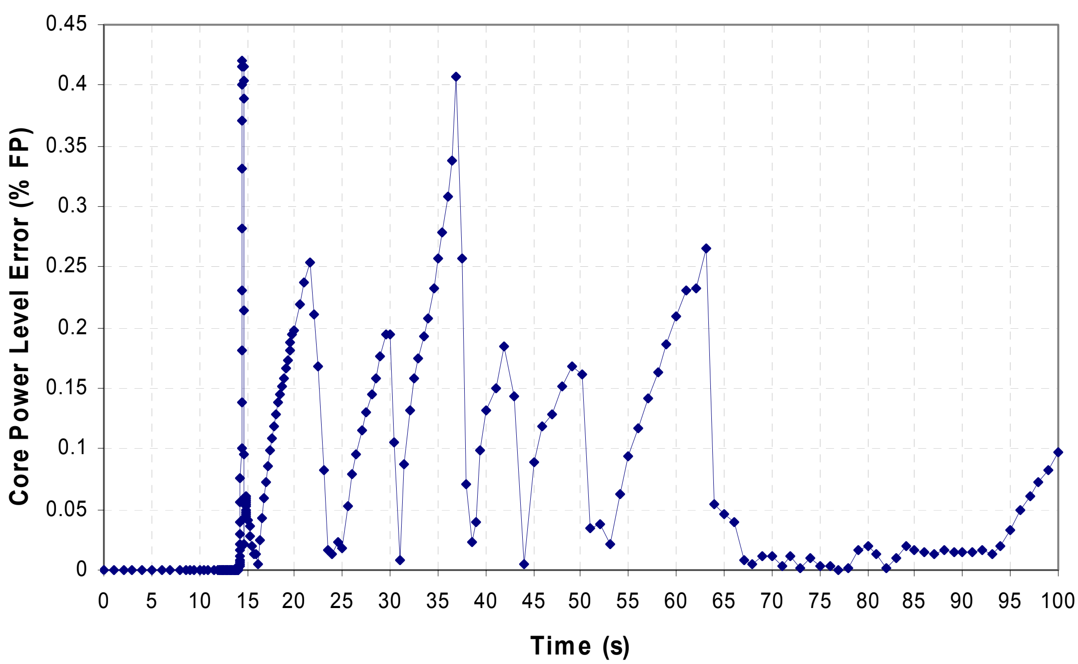

Figure 4.52 Core Power Level Error for Test Case 4

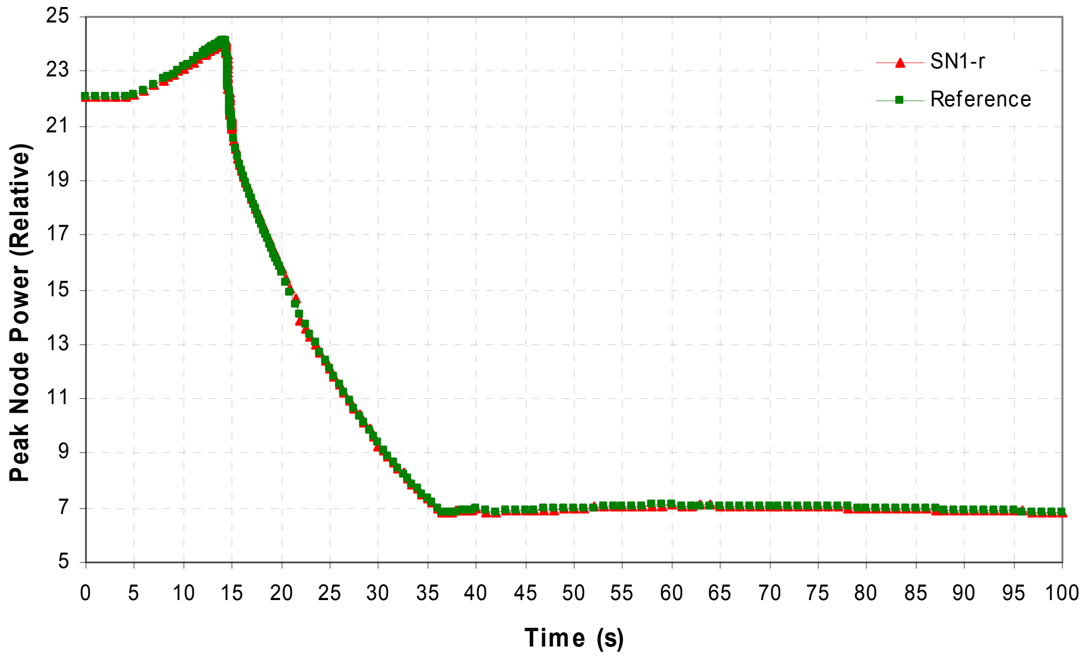

Figure 4.53 Relative Peak Node Power for Test Case 4

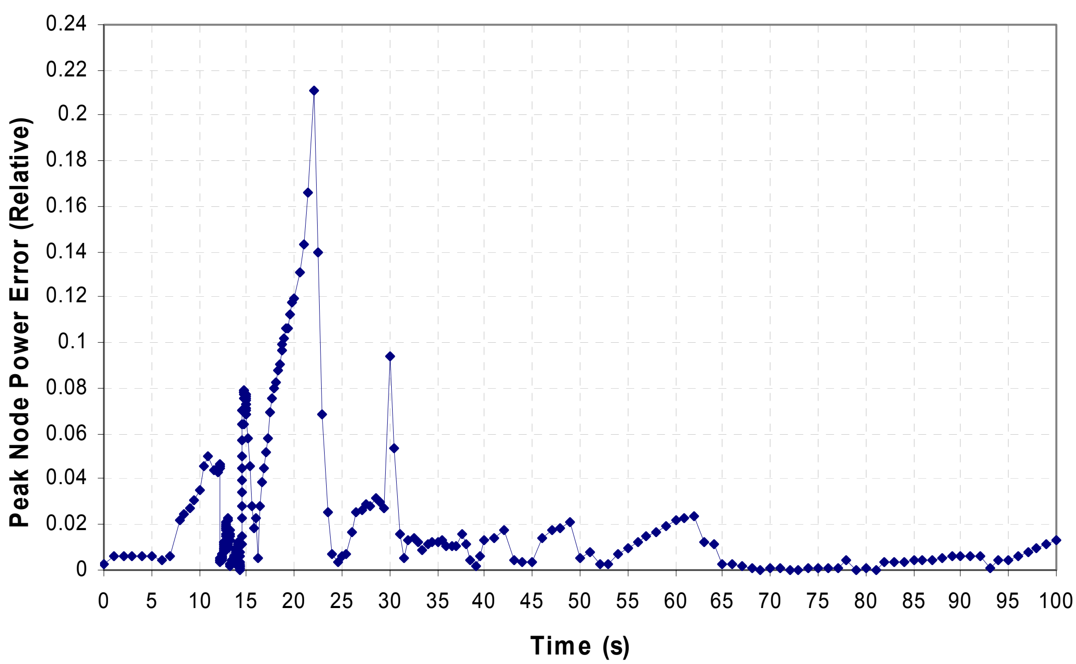

Figure 4.54 Relative Peak Node Power Error for Test Case 4

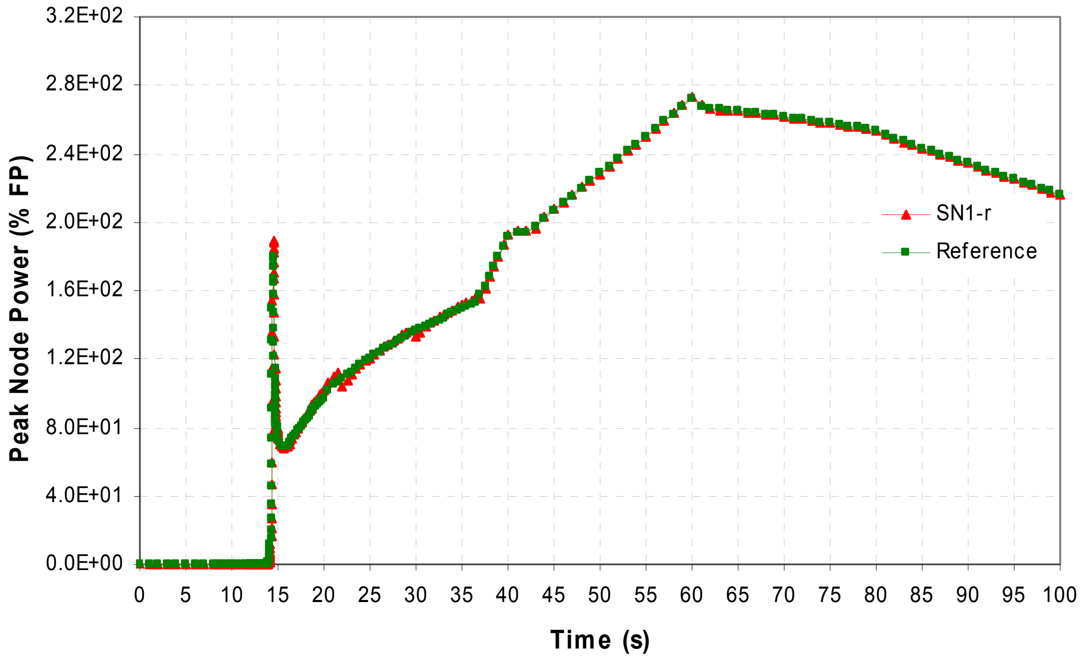

Figure 4.55 Peak Node Power for Test Case 4

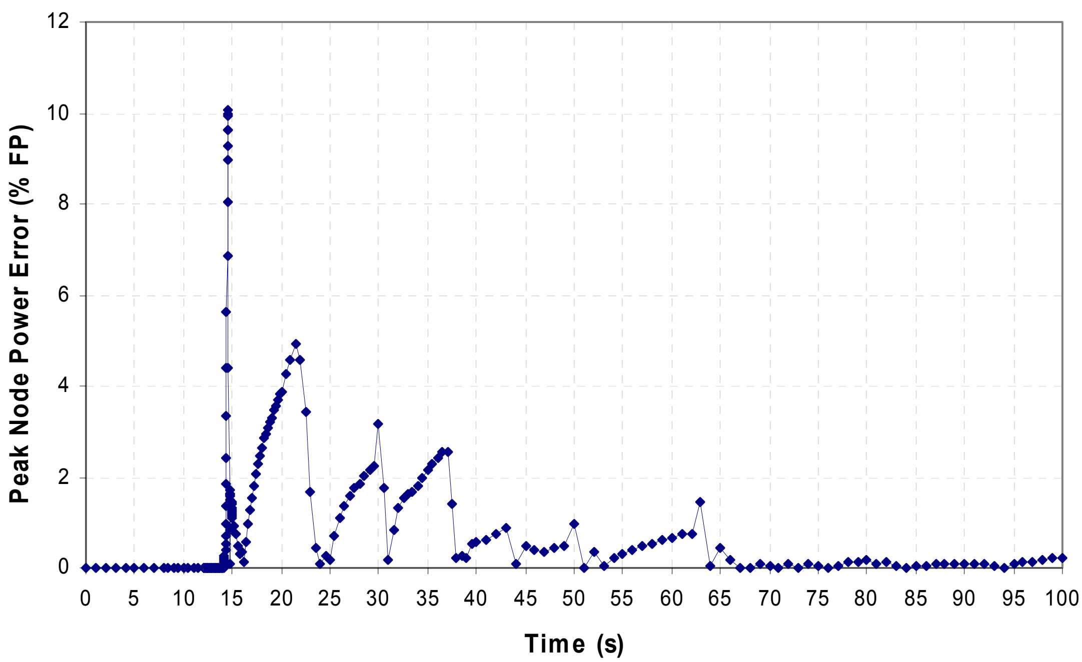

Figure 4.56 Peak Node Power Error for Test Case 4

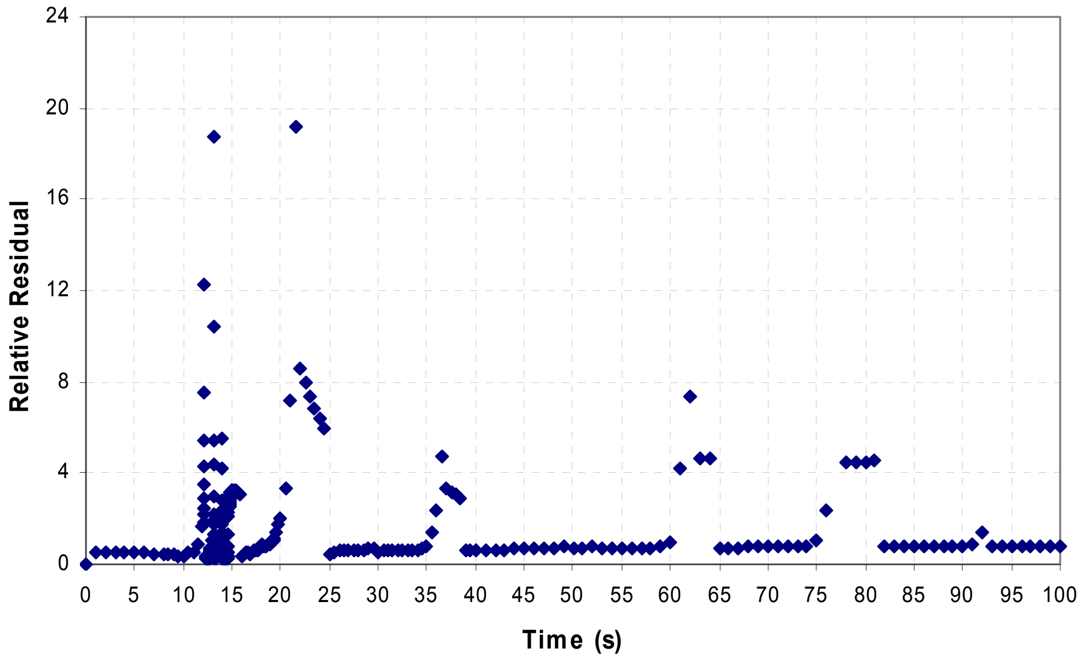

Figure 4.57 Relative Residual for Test Case 4

Table 4-11 Refine-Collapse Steps for Test Case 4

Refine Step Number	Refined	Collapsed
1	12.22	12.24
2	13.24	13.26
3	14.06	14.08
4	14.64	16.00
5	22.00	25.00
6	37.00	39.00
7	30.00	30.50
8	50.00	53.00
9	63.00	65.00
10	78.00	82.00
11	43.00	43.05
12	93.00	93.50

Table 4-12 Axial Power Map for Test Case 4

Axial Location (in)	**12**	**36**	**60**	**84**	**108**	**132**	**RMS**
Time=1.0 sec.							
Reference	0.1382	0.2869	0.6117	1.2395	***2.0031***	1.7206	
SN1-r Error	0.0000	0.0000	-0.0001	-0.0001	***-0.0001***	**0.0003**	0.0001
Time=40.0 sec.							
Reference	0.5974	0.7654	0.8801	1.1421	***1.4479***	1.1671	
SN1-r Error	**0.0012**	0.0006	0.0000	-0.0005	***-0.0011***	-0.0002	0.0007
Time=100.0 sec.							
Reference	0.6577	0.8180	0.9003	1.1240	***1.3893***	1.1107	
SN1-r Error	-0.0013	-0.0012	-0.0005	0.0005	***0.0018***	0.0007	0.0011

Table 4-13 Radial Power Map for Test Case 4 at Time=1.0 sec.

Y|X	1	2	3	4	5	6	7	8
1		**Ref. Err**					0.0770	0.0927
		SN1-r Err					0.0000	0.0000
2					0.0608	0.0568	0.1039	0.0751
					0.0000	-0.0001	0.0000	0.0000
3		**RMS**		0.1233	0.0868	0.1123	0.1080	0.2015
		5.99E-5		-0.0001	0.0000	0.0000	0.0000	0.0000
4			0.1374	0.1854	0.1624	0.1254	0.2963	0.3634
			0.0000	0.0000	0.0000	0.0000	0.0000	0.0000
5		0.0925	0.1180	0.1964	0.1444	0.2630	0.3773	0.4058
		0.0000	0.0000	0.0000	0.0000	0.0000	0.0000	0.0000
6		0.1079	0.1985	0.2062	0.3762	0.2298	0.3373	0.2279
		0.0000	-0.0001	0.0000	0.0000	0.0000	0.0000	0.0000
7	0.1786	0.2305	0.2293	0.5992	0.6901	0.4947	0.2816	0.4440
	0.0000	-0.0001	0.0000	0.0000	0.0000	0.0000	0.0000	0.0000
8	0.2304	0.1841	0.4795	0.8445	0.9099	0.4454	0.6173	0.7588
	0.0000	0.0000	0.0000	-0.0001	0.0000	0.0000	-0.0001	0.0000
9	0.2069	0.2879	0.2969	0.8021	1.0402	0.9197	0.6425	1.0008
	0.0000	0.0000	0.0000	0.0000	-0.0001	0.0000	-0.0001	0.0000
10		0.1974	0.4050	0.4484	0.9537	0.9075	1.9241	1.3797
		0.0000	0.0000	0.0000	0.0000	0.0000	0.0000	0.0000
11		0.2758	0.4303	0.8442	0.7515	1.9858	3.5546	4.1584
		0.0000	0.0000	0.0000	0.0000	0.0000	0.0000	0.0000
12			0.7412	1.1933	1.3545	1.4570	4.0896	5.3895
			0.0000	0.0000	-0.0001	0.0000	0.0000	0.0001
13				1.0456	1.1036	2.2783	2.9309	6.1300
				0.0000	0.0000	0.0000	0.0000	0.0001
14					1.1862	2.0567	6.5180	8.3220
					0.0000	0.0000	0.0002	0.0002
15	**bold** denotes the maximum error						6.1577	***8.6715***
	italic denotes the error at the maximum peak power						0.0002	***0.0004***

Table 4-13 (continued)

Y|X	9	10	11	12	13	14	15
1	0.0770						
	0.0000						
2	0.1039	0.0568	0.0608				
	0.0000	-0.0001	0.0000				
3	0.1080	0.1123	0.0868	0.1233			
	0.0000	0.0000	0.0000	-0.0001			
4	0.2963	0.1254	0.1624	0.1854	0.1374		
	0.0000	0.0000	0.0000	0.0000	0.0000		
5	0.3773	0.2630	0.1444	0.1964	0.1180	0.0925	
	0.0000	0.0000	0.0000	0.0000	0.0000	0.0000	
6	0.3373	0.2298	0.3762	0.2062	0.1985	0.1079	
	0.0000	0.0000	0.0000	0.0000	-0.0001	0.0000	
7	0.2816	0.4947	0.6901	0.5992	0.2293	0.2305	0.1786
	0.0000	0.0000	0.0000	0.0000	0.0000	-0.0001	0.0000
8	0.6173	0.4454	0.9099	0.8445	0.4795	0.1841	0.2304
	-0.0001	0.0000	0.0000	-0.0001	0.0000	0.0000	0.0000
9	0.6425	0.9197	1.0402	0.8021	0.2969	0.2879	0.2069
	-0.0001	0.0000	-0.0001	0.0000	0.0000	0.0000	0.0000
10	1.9241	0.9075	0.9537	0.4484	0.4050	0.1974	
	0.0000	0.0000	0.0000	0.0000	0.0000	0.0000	
11	3.5546	1.9858	0.7515	0.8442	0.4303	0.2758	
	0.0000	0.0000	0.0000	0.0000	0.0000	0.0000	
12	4.0896	1.4570	1.3545	1.1933	0.7412		
	0.0000	0.0000	-0.0001	0.0000	0.0000		
13	2.9309	2.2783	1.1036	1.0456			
	0.0000	0.0000	0.0000	0.0000			
14	6.5180	2.0567	1.1862				
	0.0002	0.0000	0.0000				
15	6.1577						
	0.0002						

Table 4-14 Power Map for Test Case 4 at Time=40.0 sec.

Y|X	**1**	**2**	**3**	**4**	**5**	**6**	**7**	**8**
1		**Ref.Err**					0.3976	0.4878
		SN1-r Err					-0.0001	-0.0002
2					0.2436	0.2363	0.4727	0.3360
					0.0000	-0.0001	-0.0001	-0.0001
3		**RMS**		0.4637	0.3219	0.4277	0.4155	0.7991
		2.02E-4		-0.0001	-0.0001	-0.0001	-0.0001	-0.0003
4			0.4712	0.6471	0.5526	0.4231	1.0750	1.3459
			0.0000	-0.0001	-0.0001	-0.0001	-0.0003	-0.0004
5		0.2608	0.3380	0.5695	0.3980	0.7957	1.2333	1.3672
		0.0000	0.0000	0.0000	-0.0001	-0.0002	-0.0004	-0.0004
6		0.2638	0.4717	0.4617	0.8503	0.5390	0.8776	0.5835
		0.0000	0.0000	0.0000	-0.0001	-0.0001	-0.0002	-0.0001
7	0.4601	0.5438	0.4749	1.2202	1.3796	0.9507	0.4948	0.7620
	0.0000	0.0001	0.0000	0.0000	-0.0001	0.0000	0.0000	0.0000
8	0.5721	0.3948	0.9357	1.5709	1.6001	0.6792	0.8364	0.9982
	0.0000	0.0000	0.0000	0.0000	0.0000	0.0000	0.0000	0.0000
9	0.4754	0.5738	0.5071	1.3119	1.5311	1.1319	0.6447	0.9965
	0.0000	0.0001	0.0000	0.0001	0.0001	0.0001	0.0001	0.0001
10		0.3106	0.5771	0.5750	1.1073	0.8268	1.5530	1.0645
		0.0000	0.0001	0.0000	0.0001	0.0002	0.0003	0.0002
11		0.3605	0.5027	0.8993	0.6761	1.5503	2.5745	2.9518
		0.0001	0.0001	0.0002	0.0001	0.0003	0.0005	0.0006
12			0.7981	1.1734	1.1361	1.0222	2.7427	3.5132
			0.0001	0.0003	0.0002	0.0002	0.0005	0.0005
13				0.9476	0.8296	1.4883	1.7743	3.6731
				0.0002	0.0001	0.0001	0.0001	0.0000
14					0.8194	1.2441	3.7705	4.7206
					0.0000	0.0000	-0.0004	-0.0008
15	**bold** denotes the maximum error						3.5204	***4.8398***
	italic denotes the error at the maximum peak power						-0.0004	***-0.0009***

Table 4-14 (continued)

Y|X	9	10	11	12	13	14	15
1	0.3976						
	-0.0001						
2	0.4727	0.2363	0.2436				
	-0.0001	-0.0001	0.0000				
3	0.4155	0.4277	0.3219	0.4637			
	-0.0001	-0.0001	-0.0001	-0.0001			
4	1.0750	0.4231	0.5526	0.6471	0.4712		
	-0.0003	-0.0001	-0.0001	-0.0001	0.0000		
5	1.2333	0.7957	0.3980	0.5695	0.3380	0.2608	
	-0.0004	-0.0002	-0.0001	0.0000	0.0000	0.0000	
6	0.8776	0.5390	0.8503	0.4617	0.4717	0.2638	
	-0.0002	-0.0001	-0.0001	0.0000	0.0000	0.0000	
7	0.4948	0.9507	1.3796	1.2202	0.4749	0.5438	0.4601
	0.0000	0.0000	-0.0001	0.0000	0.0000	0.0000	0.0000
8	0.8364	0.6792	1.6001	1.5709	0.9357	0.3948	0.5721
	0.0000	0.0000	0.0000	0.0000	0.0000	0.0000	0.0000
9	0.6447	1.1319	1.5311	1.3119	0.5071	0.5738	0.4754
	0.0001	0.0001	0.0001	0.0001	0.0000	0.0001	0.0000
10	1.5530	0.8268	1.1073	0.5750	0.5771	0.3106	
	0.0003	0.0002	0.0001	0.0000	0.0001	0.0000	
11	2.5745	1.5503	0.6761	0.8993	0.5027	0.3605	
	0.0005	0.0003	0.0001	0.0002	0.0001	0.0001	
12	2.7427	1.0222	1.1361	1.1734	0.7981		
	0.0005	0.0002	0.0002	0.0003	0.0001		
13	1.7743	1.4883	0.8296	0.9476			
	0.0001	0.0001	0.0001	0.0002			
14	3.7705	1.2441	0.8194				
	-0.0004	0.0000	0.0000				
15	3.5204						
	-0.0004						

Table 4-15 Power Map for Test Case 4 at Time=100.0 sec.

Y|X	**1**	**2**	**3**	**4**	**5**	**6**	**7**	**8**
1		**Ref.Err**					0.4696	0.5761
		SN1-r Err					-0.0006	-0.0007
2					0.2843	0.2751	0.5503	0.3901
					-0.0003	-0.0003	-0.0007	-0.0005
3		**RMS**		0.5362	0.3718	0.4903	0.4709	0.9004
		2.23E-4		-0.0007	-0.0005	-0.0007	-0.0006	-0.0012
4			0.5412	0.7411	0.6302	0.4760	1.1953	1.4899
			-0.0007	-0.0009	-0.0008	-0.0006	-0.0015	-0.0019
5		0.2959	0.3826	0.6415	0.4440	0.8822	1.3594	1.5066
		-0.0003	-0.0005	-0.0008	-0.0006	-0.0011	-0.0015	-0.0017
6		0.2937	0.5200	0.5020	0.9190	0.5868	0.9611	0.6396
		-0.0003	-0.0006	-0.0006	-0.0010	-0.0007	-0.0011	-0.0007
7	0.5121	0.5987	0.5112	1.2933	1.4582	1.0116	0.5286	0.8124
	-0.0006	-0.0007	-0.0006	-0.0014	-0.0016	-0.0011	-0.0005	-0.0008
8	0.6339	0.4306	0.9941	1.6435	1.6681	0.7084	0.8682	1.0323
	-0.0008	-0.0005	-0.0011	-0.0017	-0.0017	-0.0007	-0.0007	-0.0008
9	0.5241	0.6221	0.5363	1.3633	1.5734	1.1506	0.6443	0.9933
	-0.0007	-0.0007	-0.0005	-0.0013	-0.0014	-0.0008	-0.0003	-0.0004
10		0.3306	0.6028	0.5905	1.1182	0.8099	1.4823	1.0118
		-0.0003	-0.0005	-0.0004	-0.0006	-0.0003	0.0000	0.0001
11		0.3749	0.5130	0.9022	0.6637	1.4722	2.3983	2.7334
		-0.0002	-0.0002	-0.0002	-0.0001	0.0001	0.0006	0.0008
12			0.8005	1.1593	1.0986	0.9580	2.5217	3.2090
			-0.0001	0.0001	0.0003	0.0006	0.0015	0.0021
13				0.9265	0.7892	1.3722	1.6084	3.3051
				0.0003	0.0006	0.0017	0.0023	0.0048
14					0.7662	1.1286	3.3580	4.1889
					0.0010	0.0021	0.0076	0.0099
15	**bold** denotes the maximum error						3.1226	***4.2763***
	italic denotes the error at the maximum peak power						0.0091	***0.0158***

Table 4-15 (continued)

Y|X	9	10	11	12	13	14	15
1	0.4696						
	-0.0006						
2	0.5503	0.2751	0.2843				
	-0.0007	-0.0003	-0.0003				
3	0.4709	0.4903	0.3718	0.5362			
	-0.0006	-0.0007	-0.0005	-0.0007			
4	1.1953	0.4760	0.6302	0.7411	0.5412		
	-0.0015	-0.0006	-0.0008	-0.0009	-0.0007		
5	1.3594	0.8822	0.4440	0.6415	0.3826	0.2959	
	-0.0015	-0.0011	-0.0006	-0.0008	-0.0005	-0.0003	
6	0.9611	0.5868	0.9190	0.5020	0.5200	0.2937	
	-0.0011	-0.0007	-0.001	-0.0006	-0.0006	-0.0003	
7	0.5286	1.0116	1.4582	1.2933	0.5112	0.5987	0.5121
	-0.0005	-0.0011	-0.0016	-0.0014	-0.0006	-0.0007	-0.0006
8	0.8682	0.7084	1.6681	1.6435	0.9941	0.4306	0.6339
	-0.0007	-0.0007	-0.0017	-0.0017	-0.0011	-0.0005	-0.0008
9	0.6443	1.1506	1.5734	1.3633	0.5363	0.6221	0.5241
	-0.0003	-0.0008	-0.0014	-0.0013	-0.0005	-0.0007	-0.0006
10	1.4823	0.8099	1.1182	0.5905	0.6028	0.3306	
	0.0000	-0.0003	-0.0006	-0.0004	-0.0005	-0.0003	
11	2.3983	1.4722	0.6637	0.9022	0.5130	0.3749	
	0.0006	0.0001	-0.0001	-0.0002	-0.0002	-0.0002	
12	2.5217	0.9580	1.0986	1.1593	0.8005		
	0.0015	0.0006	0.0003	0.0001	-0.0001		
13	1.6084	1.3722	0.7892	0.9265			
	0.0023	0.0017	0.0006	0.0003			
14	3.3580	1.1286	0.7662				
	0.0076	0.0021	0.0010				
15	3.1226						
	0.0091						

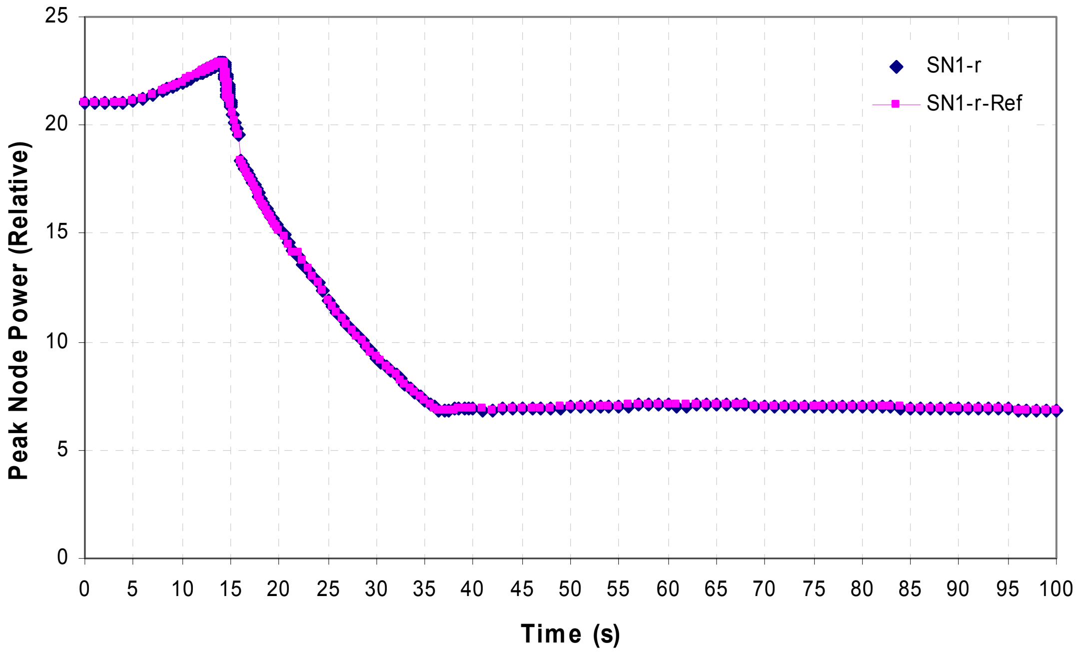

Figure 4.58 Coarse Mesh Relative Peak Node Power for Test Case 4 "Fine Mesh Determined Peak Node Location"

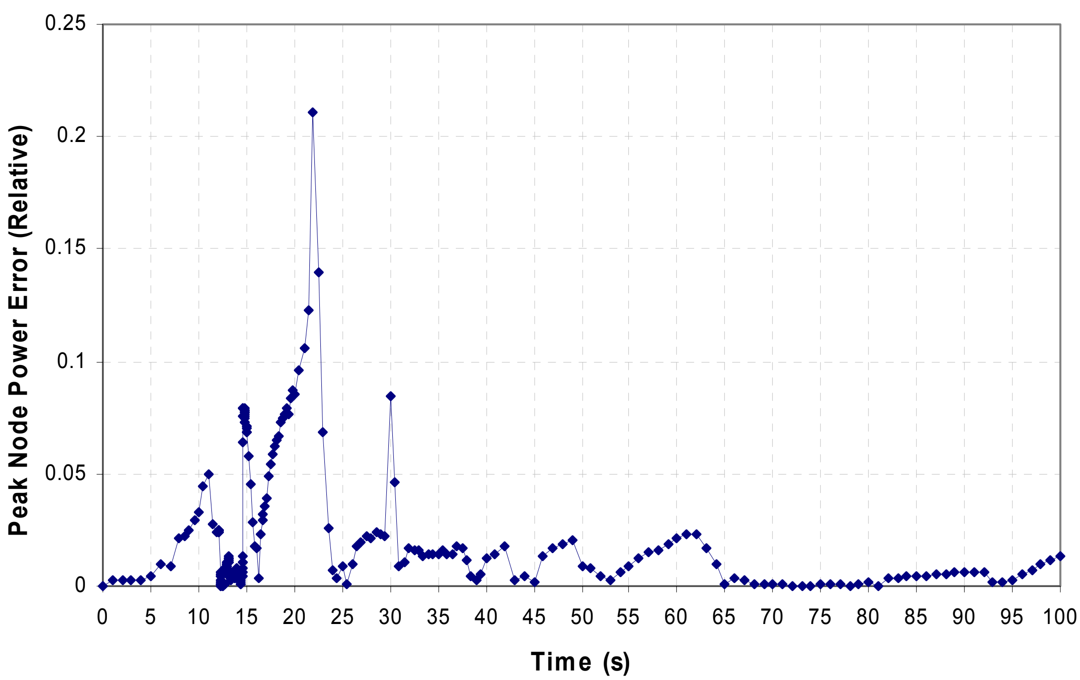

Figure 4.59 Coarse Mesh Relative Peak Node Power Error for Test Case 4 "Fine Mesh Determined Peak Node Location"

Table 4-16 CPU Time Comparison for Test Case 4

	Reference	SN1-r
CPU Time In Steady State Collapsing	0.0	4.14
CPU Time In Transient Collapsing (average)	0.0	3.93
CPU Time In Refining Steps (fine+coarse)	0.0	414.48
Total Number Outer Iteration	4901	4992
Total Code CPU Time	1452.48	1262.64

5. Summary and Recommendations

An advanced Super-Nodal method is developed to reduce the run time of 3-D core neutronics models suchas in the NESTLE reactor core simulator and FORMOSA nuclear fuel management optimization codes. An increase of the computational performance of the neutronics models can be achieved by reducing the number of spatial nodes used in the core modeling. However, as the number of spatial nodes decreases the error in the solution increases. The main idea behind the Super-Nodal method is to reduce the error associated with the use of coarse nodes in the analyses, by providing a new set of cross sections and ADFs (Assembly Discontinuity Factors) for the new nodalization. These so called homogenization parameters are obtained by preserving reaction rates, and surface currents, hence core reactivity, obtained from the reference fine mesh solution.

During this research a new type of singularity, namely “fundamental mode singularity”, is addressed in the ANM solution. The “Coordinate Shifting” approach is developed as a method to address this singularity. Also the “Buckling Shifting” approach is developed as an alternative and more accurate method to address the zero buckling singularity, which is a more common and well known singularity problem in the ANM solution. In the course of addressing the treatment of these singularities, an effort was made to provide better and more robust results from the Super-Nodal method by developing several new methods for determining the transverse leakage and collapsed diffusion coefficient, which generally are the two main approximations in the ANM methodology. Unfortunately, the proposed new transverse leakage and diffusion coefficient approximations failed to provide a consistent improvement to the current methodology. The effect of these two approximations on the Super-Nodal solution is evident, therefore the current Super-Nodal methodology can be improved if an adaptive diffusion coefficient which minimizes the homogenization errors or reduces the CMDF ratios at interfaces is developed, along with a more physical based approximation of transverse leakages.

The proposed Super-Nodal method was tested for large heterogeneities and severe reactor accidents using a three loop Westinghouse reactor core model. Two nodalizations, SN1 and SN2, have been used with three types of collapsing schemes, namely SN1, SN2, and SN1-r. The core is axially collapsed from 18 nodes to 12 and 8 nodes in the SN1 and SN2 nodalizations, respectively. While the SN1 and SN2 schemes refer to SN1 and SN2 nodalizations, SN1-r refers to SN1 nodalization with multiple refining steps. The first test case is the steady state analysis of the Westinghouse reactor core. The general core geometry is modified to introduce a strong heterogeneity by introducing partial length BP rods in four central fuel assemblies. Even though the Super-Nodal method agrees well with the fine mesh, *i.e.* reference, solution for the axial and radial power distributions, it fails to represent the intra-nodal flux shape for the BP loaded assemblies. In this test case, the two proposed singularity treatments are also shown to be effective for the nodes with the zero buckling and the fundamental mode singularities. The second test case is a transient version of the first test case. The core is depleted and a control rod bank is inserted and withdrawn in 40 seconds. A computer CPU time speedup of 1.53 and 1.64 are achieved for the SN1 and SN2 schemes, respectively. Both schemes represent the core power level with a small error; however, both schemes fail to accurately represent the peak node power during the transient. The SN1-r scheme with two additional refining steps removes this discrepancy with a decreased speedup of 1.24.

Test Case 3 is a rod ejection accident as described in the 2001 McGuire UFSAR. Similar to Test Case 2, all three schemes predict accurately the core power level; however, only the SN1-r scheme shows good accuracies for the peak node power. The SN1, SN2 and SN1-r schemes give speedups of 1.53, 2.08 and 1.26, respectively.

Test Case 4 is the large steam line break accident again as described in the McGuire UFSAR. This accident is the most challenging of all four test cases because of the strong thermal-hydraulic feedback and severe changes in the core state throughout the transient. The SN1 and SN2 schemes fail to converge beyond the point that the prompt criticality is reached. The SN1-r scheme agrees well with the reference solutions axial and radial power distributions. It also provides an accurate prediction of the peak node power except at the time of the prompt criticality, where the peak node power error reaches 10% of full rated power. The speedup is also low for this case, 1.15, due to the need for frequent refine-collapse steps in order to achieve adequate accuracy.

All the transient test cases showed that updating of the coarse mesh parameters during the transient resulted in considerable improvements in accuracy of the solution. The coarse mesh solution obviously reduces the CPU time; however, large errors in the estimate of the peak node power can be observed if the state of the reactor deviates from the reference state that the collapsing was performed at. These large errors can lead to failure of the coarse mesh solution to converge. Therefore, frequent changes in the reactor state require frequent updates of the homogenization parameters. However, as the error in the coarse mesh solution increases, refinement steps take more iterations to converge, which in turn increases the CPU time. Therefore, for an efficient Super-Nodal algorithm, it is necessary to minimize the number of refinement steps and the number of time steps that fine mesh calculations are performed at before returning to the coarse mesh level.

The transient test cases involving control rod movement or partially rodded nodes demonstrated the adverse effect of control rods on the collapsing scheme. Since the coarse mesh rodded and unrodded cross sections are calculated using the same node average flux, the reaction rates are not preserved for the partially rodded coarse nodes. This inconsistent collapsing of cross sections increases the homogenization errors causing large CMDFs and reduced robustness, which in turn increases the CPU time to solve the collapsed nodalization core model.

The rod cusping treatment improves the neutronics solution for control rod induced transients by providing better homogenization of the rodded and unrodded cross-sections for the partially rodded nodes. If a similar approach can be developed to be used in the one-node problem solved during homogenization, better accuracy for the coarse mesh solution can be achieved. However, this approach should not be expected to lead to more accurate results in the Super-Nodal solution if the location of the control rod tip is changed after the collapsing. Ideally, one would want to characterize homogenized cross section and CMDFs as a function of control rod fractional insertion in a node. Even if this is accomplished, errors due to collapse will continue to exist since homogenization parameters are a function of the flux shape within a coarse node, which in the axial direction is a strong function of control rods throughout the core.

Although updates of the coarse mesh homogenization parameters through refining steps improves the coarse mesh solution, refining steps are costly. A considerable portion of the CPU time is spent at the first fine mesh solution during each refining step. The initial estimate of the ANM correction factors ($\tilde{\boldsymbol{D}}$), which are taken from the last fine mesh solution, are poor and responsible for this slow convergent behavior. If the fine mesh $\tilde{\boldsymbol{D}}$ values can be correlated to the coarse mesh $\tilde{\boldsymbol{D}}$ values, the coarse mesh $\tilde{\boldsymbol{D}}$ values can be prolangated to provide a better estimate of the fine mesh $\tilde{\boldsymbol{D}}$ values, thereby increasing the efficiency of the refinement step.

References

[1] Alchalabi, R., Turinsky P. J., Faure F. X., Sarsour H., Engrad P., "NESTLE : A Nodal Kinetics Code," *Trans. Am. Nucl. Soc*., **67**, 432 (1993).

[2] Moore B. R., Turinsky P. J., Karve A., "FORMOSA-B: A Boiling Water Reactor In-Core Fuel Management Optimization Package," *Nucl. Technol*., **126**, 153 (1999).

[3] Bennewitz F., Finnemann H. and Moldschl H., "Solution of the Multidimensional Neutron Diffusion Equation by Nodal Expansion," *Proc. Conf. Computatonal Methods in Nuclear Engineering,* 1-99 CONF-750413 ANS, Charleston, S.C., 15-17 April (1975).

[4] Finnemann H., Bennewitz F. and Wagner M.R., "Interface Currents Techniques for Multidimensional Reactor Calculations," *Atomkernenergie*, **30**, 123 (1977).

[5] Bennewitz F., Finnemann H. and Wagner M.R., "Higher-Order Corrections in Nodal Reactor Calculations," *Trans. Am. Nucl. Soc*. **22**,250 (1975).

[6] Maeder C., "A nodal diffusion method with Legendre polynomials, "*Proc. Topical Meeting on Advances in Reactor Physics*, 121, ANS, Gatlingburg, TN, 10-12 April (1978).

[7] Henry A. F. "Refinements in Accuracy of Coarse Mesh Finite-Difference Solution of Group-Diffusion Equations," *Proc. Seminar on Numerical Reactor Calculations*, 447 IAEA, Vienna 17-21 January (1972).

[8] Antonopoulous P.T., "Large Mesh Nodal Development Study," Thesis, Department of Nuclear Engineering, MIT (1972).

[9] Shober R. A. "Nonlinear Methods for Solving the Diffusion Equation," Thesis, Department of Nuclear Engineering, MIT (1976).

[10] Smith K. S., "Analytical Nodal Method for Solving the Two-Group, Multidimensional, Static and Transient Neutron Diffusion Equations," Thesis, Department of Nuclear Engineering, MIT (1979).

[11] R. D. Lawrance, "Progress in Nodal Methods for The Solution of The Neutron Diffusion and Transport Equations," *Prog. Nucl. Energy*, **17**,303 (1986).

[12] Greenman G., Smith K. S. and Henry A. F., "Recent Advances in Analytical Nodal Method for Static and Transient Reactor Analysis," *Proc. Computational Methods in Nuclear Engineering*, 349 ANS, Williamsburg, VA 23-25 April (1979).

[13] A. M. Ougouag and H. L. Rajic, "Illico-Ho: A Self Consistent Higher Order Coarse Mesh Nodal Method," *Nucl. Sci. Eng.* **100**, 332 (1988).

[14] Chao Y. A, Suo C. A. and Penkrot J. A., "On The Theory of Interface Flux Nodal Method," *Proc. Int, Conf. Numerical Methods in Nuclear Eng*., Montreal Canada September 6-9 (1983).

[15] Chang M. H., Moon K. S., Noh J. M and Kim S. K., "A Nodal Expansion Method with Spatially Coupled Effects Incorporated into The Transverse Leakage Approximation," *Nucl. Sci. Eng.*, **103,** 343 (1989).

[16] Noh J. M., Cho N. Z., "A New Approach of Analytical Basis Function Expansion to Neutron Diffusion Nodal Calculation," *Nucl. Sci. And Eng.*, **116**,165 (1994).

[17] Joo H. G., Jiang G. Downar T., "Stabilization Techniques for The Nonlinear Analytical Nodal Method," *Nucl. Sci. Eng.*, **130**, 47 (1998).

[18] Koebke K., "A New Approach to Homogenization and Group Condensation," IAEA-TECDOC-231 (1978).

[19] Smith K. S., "Spatial Homogenization Methods for Light Water Reactors," Thesis, Dept. of Nucl. Eng., MIT (1980).

[20] Gamino R. G., "The Development and Application of Supernodal Methods to PWR Analysis," Thesis, Dept. of Nucl. Eng. MIT (1986).

[21] Delp. D. L., "FLARE A Three Dimensional Boiling Water Reactor Simulator," Rep. GEAP-4598 General Electric, San Jose CA (1964).

[22] Ciarlet P. G., The Finite Element Method for Elliptic Problems, North-Holland, Amsterdam (1978).

[23] Strang G., Fix G. J., An Analysis of The Finite Element Method, Prentice-Hall, Englewood Cliffs, NJ (1973)

[24] Fedon-Magnaud Ch., Hennart J. P., Lautard J. J., "On The Relationship Between Some Nodal Schemes and The Finite Element Method in Static Diffusion Calculations," *Advances in Reactor Computations*, **2**, 987 Salt Lake City, UT, (1983).

[25] Hennart J. P., "On The Numerical Analysis of Analytical Nodal Methods," *Numerical Methods for Partial Differential Equations*, **4**, 233 John Wiley &Sons (1988).

[26] Penland R. C., Azmy Y. Y. and Turinsky P. J., "Error Analysis of The Nodal Expansion Method for Solving The Neutron Diffusion Equation," *Nucl. Sci. Eng.* **125**, 284 (1997).

[27] Smith K. S., Ver Planc and D., Edenius, M., "QPANDA An Advanced Nodal Method for LWR Analyses," *Trans. Am. Nucl. Soc.*, **50**, 532 November (1985).

[28] Hoxie, C. L., and Henry A. F.,"Reconstruction of Heterogenous PWR Flux Shapes from Nodal calculations," *Trans. Am. Nucl. Soc*. **39**, 905 December (1981).

[29] Khalil H.S., "The Application of Nodal Methods to PWR Analysis," Thesis, Department of Nuclear Engineering, MIT (1983).

[30] Perez J. F., "Reconstruction of Three- Dimensional Flux Shapes from Nodal Solutions," Nuclear Engineer's Thesis, Department of Nuclear Engineering, M.I.T. Cambridge, MA June (1984).

[31] Klaus Koebke Manfred Wagner, "The Determination of The Pin Power Distribution in A Reactor Core on the Basis of Nodal Coarse Mesh Calculations" Atomkernenergie Bd. 30 (1977)Lfg. 2 P 139

[32] Smith K. S, "Nodal Method Storage Reduction by Non-Linear Iteration," *Trans. Am. Nucl. Soc.* **44**, 265 (1983)

[33] D. Anderson, J. Tannehill and R. Pletcher, <u>Computational Fluid Mechanics and Heat Transfer</u>, Hemisphere Publishing Corporation, (1984).

[34] Smith, K. S, VerPlanck D. M., "SIMULATE-3: Advanced Three-Dimensional Two-Group Reactor analysis Code," STUDSVIK-89/04, Studsvik of America, Inc. (1989).

[35] Duke Energy Company, McGuire Nuclear Station Updated Final Safety Analysis Report (2001).

[36] Abramson P. B., Light Water Reactor Safety Analysis, Hemisphere Publishing Corporation (1985).

[37] NESTLE 6.1 *Code Manual,* Electric Power Research Center, Raleigh, North Carolina July (1997).

[38] R. Alchalabi, "Development of An Efficient Multigrid Method for The NEM Form of The Multigroup Neutron Diffusion Equation," Thesis, Department of Nuclear Engineering, N.C. State University (1997).

[39] Haberman R., Elementary Applied Partial Differential Equations, Prentice Hall Inc., NJ (1987).

APPENDIX

Solution of two-group diffusion equation for a homogenous node in 2-D using Fourier Series.

The two group diffusion equation in 2-D is given as,

$$
\begin{aligned}
-\boldsymbol{D}_1(\nabla_x^2\phi_1 + \nabla_y^2\phi_1) + (\Sigma_{r1} - \frac{1}{\boldsymbol{k}}\nu\Sigma_{f1})\phi_1 - \frac{1}{\boldsymbol{k}}\nu\Sigma_{f2}\phi_2 = 0 \\
-\boldsymbol{D}_2(\nabla_x^2\phi_2 + \nabla_y^2\phi_2) + \Sigma_{r2}\phi_2 - \Sigma_{s21}\phi_1 = 0
\end{aligned}
\tag{A 1}
$$

with non-homogenous boundary conditions,

$$
\alpha\phi + \beta\vec{\boldsymbol{n}}_s \cdot \vec{\boldsymbol{J}} = \boldsymbol{f}(\boldsymbol{x},\boldsymbol{y}) \text{ for } (x,y)\in\Gamma,\ x\in[-1/2,+1/2],\ y\in[-1/2,+1/2] \tag{A 2}
$$

In order to simplify the solution, Equation (A 1) can be decoupled with respect to energy group. Using the eigenvectors of the system of equations given in Equation (A 1), the following decoupled system of equations are obtained,

$$
\begin{aligned}
\nabla_x^2\Phi_1 + \nabla_y^2\Phi_1 + \boldsymbol{B}_{m1}^2\Phi_1 = 0 \\
\nabla_x^2\Phi_2 + \nabla_y^2\Phi_2 + \boldsymbol{B}_{m2}^2\Phi_2 = 0
\end{aligned}
\tag{A 3}
$$

where

$$
\begin{aligned}
\Phi_1(\boldsymbol{x},\boldsymbol{y}) &= \frac{\phi_1(\boldsymbol{x},\boldsymbol{y}) - \boldsymbol{s}\phi_2(\boldsymbol{x},\boldsymbol{y})}{\boldsymbol{r}-\boldsymbol{s}} \\
\Phi_2(\boldsymbol{x},\boldsymbol{y}) &= \frac{-\phi_1(\boldsymbol{x},\boldsymbol{y}) + \boldsymbol{r}\phi_2(\boldsymbol{x},\boldsymbol{y})}{\boldsymbol{r}-\boldsymbol{s}}
\end{aligned}
\tag{A 4}
$$

and

$$
\begin{aligned}
\boldsymbol{B}_{m1}^2 &= \kappa^2 \\
\boldsymbol{B}_{m1}^2 &= \mu^2
\end{aligned}
\tag{A 5}
$$

Definitions for r, s, κ, μ are given in Section 2.1. The set of equations given in Equation (A 3) is linear and homogenous; therefore, the method of separation of variables can be applied to solve them.

$$\Phi_j(\boldsymbol{x}, \boldsymbol{y}) = \boldsymbol{X}_j(\boldsymbol{x})\boldsymbol{Y}_j(\boldsymbol{y}) \tag{A 6}$$

Inserting in Equation (A 3)

$$\frac{\nabla_x^2 \boldsymbol{X}_j}{\boldsymbol{X}_j} + \frac{\nabla_y^2 \boldsymbol{Y}_j}{\boldsymbol{Y}_j} + \boldsymbol{B}_{mj}^2 = 0 \tag{A 7}$$

Separating $\boldsymbol{B}_{mj}^2$ into x and y direction components, Equation (A 7) can be written in terms of two one dimensional equations as,

$$\nabla_x^2 \boldsymbol{X}_j + \boldsymbol{B}_{xj}^2 \boldsymbol{X}_j = 0 \tag{A 8}$$

and

$$\nabla_y^2 \boldsymbol{Y}_j + \boldsymbol{B}_{yj}^2 \boldsymbol{Y}_j = 0 \tag{A 9}$$

where

$$\boldsymbol{B}_{xj}^2 + \boldsymbol{B}_{yj}^2 = \boldsymbol{B}_{mj}^2 \tag{A 10}$$

Unfortunately, because of the non-homogenous boundary conditions in x and y, it is not possible to determine the separation constants $\boldsymbol{B}_{xj}^2$ and $\boldsymbol{B}_{yj}^2$. This problem can be resolved by applying the Principle of Super Position. The problem is broken into four problems each having one non-homogenous condition [39] as follows,.

$$\Phi_j = \sum_S \Phi_j^S \quad S{=}E,W,U,D \tag{A 11}$$

with boundary conditions given as

$$\vec{n}_s.\vec{J}\Big|_{\Gamma_s} = f_J\Big|_{\Gamma_s} \quad S{=}E,W,U,D$$

$$\vec{n}_s.\vec{J}\Big|_{\Gamma_{s'}} = 0 \quad S' \neq S \tag{A 12}$$

The solution of this boundary value problem is a Fourier series for each *S* direction,

$$\Phi_j^S = \sum_{n=1}^{\infty} c_{jn}^S X_{jn}^S(x) Y_{jn}^S(y) \tag{A 13}$$

where $X_{jn}^S(x)$ and $Y_{jn}^S(y)$ are the solutions of the following equations,

$$\nabla_x^2 X_{jn}^S + B_{xjn}^{S^2} X_{jn}^S = 0 \tag{A 14}$$

and

$$\nabla_y^2 Y_{jn}^S + B_{yjn}^{S^2} Y_{jn}^S = 0 \tag{A 15}$$

where

$$B_{xjn}^{S^2} + B_{yjn}^{S^2} = B_{mj}^2 \tag{A 16}$$

Inserting Equation (A 13) into Equation (A 3) and dropping *j* for simplicity, we obtain,

$$(\nabla_x^2 + \nabla_y^2 + B_m^2) \sum_S \sum_{n=1}^{\infty} c_n^S X_n^S(x) Y_n^S(y) = 0 \tag{A 17}$$

The leakage term in the *y* direction can be moved to the RHS,

$$(\nabla_x^2 + B_m^2) \sum_S \sum_{n=1}^{\infty} c_n^S X_n^S(x) Y_n^S(y) = -\nabla_y^2 \sum_S \sum_{n=1}^{\infty} c_n^S X_n^S(x) Y_n^S(y) \tag{A 18}$$

Inserting Equation (A 15) in Equation (A 18) and integrating along the y direction we obtain

$$(\nabla_x^2 + B_m^2)\overline{\Phi}(x) = \sum_S \sum_{n=1}^{\infty} c_n^S {B_{yn}^S}^2 X_n^S(x) \int_{-1/2}^{1/2} Y_n^S(y)dy \tag{A 19}$$

where

$$\overline{\Phi}(\boldsymbol{x}) \stackrel{\Delta}{=} \sum_{\boldsymbol{S}} \sum_{\boldsymbol{n}=1}^{\infty} \boldsymbol{c}_{\boldsymbol{n}}^{\boldsymbol{S}} \boldsymbol{X}_{\boldsymbol{n}}^{\boldsymbol{S}}(\boldsymbol{x}) \int_{-1/2}^{1/2} \boldsymbol{Y}_{\boldsymbol{n}}^{\boldsymbol{S}}(\boldsymbol{y})\boldsymbol{dy} \tag{A 20}$$

Normalizations of $\{X_n^S\}$ and $\{Y_n^S\}$ are free to select, therefore we can select the normalization such that $\int_{-1/2}^{1/2} Y_n^S(y)dy = 1$. Then Equation (A 19) can be written as,

$$(\nabla_{\boldsymbol{x}}^2 + \boldsymbol{B}_{\boldsymbol{m}}^2)\overline{\Phi}(\boldsymbol{x}) = \sum_{\boldsymbol{S}} \sum_{\boldsymbol{n}=1}^{\infty} \boldsymbol{c}_{\boldsymbol{n}}^{\boldsymbol{S}} {\boldsymbol{B}_{\boldsymbol{yn}}^{\boldsymbol{S}}}^2 \boldsymbol{X}_{\boldsymbol{n}}^{\boldsymbol{S}}(\boldsymbol{x}) \tag{A 21}$$

The summation on the RHS represents the transverse leakage function in the transverse integrated diffusion equation. Although the RHS looks similar to the Fourier expansion for the transverse integrated flux ($\overline{\Phi}(x)$), it is different since $\overline{\Phi}(x)$ does not have the ${B_{yn}^S}^2$ term in the expansion as shown below,

$$\overline{\Phi}(x) = \sum_S \sum_{n=1}^{\infty} c_n^S X_n^S(x) \tag{A 22}$$

Rewriting the RHS of Equation (A 21) by introducing the β term

$$RHS = \sum_S \sum_{n=1}^{\infty} (\beta + ({B_{yn}^S}^2 - \beta)) c_n^S X_n^S(x) \tag{A 23}$$

we can extract the flux component as follows

$$\boldsymbol{RHS} = \beta\overline{\Phi}(\boldsymbol{x}) + \sum_{\boldsymbol{S}}\sum_{\boldsymbol{n}=1}^{\infty}(\boldsymbol{B}_{\boldsymbol{yn}}^{\boldsymbol{S}\,2} - \beta)\boldsymbol{c}_{\boldsymbol{n}}^{\boldsymbol{S}}\boldsymbol{X}_{\boldsymbol{n}}^{\boldsymbol{S}}(\boldsymbol{x}) \tag{A 24}$$

and move the flux component to the LHS of Equation (A 21)

$$(\nabla_x^2 + (B_m^2 - \beta))\overline{\Phi}(x) = \sum_{S}\sum_{n=1}^{\infty}(B_{yn}^{S\,2} - \beta)c_n^S X_n^S(x) \tag{A 25}$$

The buckling term in this new form of the transverse integrated equation is shifted by the β term. The term on the left hand side is the residual term when the transverse leakage is represented in terms of the intra-nodal flux. The β term can be selected in various ways,

1. Select β such that

$$\beta\int_{-1/2}^{1/2}\overline{\Phi}(\boldsymbol{x})\boldsymbol{dx} = \int_{-1/2}^{1/2}\left(\sum_{\boldsymbol{S}}\sum_{\boldsymbol{n}=1}^{\infty}\boldsymbol{c}_{\boldsymbol{n}}^{\boldsymbol{S}}\boldsymbol{B}_{\boldsymbol{yn}}^{\boldsymbol{S}\,2}\boldsymbol{X}_{\boldsymbol{n}}^{\boldsymbol{S}}(\boldsymbol{x})\right)\boldsymbol{dx} \tag{A 26}$$

   Then the β term can be defined as

$$\beta = \frac{1}{\overline{\Phi}}\int_{-1/2}^{1/2} RHS\;dx \tag{A 27}$$

2. Select $\beta = B_{y1}^{S\,2}$ which is the fundamental overtone. This approximation removes the first term in the summation in Equation (A 25).

3. Select the β so as to minimize RHS of Equation (A 25) when integrated over the span of x in a least square sense.

$$\left(\sum_{S} \sum_{n=1}^{\infty} (B_{yn}^{S\,2} - \beta) c_n^S \right)^2 \tag{A 28}$$

Then β satisfies the following equation,

$$\sum_{S} \sum_{n=1}^{\infty} (B_{yn}^{S\,2} - \beta)(c_n^S)^2 = 0 \tag{A 29}$$

where the orthogonality of $\{X_n^S\}$ has been utilized to obtain Equation (A 29).

Equation (A 29). can be solved for β as

$$\beta = \frac{\sum_{S} \sum_{n=1}^{\infty} B_{yn}^{S\,2} (c_n^S)^2}{\sum_{S} \sum_{n=1}^{\infty} (c_n^S)^2} = 0 \tag{A 30}$$